

DISSERTATION

Critical Currents in High-Temperature Superconducting Films and in Coated Conductors

ausgeführt zum Zwecke der Erlangung
des akademischen Grades eines
Doktors der technischen Wissenschaften
unter der Leitung von

Univ. Prof. Dr. phil. Dr. h.c. Harald W. Weber
E141

Atominstitut der Österreichischen Universitäten

eingereicht an der Technischen Universität Wien
Fakultät für Physik

von

Dipl.-Ing. Florian Hengstberger
e0025265

Wachaustraße 41
3121 Karlstetten

Wien, Mai 2009

Meiner Mutter

Danksagung

Bei Prof. Weber möchte ich mich dafür bedanken, dass er es mir ermöglichte, mich über einen langen Zeitraum ungestört einem spannenden Thema widmen zu können, für das Grundvertrauen, das er mir immer entgegenbrachte, und dafür, dass ich so arbeiten konnte, wie ich es für richtig hielt.

Michi, ohne deine Ermutigungen wäre meine Zeit nur halb so schön und ohne deine prompte Bereitschaft zu ausdauernden Diskussionen nur halb so aufregend gewesen.

Danke, Franz, für deine allmorgentliche Aufmunterung und deinen wissenschaftlichen Rat.

Bei allen Mitgliedern unserer Arbeitsgruppe, im Speziellen bei René Fuger, möchte ich mich für die gute Zusammenarbeit und das angenehme Arbeitsklima bedanken.

Marcus Weigand, John Durrell, Ahmed Kursumovic und Judith MacManus-Driscoll gilt mein Dank für ihre Unterstützung während meiner Aufenthalte in Cambridge.

Meinen Verwandten, vor allem meinem Vater und meinen beiden Schwestern sowie Walther und Gerda, möchte ich herzlich dafür danken, dass sie sich für den Fortschritt meiner Arbeit interessierten, ohne (genau) zu wissen, woraus sie eigentlich besteht.

Babsi, du weißt, was du für mich bedeutest.

Kurzfassung

Gegenstand dieser Dissertation ist die Charakterisierung dünner Filme des Hochtemperatur-Supraleiters $\text{YBa}_2\text{Cu}_3\text{O}_7$, die mit verschiedenen großtechnologisch relevanten Verfahren auf ein- und poly-kristallinen Substraten aufwachsen. Hierzu wird kritische Stromdichte J_c , die maximale Stromdichte, die das Material mit akzeptablen Verlusten tragen kann, mit einander ergänzenden numerischen und experimentellen Methoden untersucht.

Die Homogenität der Proben wird durch eine neue Technik sichergestellt, die mittels Hallsonden das magnetische Feld über der Probe ortsabhängig auflöst. Berechnungen des lokalen J_c aus Hall Scans des Selbstfeldes (das magnetische Feld, das von den Strömen in der Probe erzeugt wird) erlauben, J_c als Funktion der Position in Probe zu quantifizieren. Durch diese Methode kann gezeigt werden, dass eine enge Korrelation zwischen J_c und B an einem bestimmten Ort besteht, was klar auf eine Feldabhängigkeit $J_c(B)$ auch bei kleinsten Feldern hinweist.

Numerische Berechnungen der Stromdichte- und Magnetfeld-Verteilungen simulieren Transport- und Magnetisierungs-Experimente. Dabei wird ein Ausdruck abgeleitet und durch die Berechnungen bestätigt, der den Effekt von $J_c(B)$ auf die Dickenabhängigkeit von J_c angibt.

Magnetisierungs- und Transport-Messungen bestimmen das technologisch relevant mittlere J_c eines Film in Abhängigkeit von angelegtem Magnetfeld und der Temperatur. Es zeigt sich, dass Granularität J_c signifikant reduziert, wenn die Probe auf poly-kristallinen Substraten aufgebracht wird. Spezielle Bedeutung kommt dem Einfluss von künstlichen Defekten auf die Verankerung im Material zu. Obwohl nichtsupraleitende Einschlüsse, die während des Wachstums entstehen, J_c in magnetischen Feldern erhöht, vergrößert Neutronenbestrahlung, die als Vergleichstest dient, $J_c(B)$ viel stärker. Das zeigt, dass noch bessere Ergebnisse in magnetischen Feldern durch eine Optimierung der Defektstruktur erreicht werden können.

Abstract

The subject of this thesis is the characterisation of high-temperature superconducting thin films of $\text{YBa}_2\text{Cu}_3\text{O}_7$ grown by methods, which are relevant for large-scale production, on single- as well on poly-crystalline substrates. Complementary experimental and numerical methods are employed to analyse the critical current density J_c , the maximum current density the material conducts with acceptable dissipation, emphasising the magnetic field dependence of the critical current density $J_c(B)$.

The supercurrent in the sample is spatially resolved by a novel scanning Hall probe technique, which assures the homogeneity of the investigated films. Calculations of the local J_c from Hall scans of the self-field (the magnetic field created by the currents flowing in the sample) allow to quantify J_c as a function of the position in the films. This method reveals a close correlation between J_c and B at a certain position, which is a clear indication for a field dependence $J_c(B)$ down to the lowest fields and is of fundamental interest.

Numerical calculations of the current density and magnetic field distribution are performed simulating transport and magnetisation experiments on thin films. An analytic expression is derived and confirmed by the calculations, which quantifies the effect of $J_c(B)$ on the thickness dependence of J_c .

Magnetisation and transport measurements determine the technologically relevant average J_c of the film as a function of the applied magnetic field and temperature. It is found that granularity significantly reduces J_c , if the sample is grown onto poly-crystalline substrates. Particular emphasis is laid on the influence of artificial defects on flux pinning in the material. Although non-superconducting inclusions precipitated during growth improve J_c in magnetic fields, neutron irradiation, which serves as a benchmark experiment, increases $J_c(B)$ in the films much more effectively. This demonstrates that a higher in-field performance is achievable, if the defect structure of the films is optimised.

Contents

I. Introduction	1
1. Pinning in high-temperature superconductors	2
1.1. Zero temperature	2
1.2. Finite temperatures	4
2. Thin film geometry	6
2.1. Flux penetration into thin films	6
2.2. The “inaccessible” thickness	9
II. Experimental	10
3. YBCO thin film growth	11
3.1. Pulsed Laser Deposition	11
3.2. Hybrid Liquid Phase Epitaxy	12
3.3. MOD	14
3.4. Patterning	14
4. Instrumentation	16
4.1. SQUID	16
4.2. Vibrating Sample Magnetometer	19
4.3. Transport measurements	23
4.4. Scanning Hall probes	25
4.5. TRIGA Mark-II reactor	27
4.6. Focussed Ion Beam	28
5. Evaluation methods	31
5.1. Magnetisation critical current density	31
5.2. Transport critical current density	35
5.3. Irreversibility line	38
5.4. Transition temperature	39
III. Results	42
6. Magnetoscan	43
6.1. Interpretation	43

6.2. Comparison to alternative techniques	46
7. Inversion of Hall maps	50
7.1. Numerics	50
7.2. Application to bulks	57
7.3. Application to thin films	61
8. Simulation of self-field effects	68
8.1. Numerics	70
8.2. Simulation of magnetisation measurements	71
8.3. Simulation of transport measurements	74
9. Magnetisation measurements	82
9.1. Field dependence of the critical current density	83
9.2. Effect of doping	87
10. Transport measurements	91
10.1. Anisotropy of the critical current density	91
10.2. Irreversibility line	97
11. Irradiation	101
11.1. Single-crystalline substrates	102
11.2. Poly-crystalline substrates	106
12. Summary	111
Bibliography	114
Curriculum vitae	123

Part I.

Introduction

Chapter 1.

Pinning in high-temperature superconductors

1.1. Zero temperature

A perfect type-II superconductor in the mixed state is not able to support a current without dissipating energy, because the energy landscape seen by the vortices is, apart from their mutual interaction, position-independent in a perfect material and consequently any force exerted on the flux lines initiates their movement. The normalconducting cores of the vortices cause a substantial electrical resistivity in the flux flow regime

$$\rho_{\text{ff}} = \rho_{\text{normal}} \left(\frac{H}{H_{c2}} \right), \quad (1.1)$$

which is a considerable fraction of the normal-state resistivity and high-temperature superconductors seem to loose the main argument in favour of their application.

But in contrasts to, for example, copper, where the resistivity is lowest in a homogeneous material, the irreversible properties of superconductors greatly benefit from defects, because they eliminate the translation invariance by lowering the condensation energy at their position. The spatial variations attract the flux lines, which now remain pinned as long as the external force exerted on them is lower than the forces of the pins and the material regains its outstanding conductivity.

Many different types of pinning centres are active in YBCO ranging from weakly pinning oxygen disorder in single crystals to a high density of strongly pinning crystallographic defects in thin films, such as edge and screw dislocations [1], which are a consequence of the fast growth far from thermodynamic equilibrium. Apart from structural imperfections, also a certain amount of non-superconducting

secondary phases, as for example Y_2O_3 inclusions (see Fig. 9.5), are formed during thin film growth. The engineering of a highly effective defect matrix, for example by the precipitation of secondary phases, is one of the key tasks of current materials research.

When the vortices start to penetrate the sample above the lower critical field H_{c1} , the pinned flux line lattice is now able to partially withstand the driving force, caused by the application of an external magnetic field or a transport current (cf. chapter 2). As a consequence, a flux density gradient is established and the magnetisation decays from the edges towards the centre of the sample. The simplest material law accounting for this behaviour is the assumption of a constant gradient

$$\vec{\nabla} \times \vec{M} = \vec{J}_c. \quad (1.2)$$

This is the scope of the widely used Bean model, which contains the critical current density J_c , i.e., the current density the material is able to sustain without dissipation, as the only material parameter. Despite its simplicity the concept is often sufficient to explain many of the observations in magnetisation and transport experiments.

However, J_c is only a phenomenological quantity—it is not connected to the material properties. To the best of my knowledge none of the available theories, which link J_c to fundamental properties, explains the high critical current densities in YBCO thin films. This is evident in literature, where a theoretical framework is seldom used for its designated purpose, i.e., to reveal the intrinsic properties not directly accessible to experiment.

The fact that such a theory does not exist at present is not due to a lack of imagination—it is the complexity of the phenomenon, which renders a theoretical foundation so difficult. First, superconductivity is effected by a correlated electron system, which represents itself a challenging problem (the high-temperature superconductors still await a theoretical description). Second, the thermodynamic properties in a magnetic field must be treated and one enters into the physics of vortices, objects made up from many superconducting electrons. Not enough, the pinning of the flux line lattice is the collective effort of interacting flux lines attracted by the defect matrix.

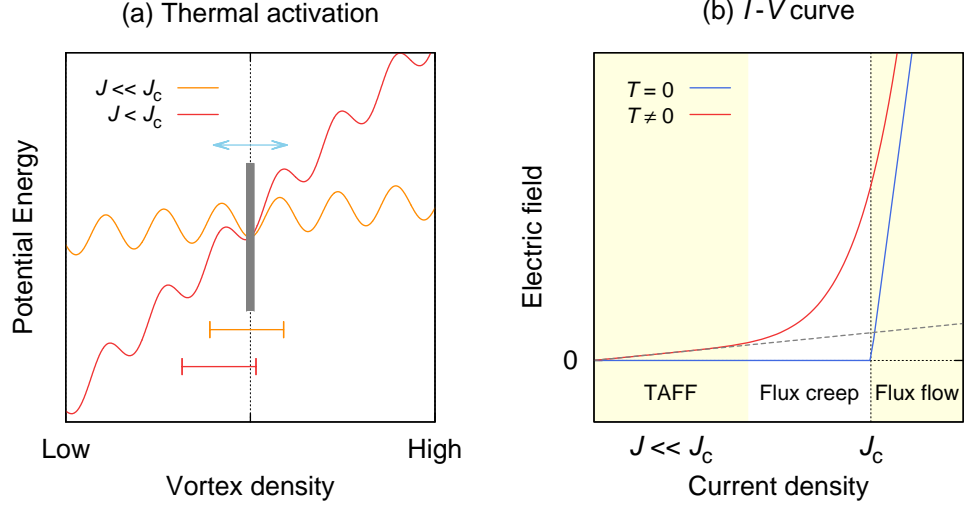


Figure 1.1. (a) Thermal activation of a vortex. In the presence of a current the flux lines preferentially relax the gradient. (Bars indicate the frequency of moving in the direction of blue arrows, i.e., towards or opposite to the gradient.) (b) Resistive transition at zero and finite temperatures showing the effect of thermal activation.

1.2. Finite temperatures

At finite temperatures, thermal energy de-pins vortices and causes the vortex density gradient defined by (1.2) to relax. This is particularly important for YBCO and high-temperature superconductors in general because of their relatively low pinning energy (the coherence length is only a few nanometres) and their high operating temperature (typically 77 K) compared to conventional low-temperature superconductors.

The effect of thermal energy can be understood by considering the activation of a single flux line out of a potential well of depth U , an event whose rate depends exponentially on the ratio of these two energies. If there is no gradient in the vortex density, i.e., no macroscopic current J flows through the sample, there is no preferred direction: the movement of the activated vortices will be random and no electric field will be created on average. If, on the other hand, a macroscopic magnetisation exists or a transport current flows, the vortices will preferentially lower the flux density gradient (cf. Fig. 1.1a) and the imbalance of hops up- or downhill

$$E \propto \left| e^{-U^\uparrow(J)/k_B T} - e^{-U^\downarrow(J)/k_B T} \right| \quad (1.3)$$

creates a net electric field E . The particular form of $E(J)$ depends on $U(J)$ as well as on the relative strength of the thermal energy compared to the driving force on the vortices.

When strong thermal activation is biased by a relatively small driving force ($J \ll J_c$) the assumption of a linear $U(J)$ dependence and a first order expansion of (1.3) results in the ohmic relation

$$E = \rho_{\text{TAFF}} J, \quad (1.4)$$

which defines the resistivity of a superconductor in the thermally activated flux flow (TAFF) regime. The fact that the resistance is independent of the current supports a resistive criterion for defining the irreversibility line (cf. section 5.3), because these measurements probe a state governed by thermal activation.

In the case of a strong force, i.e., if the gradient is close to critical ($J \approx J_c$), the vortices will almost exclusively relax the gradient and the first contribution of the right hand side (1.3) can be neglected. Assuming a logarithmic dependence of the activation energy on the current $U^\downarrow(J) = U_0 \log(J/J_c)$, we obtain the power-law

$$E \propto \left(\frac{J}{J_c}\right)^n \quad n = U_0/k_B T \quad (1.5)$$

observed in transport measurements of the critical current density. Using an arbitrary electric field criterion E_c , an I - V curve can be described in terms of the critical current density and the n -value (cf. section 5.2).

Figure 1.1b depicts the effect of a finite temperature on the I - V curve: the sharply defined transition into the flux flow regime at $J = J_c$ at zero temperature is smeared out by thermal activation and dissipation occurs also at the lowest applied currents.

Chapter 2.

Thin film geometry

A large number of samples, grown by various deposition methods on single- as well as poly-crystalline substrates, was investigated in the course of this work. Critical current densities exceeding 10^{10} Am^{-2} at zero applied field and 77 K are routinely achieved in the approximately $1 \mu\text{m}$ thick conductors. Their most general property is, however, their geometry—the thickness is much smaller than the lateral dimensions (typically a few millimetres)—and the high aspect ratio $a, b \gg c$ of this geometry determines the behaviour in transport and magnetisation measurements. In particular two features—the early flux penetration at applied fields much below H_{c1} and the “inaccessibility” of the thickness in those experiments—are specific to thin films. They are introduced below by modelling the sample as a long strip of width a and thickness c .

2.1. Flux penetration into thin films

2.1.1. External applied fields

If a superconducting strip is exposed to an external applied field, surface currents shield the magnetic field from the interior as long as the magnetic induction is below the lower critical field B_{c1} in the entire body of the sample. It is a peculiarity of the strip geometry that the shielding currents strongly amplify the magnetic induction at the edges of the sample. Subjected to an external field H , flux penetration occurs, if [2]

$$B_{c1} \approx \mu_0 H \sqrt{a/c}. \quad (2.1)$$

The amplification $\sqrt{a/c}$ is about 50 for typical samples. As a consequence, the demagnetisation of the Meissner currents reduces the maximum applied field,

which is still compatible with flux expulsion, to below 1 mT at 77 K, although B_{c1} is about 30 mT for fields $H \parallel c$ at this temperature [3].

Hence, comparatively small external fields cause an entry of flux into the conductor. At the penetration field B^* vortices have populated the entire conductor; one finds for a strip in the Bean critical state [4]

$$B^* > \mu_0 c J_c / \pi = B_f. \quad (2.2)$$

Here, the typical field B_f of a thin film was introduced. It represents a suitable field scale for this geometry and is 4 mT for a 1 μm thick conductor carrying a critical current density of 10^{10} Am^{-2} . This is remarkable because B_f is smaller than B_{c1} by nearly a factor of ten at 77 K; in the absence of demagnetisation the sample would still be in the Meissner state.

Penetration from different sides results in oppositely directed currents flowing left and right of the centre and no net current passes through the cross-section. The current distribution creates a pronounced maximum of the z -component of the self-field at the centre, suitable for characterising the conductor with scanning Hall probes (see Fig. 2.1).

2.1.2. Transport currents

If a transport current is applied to a strip at zero applied field, Meissner currents generate a loop-shaped magnetic field around the conductor. Analogous to the case of an external applied field, the generated magnetic induction is strongest at the sample edges and determines the ultimate transport current in the Meissner state [2]

$$B_{c1} \approx \frac{\mu_0 I}{2\pi c} \sqrt{c/a}, \quad (2.3)$$

much less than the critical current a typical tape is able to carry. Similar to magnetisation, vortices penetrate the sample and establish a flux density gradient on their way inwards. It is worth noting, that parts of the sample are in the critical state, while others are free of flux—the current density does not homogeneously approach J_c in the conductor.

If the applied current is equal to the critical current I_c , the loop shaped vortices have reached the centre of the conductor and the entire sample is in the critical state. The circular field of the Meissner transport current implies that vortices of opposite direction nucleate left and right of the centre. Thus the currents flow in

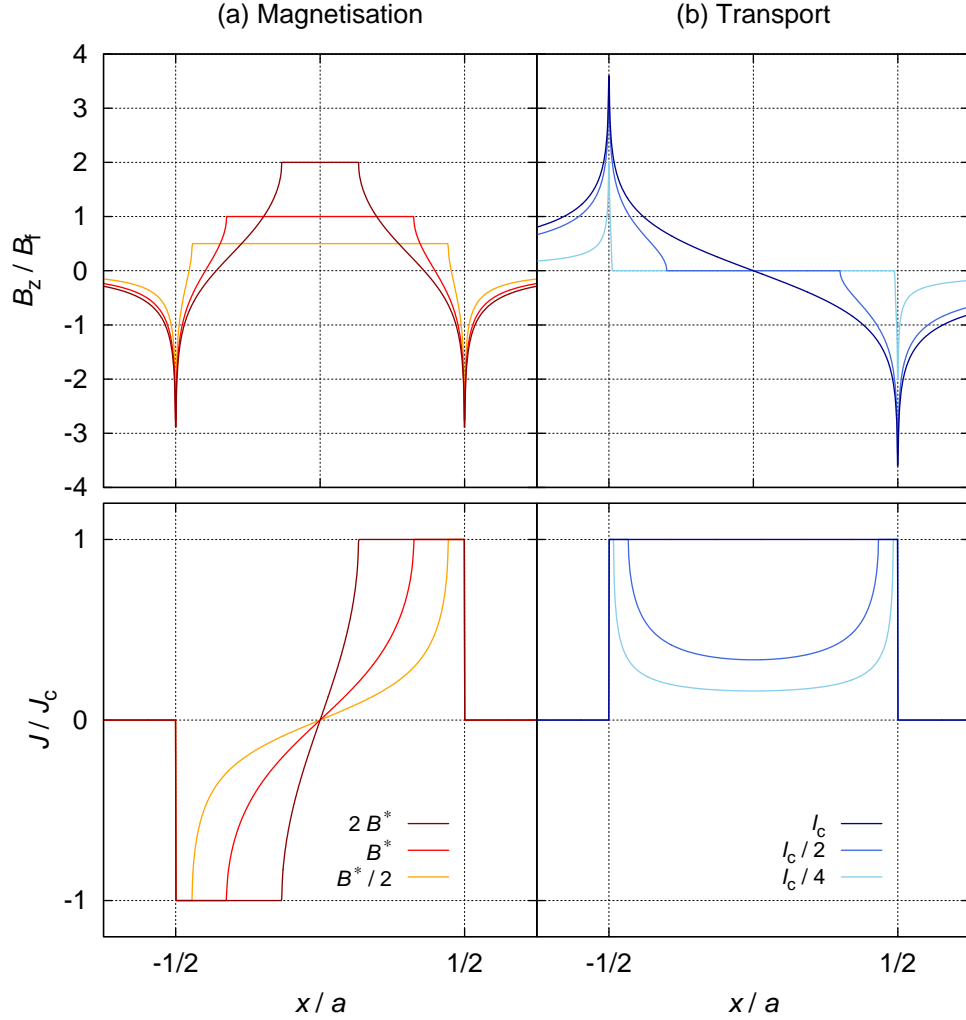


Figure 2.1. Application of the Bean model to thin films—current distribution and self-field. (a) In a magnetised strip currents of opposite direction flow in the left and right half of the conductor, creating a prominent peak in B_z at the centre. (b) If the tape conducts a transport current below I_c , the current density is—unlike in a metallic conductor—not homogeneously distributed over the cross-section. The direction of the currents is equal in the entire conductor and the z -component of the magnetic field is zero at the centre.

the same direction and the self-field is parallel to the surface above the centre of the tape (cf. Fig. 2.1).

2.2. The “inaccessible” thickness

In order to analyse the flux pinning properties of a film, the critical current density must be evaluated from either the magnetic moment or from the critical transport current of the sample (cf. chapter 5). This requires an exact knowledge of the sample cross-section; in particular a precise measurement of the thickness of the superconducting layer, which is below the resolution of optical microscopy.

One tries, of course, to obtain the thickness with the experimental equipment at hand. Evidently, transport experiments are of no avail—but the same is true of magnetisation. In the Bean critical state the magnetic moment parallel to the short side of a strip is

$$m_{\parallel} = H_f a^2 \pi \left[\tanh \left(\frac{H_{\max}}{H_f} \right) + 2 \tanh \left(\frac{H - H_{\max}}{2H_f} \right) \right] \quad (2.4)$$

per unit length [4]. (Here, H_{\max} refers to the last maximum applied field.) Because the expression depends on the typical field $\mu_0 H_f = B_f$ of a thin film, which is proportional to the product cJ_c , thickness and critical current density affect the magnetisation curve in the same way and are thus inseparable. Equation 2.4 further shows that other irreversible quantities, such as the the AC magnetic response or the slope of the reverse leg, are in consequence also functions of the (critical) sheet current density $K_c = cJ_c$, which determines the thin film geometry.¹

Assessing the reversible magnetic moment is, regardless of the early flux penetration at fields much below H_{c1} , also futile, because [5]

$$m_{\parallel}, m_{\perp} \propto H a^2 \pi \frac{1}{1 - \gamma c/r} \quad (2.5)$$

for a flat disk in the Meissner state with radius $r \gg c$ for the two main field directions (γ is a factor of about one). Although this expression explicitly contains the aspect ratio c/r , the effect is too small to measure the thickness with confidence, because it is typically a factor of thousand smaller than the radius.

The thickness of a flat superconductor is thus inaccessible to both transport and magnetisation experiments but it can be attained for example in an FIB system as described in section 4.6.

¹ However, the sheet current density is a very practical quantity—it specifies the critical current the conductor is able to carry per unit width.

Part II.

Experimental

Chapter 3.

YBCO thin film growth

After twenty years of intensive research and with the advent of the oxy-pnictides the ceramic high-temperature superconductors can be regarded as a mature class of materials ready for applications. Much effort has been devoted to meet the key prerequisites of mechanical flexibility and reproducible performance on long lengths by growing films on textured poly-crystalline metal tapes. It was soon recognised that a sophisticated buffer layer architecture, which acts as a diffusion barrier or transfers the template's texture to the superconductor, is essential. Thus, fabricating a high-performance coated conductor involves tailoring many processing parameters. In order to pretune them and to investigate the potential performance of the material in the absence of granularity one usually starts growing samples on single-crystalline substrates.

The available spectrum of growth technique is rich and ranges from rather straightforward physical vapour deposition to complex chemical methods. It is currently attempted to produce “all-chemical” coated conductors [6], an inexpensive way to grow the superconductor and the individual buffer layer in an exclusively chemical route. Especially the latter concept will, once accomplished, enable inexpensive large scale production and will thus appeal to industry.

3.1. Pulsed Laser Deposition

Pulsed laser deposition (PLD) is a physical deposition technique, where a target, for example a stoichiometric YBCO pellet, is vaporised by a laser beam and the film grown from the gas phase, because the pulsed laser beam deposits a high amount of energy on a small spot of the target surface in a very short time. As a consequence, the absorption of the light is adiabatic and leads to local vaporisation of the target material forming a plasma plume, which transports the material to

the substrate. The first successful deposition of YBCO-films by PLD was reported shortly after their discovery [7].

The pulse rate of the laser determines the amount of material ablated per time and plays a crucial role in the growth kinetics of the film. Typically, the repetition rate of the pulses is about 10 Hz and one pulse refers to a deposition of roughly 0.1 nm of material. This results in a growth rate of approximately 1 nm/s [8].

An advantage of PLD sample growth is the easy change of the target material. Using a multi-target carousel system, more than one material can be ablated in a single deposition. In this way nano-precipitates were introduced in the samples provided by the Leibniz Institute for Solid State and Materials Research Dresden (IFW Dresden). A total of 75 pulses on a YBCO target covered the single-crystalline SrTiO_3 (STO) with about 6.5 unit cells and were followed by a few shots on a Ir or Hf target. The amount of transition metal deposited is not sufficient to cover the entire surface and randomly distributed islands of nanometre size are formed. The process is repeated 40 times and the quasi-multilayer is formed [9, 10].

The films were grown using off-axis laser deposition, which results in a higher film homogeneity. The processing parameters were representative for PLD sample growth: the film was grown in vacuum at a temperature of 820 °C; superconductivity was induced by in-situ oxygenation at a oxygen partial pressure of 400 mbar [9]. In the end the samples were covered with a gold protective layer.

3.2. Hybrid Liquid Phase Epitaxy

As the name suggests liquid phase epitaxy (LPE) involves a liquid phase, which mediates the crystal growth, for instance an Y-rich BaO-CuO melt [11]. By undercooling supersaturation is achieved, i.e., the Y content of the flux exceeds the equilibrium concentration, and YBCO nucleates at the substrate—the film starts to grow. In general this process is much closer to thermodynamic equilibrium conditions than, for example, growth by PLD, where the gas phase solidifies on the substrate surface, and a high degree of structural perfection can thus be expected in films grown by LPE [12]. However, the presence of structural defects is vital for the application of the material. Hence higher supersaturation is desired, but difficult to maintain during growth [12]. A further disadvantage is the dominance of Y diffusion in the flux and its aggressiveness to certain buffer layers covering substrate.

These problems are overcome by combining LPE and PLD to hybrid liquid phase epitaxy (HLPE) [12, 13]. Initially a thin layer of BaO-CuO (about 100 nm)

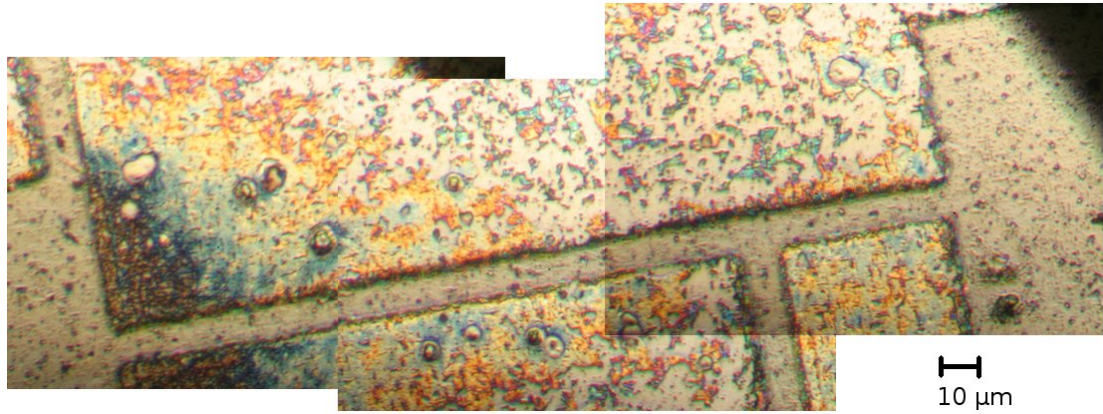


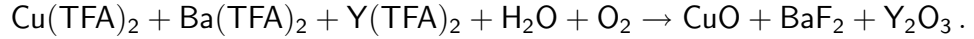
Figure 3.1. Optical micrograph showing the 0°-track of a HLPE sample bridged for transport measurements.

is deposited by PLD on the substrate; it constitutes the liquid phase that mediates the growth. The subsequent YBCO deposition from the PLD plume supersaturates the flux and nucleation starts at the liquid-solid interface, if the size of the incoming particles is undercritical, i.e., there is no precipitation in the liquid. The diffusion in the liquid is not a determining factor in thin layers [12] and the growth rate is controlled by the feed rate, i.e., the repetition rate of the laser. One advantage of this method is that the flux traps virtually all deposited material. Moreover, the liquid-solid interface at the growth front provides an environment compatible with laser pulse rates, which are higher than in PLD by a factor of ten. The resulting high growth rates of up to 35 nm/s [13] are reflected in a short deposition time and render this technique particularly interesting for reducing the processing time in industrial production.

A large number of HLPE sample was provided by the Department of Materials Science and Metallurgy, University of Cambridge (UCAM). Typical growth parameters were: laser repetition rate 50 Hz, sample (heater) temperature of about 820 °C, and oxygen partial pressure of 1 mbar. The in-situ oxygenation at 500 °C and 600 mbar lasts about one hour. Secondary phases are incorporated by preparing a laser target with the desired composition or by switching between targets with different materials. The samples were deposited on single-crystalline STO as well as on surface-oxidised NiO [14] or on RABiTs tape.

3.3. MOD

In contrast to the previous methods, which both employ a laser to ablate the target material, no expensive equipment is needed in metal-organic deposition (MOD) for the coating. Here, wetting with trifluoroacetate (TFA) solution by either spin or dip coating transfers the starting products to the substrate. During the pyrolysis stage at about 300 °C the film shrinks and decomposes (besides other volatile products) into



The end products of this reaction constitute the precursor material for the subsequent growth stage carried out at a temperature of about 800 °C, where YBCO can form thanks to the decomposition of BaF₂. The growth is finalised by oxygenating the sample.

The large number of compounds involved render the process more complex than, for example, the physical vapour deposition techniques; especially a precise control of the water pressure is crucial [15]. Moreover, further optimisation of the chemical route is required to obtain a thickness greater than 1 µm, which is well within reach of PLD and in particular HLPE sample growth.

Samples grown by MOD have been provided by the Institut de Ciència de Materials de Barcelona (ICMAB) and by Nexans SuperConductors (Nexans).

3.4. Patterning

Contacting a superconducting film for transport measurements is one of the most delicate operations due to the high current carrying capability of the material. In order to avoid ohmic heating, it is necessary to fabricate contacts, which are sufficiently large for supporting the critical current and have low resistance. If the film is grown on standard single-crystalline substrates (10 × 5 mm²) or short pieces of metallic tape, there is usually not enough space for sufficiently large contacts and the width of the film has to be reduced to decrease the critical current.

A number of HLPE samples were patterned to 10 µm wide tracks (see Fig. 3.1) using the pattern depicted in Fig. 3.2. At the beginning the sample is cleaned with acetone in an ultrasonic bath and a standard photolithographic process is used to cover all of the sample except the contact pads with photoresist. Ion-milling of

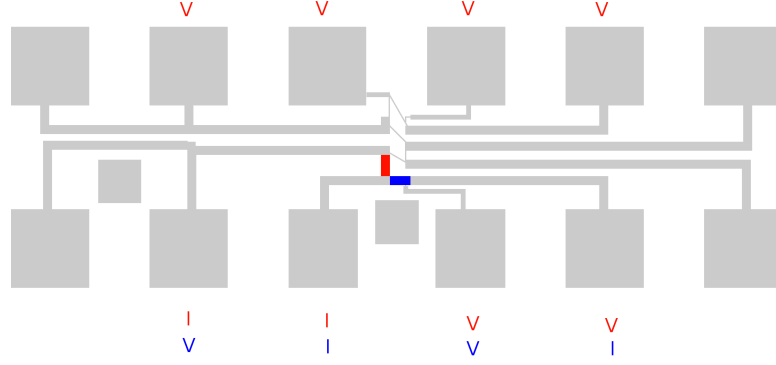


Figure 3.2. Pattern used in transport measurements on HLPE samples. The blue and the red track are magnified and referred to as 0° - or 90° -track in the following. The pattern provides some redundancy; possible voltage and current pads are labelled in the colour of the tracks.

the BaO-CuO flux situated on top exposes the YBCO, which is then coated with Ag and Au (combined roughly $1\text{ }\mu\text{m}$ thick) by sputter deposition. The photoresist is easily removed and only the contact pads are covered with the metals. A second photolithographic step is necessary to protect the tracks in the final physical etching process, forming the pattern by ion-milling the sample.

Chapter 4.

Instrumentation

4.1. SQUID

A Superconducting Quantum Interference Device (SQUID) is a magnetic flux detector, which is sensitive to amounts of flux much below the elementary flux quantum $\Phi_0 \approx 2.068 \times 10^{-15} \text{ Wb}$. It utilises two basic phenomena of superconductors, namely flux quantisation and Josephson tunnelling through weak links. Among the two basic designs, the DC and the AC SQUID (containing one or two Josephson contacts), the latter is generally applied in magnetometers.

The magnetic flux generated by the sample is not directly sensed by the SQUID and a flux transformer is used to transfer the signal. One part of the transformer is located in the liquid helium bath and couples inductively to the SQUID, while the other part is wound around the sample chamber (see Fig. 4.1a). The winding direction and the number of turns constitute a second-order gradiometer, which cancels even linearly z -dependent field inhomogeneities.

As a consequence of flux quantisation, the SQUID signal is periodic in Φ_0 . This is overcome by employing a feedback mechanism, which compensates the external flux and stabilises a constant amount of flux through the SQUID. The compensation current provides the measured value.

4.1.1. DC measurements

Due to the feedback mechanism samples with high magnetic moments can be measured, but only relative changes in flux are detectable. The sample is therefore moved along the z -axis through the gradiometer coils and the total change of flux in the gradiometer is recorded as a function of the sample position.

The SQUID readout voltage is found by integrating the magnetic induction passing through a single pickup-coil with radius r and distance Δz to a magnetic dipole ($\vec{m} = m \vec{e}_z$). In cylindrical coordinates the expression reads

$$\Phi(\Delta z) = \frac{\mu_0 m}{4\pi} \int_0^{2\pi} \int_0^r d\theta d\rho \rho \frac{2\Delta z^2 - \rho^2}{(\rho^2 + \Delta z^2)^{5/2}} = \frac{\mu_0 m r^2}{2(\Delta z^2 + r^2)^{3/2}}. \quad (4.1)$$

The output voltage of the SQUID can thus be written as a function of the z -position of the sample

$$U(z) \propto 2\Phi(z) - \Phi(z - h) - \Phi(z + h), \quad (4.2)$$

which is depicted in Fig. 4.1b; the sample can be centred by finding the maximum of the curve.

During the measurement least square fits to (4.2) are used to identify the magnetic moment of the sample. It is exactly this procedure that makes SQUID measurements sophisticated. Close to the irreversibility line, for example, even very low field inhomogeneities affect the critical state and the magnetic moment can be position-dependent. Moreover, at very low applied fields the sample holder's signal can be comparable to a weakly superconducting film. In such cases the fit algorithm is prone to fail and a careful inspection of the raw data is mandatory.

4.1.2. AC measurements

A change in flux through the detection coils can also be induced by applying a time varying magnetic field to the sample. The powerful superconducting magnets are not designed to produce alternating fields and a separate copper coil is thus provided. Employing a phase sensitive detection circuitry provides the in-phase signal m' and the out-of-phase signal m'' .

$$m(t) = m' \cos(\omega t) + m'' \sin(\omega t) \quad (4.3)$$

This method is particularly suitable for T_c measurements, where the superconductivity in the sample is probed at a minimal applied field, in order to minimise perturbances. Furthermore, the out-of-phase-signal, which is related to the dissipation in the sample, shows a pronounced peak during the superconducting condensation.

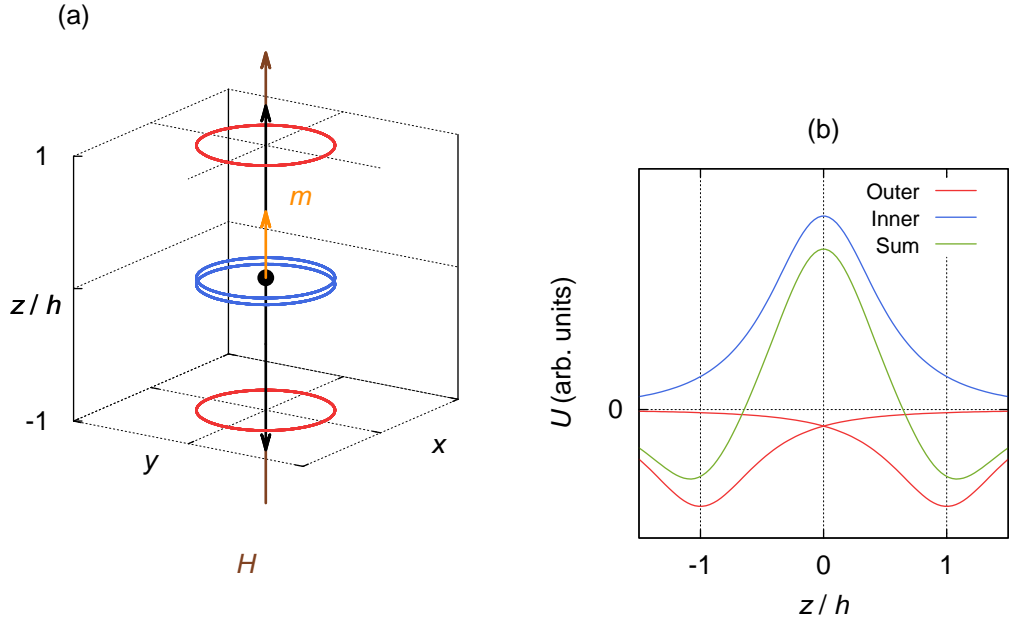


Figure 4.1. (a) The coil configuration of the SQUID implements a second-order gradiometer. (Equal colours refer to equal winding direction.) (b) Readout voltage of the gradiometer as a function of the z -position of the sample.

4.1.3. Quantum Design SQUIDs

Two SQUID magnetometers manufactured by Quantum Design and provided with 1 and 7 T magnets were used to assess the DC magnetic moment and to determine the transition temperature by AC measurements. Their magnets can be operated in the persistent mode, which was used to reduce the noise coupling into the magnet from the power supply. The SQUID detection system of the magnetometers is very sensitive and measures magnetic moments as low as 10^{-9} Am^2 , provided that the background signal is sufficiently low. However, the environmental parameters, in particular the accuracy in temperature at the sample position and the temperature gradient established in the VTI, represent considerable uncertainties.¹ A further source, which interferes with the sample's signal, is the sample holder. Fortunately, the DC magnetic signal of good quality YBCO thin films usually exceeds both, the sample holder's and a single crystalline substrate's magnetic signal, by orders of magnitude. The influence of an underlying ferromagnetic signal on the evaluation of a hysteresis loop is discussed in section 5.1.3 in more detail.

¹ Note that in a DC measurement the sample is situated in the lowest position after each scan and not in the centre of the detection coils, where the temperature sensor is mounted on the sample wall.

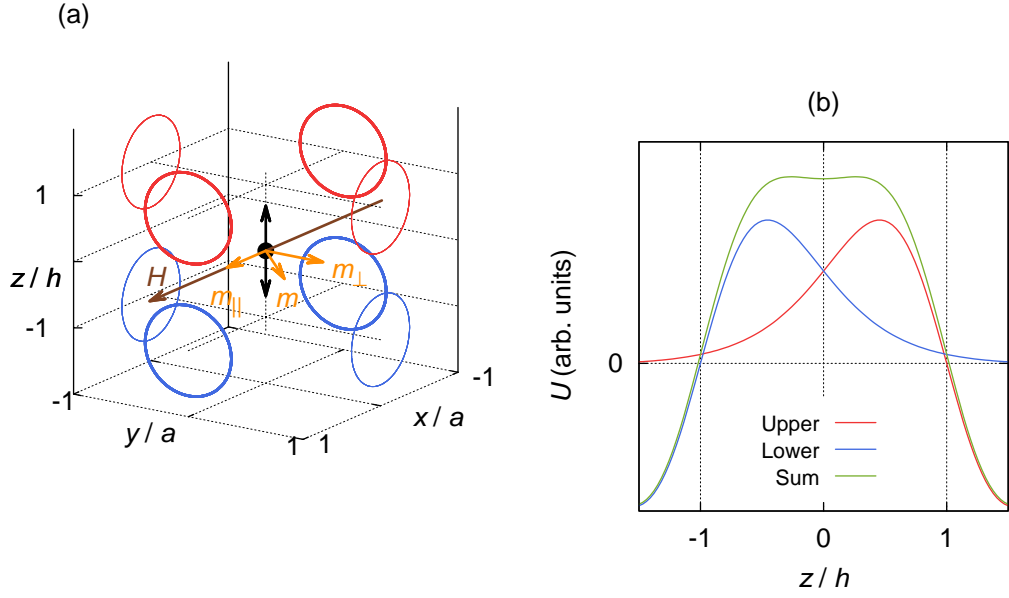


Figure 4.2. (a) Coil configuration of the VSM. A set of 8 coils is used to measure the component of the magnetic moment parallel and orthogonal (orange arrows) to the external applied field (brown arrow). (Equal colour refers to equal winding direction.) The sample is centred in between the coils and oscillates along the z -direction (black arrow). (b) Both coil pairs together create a flat peak in the output voltage. The shallow minimum is used to centre the sample vertically.

The transition temperature T_c was determined by temperature dependent AC measurements using standard parameters of $30 \mu\text{T}$ and 31 Hz for the applied AC field.

4.2. Vibrating Sample Magnetometer

Whereas the SQUID is capable of detecting relative quantities of static magnetic flux, a Vibrating Sample Magnetometer (VSM) [16] is based on sensing the inductive voltage, which is generated by an oscillating sample's time varying magnetic flux. This is achieved by vibrating the sample in the centre of a set of pick-up coils. For this purpose it is attached to a rod, which is driven by a system similar to a loudspeaker [17]. The unwanted background signal, which results, e.g., from external vibrations coupled to the instrument, is eliminated by employing a lock-in technique, where the drive signal serves as a reference.

The coil setup determines the performance of the system and VSMs with various assemblies have been built [18]. The VSM used in this work is equipped with a split-

coil magnet, and angular dependent measurements can be performed by rotating the sample. Therefore, two independent sets of coils (see Fig. 4.2a) are necessary to measure the component of the magnetic moment parallel and orthogonal (m_{\parallel} and m_{\perp}) to the applied field simultaneously. Each set consists of an upper and a lower pair of coils, the lower one being oppositely wound, which effectively cancels the voltage induced by the sweep of the external field. The coil configuration is similar to [19] and provides high sensitivity and a linear response with some tolerance to misalignment by creating a flat peak along the z -axis (cf. Fig. 4.2b).

Note that by symmetry (cf. Fig. 4.2a) the net flux through the coils is zero in the entire x,y -plane, because a VSM coil set is designed to be sensitive to changes of flux, which it is not necessarily correlated with the amount of flux passing through the coil system. This is opposite to the SQUID detection coils, where one aims at maximising the total flux, when the sample is in the centre position.

4.2.1. Calculation of the VSM Signal

The voltage induced in the coil system by a harmonically oscillating magnetic dipole $z(t) = z_0 \sin(\omega t)$ is proportional to the net change of flux through the coils

$$U \propto \sum_i \frac{d\Phi_i}{dt} = z_0 \omega \cos(\omega t) \sum_i \frac{d\Phi_i}{dz}. \quad (4.4)$$

Here $d\Phi_i/dz$ denotes the change in flux created by the movement of the sample along the z -axis. (The coordinate system employed is depicted in Fig. 4.2a.) The sensitivity of a VSM can, therefore, be tuned by changing either the amplitude or the frequency of the vibration.

If one neglects the finite size of the loop shaped coils and uses a dipole approximation, the “principle of reciprocity” can be employed to derive a closed expression by calculating the reverse problem, i.e., the field created by the pick-up coils at the sample position. The peak voltage \hat{U} induced, for example, in the parallel coil set is

$$\hat{U}_{\parallel} \propto z_0 \omega \sum_i \frac{d}{dz} \vec{H}_i \cdot \vec{e}_x, \quad (4.5)$$

where \vec{H}_i refers to the x -component of a dipole’s magnetic field positioned at the centre of the i -th coil. The voltage induced in the parallel coils is

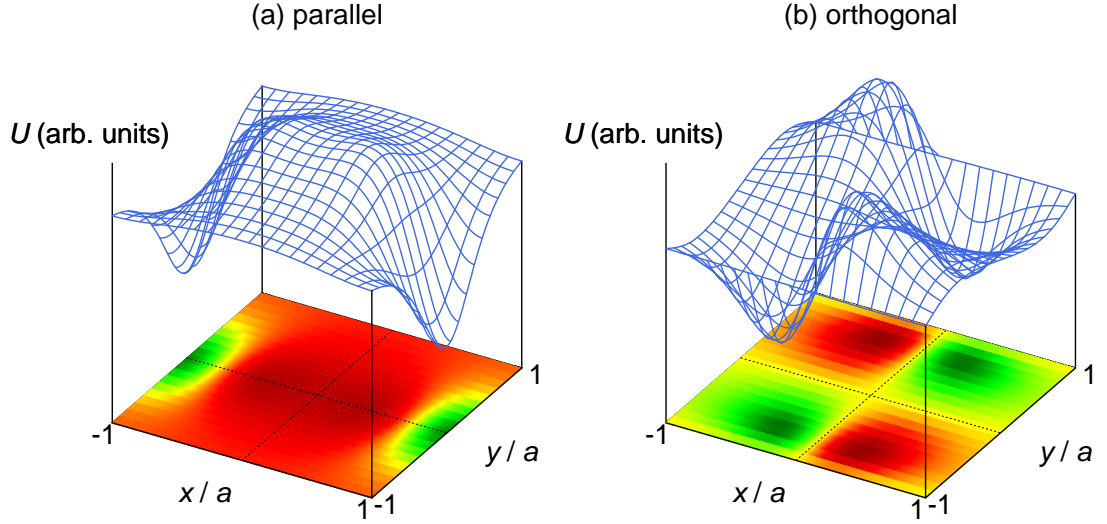


Figure 4.3. Sensitivity of the VSM in the x,y -plane. The spatial dependence of the output voltage is complex but the symmetry of the signal helps to centre the sample horizontally.

$$\begin{aligned} \hat{U}_{\parallel}(x, y, z) &\propto z_0 \omega [F(x - a, y, z - h) - F(x - a, y, z + h) \\ &\quad + F(x + a, y, z - h) - F(x + a, y, z + h)] \\ F(\Delta x, \Delta y, \Delta z) &= \Delta z \frac{m_{\parallel} (\Delta y^2 + \Delta z^2 - 4\Delta x^2) - m_{\perp} 5\Delta x \Delta y}{(\Delta x^2 + \Delta y^2 + \Delta z^2)^{7/2}}, \end{aligned} \quad (4.6)$$

where m_{\parallel} and m_{\perp} are two components of the magnetic dipole \vec{m} with respect to the external field; a and h define the horizontal and vertical position of the individual coils (cf. Fig. 4.2a). The expression for the orthogonal voltage \hat{U}_{\perp} can be derived by a transformation of coordinates, i.e., by simply exchanging $x \leftrightarrow y$ and $m_x \leftrightarrow m_y$ in (4.6).

4.2.2. Sample Alignment

Horizontal Calculations for U_{\parallel} and U_{\perp} for a sample magnetised parallel to the applied field ($m_{\perp} = 0$) are given in Fig. 4.3. The spatial dependence is relatively complex, but the symmetries are useful for centring the sample in the x,y -plane or for understanding measurements, where the sample is rotated and a precession of the sample rod cannot be excluded.

Vertical The same calculation for the sample moving along the z -axis is depicted in Fig. 4.2b. The sample is centred at the shallow minimum on top of the peak. Such a measurement was used to identify the parameters a , h of the pick-up coil system by fitting (4.6) and were found to be $a \approx 14$ and $h \approx 10$ mm.

Angular No simple strategy is available for the angular alignment and sample specific properties such as its geometry must be exploited to position it. In thin films the currents flowing in the a,b -plane necessarily create the main contribution to the magnetic moment for pure geometrical reasons. Consequently, the magnetic moment is to great accuracy always parallel to the c -axis of the film. Once magnetised, the angular alignment is best performed in the remanent state, where $m_{\parallel} = m \cos(\phi)$ and $m_{\perp} = m \sin(\phi)$. Rotating the sample and nulling m_{\perp} , which shows a pronounced angular dependence, is therefore more advisable than maximising m_{\parallel} .

The remaining angular deviation can be calculated from both components. As in most cases only the parallel component is evaluated, even a 5° misalignment creates an insignificant error ($\cos(5^\circ) \approx 0.996$) and the angular orientation is in fact fast and easy.

4.2.3. Calibration

Only basic electrodynamics is required to calculate the proportionality constant between the induced voltage and the magnetic moment, even if one accounts for the finite geometry of the coils. However, the convenient and reliable way of calibration against a reference sample is usually undertaken.

4.2.4. Oxford Instruments MagLab VSM

The Oxford Instruments MagLab VSM is equipped with a 5 T split coil magnet, which is horizontally aligned; no persistent mode was foreseen for the magnet. The sample can be rotated around the vertical z -axis and both components of the magnetic induction, parallel and orthogonal to the applied field, can independently be measured. Although the resolution of the device is significantly lower (roughly 10^{-7} Am^{-2}) compared to a SQUID magnetometer, it is considered as a fast measurement technique because the measurement time is determined by the integration period of the lock-in amplifier. At a sweep rate of 0.5 T/min and an integration period of 0.3 s, which were used throughout this work unless otherwise stated, the field averaged out in this time is approximately 2.5 mT, which is acceptably low.

The electric field generated by sweeping the magnetic field can easily be estimated in a simple model. In cylindrical coordinates (the magnetic field is parallel to the z -axis, H_z) the electric field has only an azimuthal component, E_θ , because of the symmetry of the problem. Integrating Faraday's law, using a path along the circumference of a circle with radius r , results in

$$E_\theta = \mu_0 \frac{r}{2} \frac{dH_z}{dt}, \quad (4.7)$$

where dH_z/dt refers to the sweep rate of the magnetic field. Substituting a typical value of 2 mm for the sample's radius, the electric field is calculated to be approximately 0.1 $\mu\text{V}/\text{cm}$. This is considerably higher than in SQUID measurements and a factor of 10 less than the 1 $\mu\text{V}/\text{cm}$ criterion applied in transport experiments. Furthermore, the electric field is not constant and rises linearly from zero at the centre to its maximum value at the sample edge.

4.3. Transport measurements

4.3.1. 17 T-system

The highest magnetic induction of all transport systems is reached in the 17 T-system. In standard operation, i.e., without pumping the helium bath in which the magnet is immersed, fields of up to 15 T can be applied to the sample. Because the solenoid is coaxial with the variable temperature insert (VTI), rotating the sample is mechanically difficult and was therefore not implemented in the sample holder, which is used to measure thin films and coated conductors. The sample can be mounted with either the a,b -plane or the c -axis parallel to the magnetic field. In these configurations a resistive determination of the irreversibility line can be undertaken for the two main field directions. Throughout spring loaded contacts were used, which pressed a thin In foil to the top sample surface, to establish the electrical contacts for four-point measurements.

4.3.2. 6 T-system

Due to the split coil geometry of the magnet the anisotropy of the critical current density can be determined in the 6 T-system. The probe represents a two-axis goniometer and by rotating the sample every direction of the magnetic field with respect to the sample's crystallographic system can be established. Furthermore, the Lorentz force, which is a function of the angle between the transport current

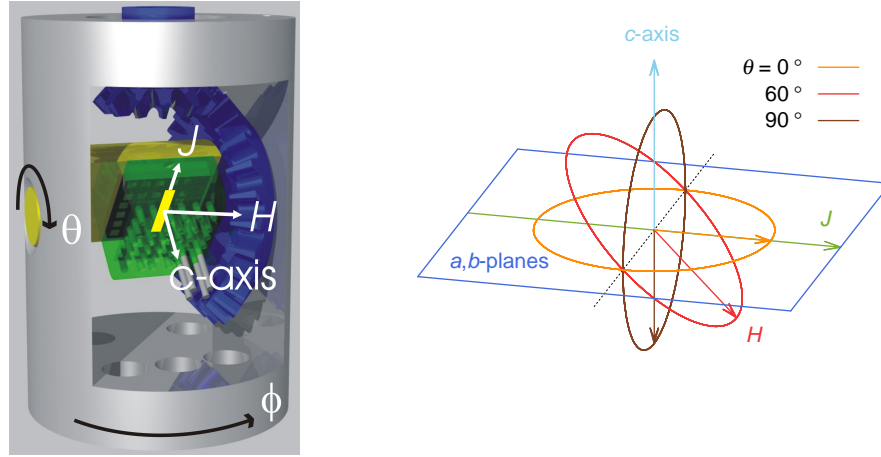


Figure 4.4. Definition of the angles in the 6 T-system. **(Left)** Schematics of the setup. (Courtesy of R. Schöppel). **(Right)** The angle between the plane, in which the magnetic fields is rotated by ϕ , and the a,b -planes of the film is controlled by θ . The arrows indicate the direction of the applied field if $\phi = 0$.

density \vec{J} flowing in the a,b -plane and the external magnetic induction, can be varied in this way.

The left panel of Fig. 4.4 shows a schematic view of the setup. In the coordinate system of the magnet (the x -axis is parallel to the applied field H , the z -axis identical to the symmetry axis of the VTI and the y -axis orthogonal to both) the current is directed with respect to the magnetic field by a θ -tilt around the y -axis followed by a ϕ -rotation around the z -axis; both angles are zero, if the current is parallel to the magnetic induction. In this coordinate system the parametrisation of \vec{J} reads

$$\vec{J}(\theta, \phi) = J \begin{pmatrix} \cos(\phi) & \sin(\phi) & 0 \\ -\sin(\phi) & \cos(\phi) & 0 \\ 0 & 0 & 1 \end{pmatrix} \cdot \begin{pmatrix} \cos(\theta) \\ 0 \\ \sin(\theta) \end{pmatrix} = J \begin{pmatrix} \cos(\phi) \cos(\theta) \\ -\sin(\phi) \cos(\theta) \\ \sin(\theta) \end{pmatrix} \quad (4.8)$$

and the magnitude of the Lorentz force density is calculated to be

$$f(\theta, \phi) = \mu_0 |\vec{J} \times \vec{H}| = \mu_0 J H \sqrt{\sin(\theta)^2 + \sin(\phi)^2 \cos(\theta)^2}, \quad (4.9)$$

showing that $\phi = \theta = 0$ is the force free configuration. In the special cases $\phi = 90^\circ$ and $\theta = 90^\circ$ the sample is subjected to the maximum Lorentz force

regardless of the other angle; standard anisotropy measurements $J_c(\phi)$ use the latter.

The right panel of Fig. 4.4 illustrates how the magnetic field transfers into the crystallographic system of the sample. It provides better insight into the working of the setup: θ determines the angle between the plane, in which the magnetic field is rotated by ϕ , and the a,b -planes of the film.

Because a sophisticated mechanical design limits the available sample space, only patterned films (see section 3.4) with lateral dimensions below $1 \times 1 \text{ cm}^2$ can be characterised. The maximum current of about 3 A is limited by the spring loaded contacts and the wiring feeding the current to the sample.

4.3.3. Electromagnet

For a characterisation of coated conductors at their designated operating temperature of 77 K and in moderate fields of up to 1.4 T, an electromagnet can be used. The probe is equipped with only one axis of rotation and the sample is mounted in maximum Lorentz force configuration (the current always flows perpendicular to the applied magnetic field). In contrast to the other transport systems, which employ a gas-flow cryostat to vary the temperature, the sample is immersed in liquid nitrogen. This is beneficial, if excessive contact heating obstructs the measurements, because of the available cooling power. The system is particularly suited for a comparison with magnetoscan measurements, which are carried out in liquid nitrogen as well (see section 6.2.1).

4.4. Scanning Hall probes

The experiments discussed so far measure only a single quantity as a function of the external parameters, such as temperature of field. Both, the magnetic moment determined in a SQUID or VSM and the voltage drop in a transport experiment, result from critical currents flowing in the entire volume of the sample. Consequently, the evaluated critical current density is a global material parameter, because spatial variations cannot be considered.

Scanning Hall probes are particularly useful to resolve the local properties of a film by mapping the magnetic induction generated by the supercurrent flow in the sample. Generally $B = \vec{B} \cdot \vec{e}_z$, which is the component perpendicular to the top surface, is assessed at a certain constant distance d (gap).

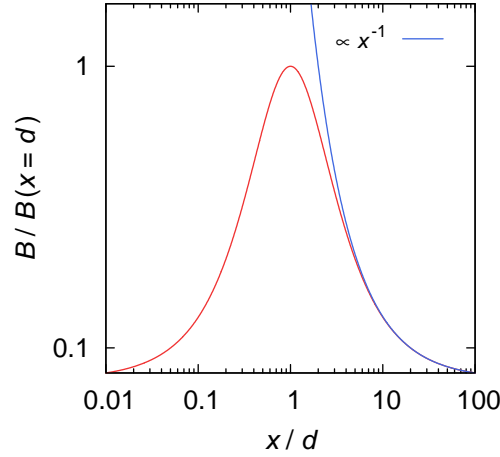


Figure 4.5. Magnetic field in z -direction created by a current flowing in y -direction at the Hall probe position x . Due to symmetry the sensor does not detect underneath currents ($x = 0$); the sensitivity peaks when the lateral distance is equal to the scanning gap ($x = d$).

In the simple case of a straight wire the magnetic induction at the Hall probe position is calculated to be

$$B(x) \propto I \frac{x}{x^2 + d^2}, \quad (4.10)$$

where the current I flows in y -direction and the Hall probe is moved along x . The above equation already demonstrates the important features of the experiment, namely, currents flowing directly underneath the sensor ($x = 0$) cannot be detected, and the peak sensitivity is reached at a distance equal to the scanning gap $x = d$. For larger distances ($x \gg d$) the signal decreases approximately as $B(x) \approx 1/x$. In essence, the Hall probe is more sensitive to the nearby currents, thus enabling the assessment of position dependent information.

It is important to notice that averaging effects are unavoidable due to the finite dimension of the active area, but are negligible as long as a pixel of the scanning mesh is larger than the active area [20]. This condition is easily fulfilled because high resolution Hall probes with an active area below $50 \times 50 \mu\text{m}^2$ are used in all the experiments.

4.4.1. Scan systems

The scanning device developed in [21] was used. The experiment is fast and a high density of points can be assessed in a short time (more than 10 000 points per

hour), making Hall scans ideal for a swift characterisation of the homogeneity of films and coated conductors. The Hall probe is glued onto a cylindrical holder in order to protect the active area. This security measure is mainly responsible for the uncertainty in the gap d , which is roughly 0.1 – 0.2 mm. Stepper motors drive three axis, which span an orthogonal coordinate system, and the probe is positioned with a spatial resolution of 10 μm .

Hall maps Thanks to the relatively small penetration field (cf. section 2.1.1), thin films can be activated by a strong permanent magnet such as NdFeB ($\mu_0 M_r > 1 \text{ T}$). The sample is either cooled in the magnet's field or magnetised when immersed in liquid nitrogen. The removal of the permanent magnet subjects the entire volume of the sample to a change in magnetic induction much larger than B^* and the critical state is established in the entire volume. This technique allows a quantification of the local current densities, which is elaborated in chapter 7.

Magnetoscan For large conductor dimensions the diameter of the permanent magnet is too small to induce supercurrent flow in the entire sample—an alternative way to activate the currents is necessary. The magnetoscan overcomes this problem by moving the permanent magnet together with the Hall probe during the scan. In this way a Bean-like current distribution similar to a magnetisation in a large homogeneous field is generated in the area mainly contributing to the total signal. More details are given in chapter 6, where the interpretation of the magnetoscan signal is discussed together with typical measurements and compared to other techniques.

4.5. TRIGA Mark-II reactor

The TRIGA Mark-II is a pool-type nuclear reactor located in the institute. It is a low power research facility (in continuous operation only 250 kW are reached) and serves primarily as neutron source, providing a total neutron flux density of up to $2.1 \times 10^{17} \text{ m}^{-2}\text{s}^{-1}$ in the central irradiation facility (CIF) [22]. The ensemble of neutrons is grouped into three categories, thermal ($E < 0.55 \text{ eV}$), epithermal, and fast ($E > 0.1 \text{ MeV}$) neutrons.

Fast neutrons generate collision cascades upon hitting a nucleus, i.e., surrounding lattice atoms are strongly displaced. After the impact an amorphous area is left, which was estimated by TEM to be about 1 – 5 nm [23]. These spherical defects are randomly distributed and their density is proportional to the fast neutron fluence

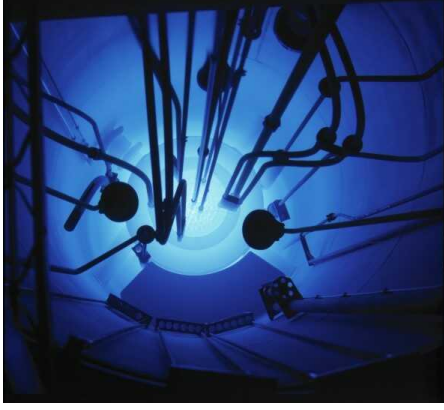


Figure 4.6. Čerenkov radiation in the pool of the TRIGA MARK-II research reactor.

the sample is subjected to. The fluence of fast neutrons is $7.6 \times 10^{16} \text{ m}^{-2} \text{ s}^{-1}$ [22]; a “reactor workday”, which amounts to a fluence of $2 \times 10^{21} \text{ m}^{-2}$ is equal to a cascade density of 10^{22} m^{-3} .

Whilst the defects created by the fast neutrons considerably change the irreversible properties of high-temperature superconductors (cf. the brief review at the beginning of chapter 11), the damage created by the thermal neutrons as well as the ubiquitous gamma radiation do not play a role for flux pinning in YBCO.

4.5.1. Irradiation procedure

For safety reasons, an assessment of the sample’s radioactivity after the irradiation and the dose rate released while handling the sample is absolutely mandatory. The activation products as well as the calculation of their lifetime and activity are based on neutron activation tables of the elements. If necessary, sufficient time for decay must be taken into account. This is especially the case for coated conductors on metallic substrates containing elements such as W and Au.

The sample is then sealed in a quartz tube filled with helium gas and transferred inside an Al capsule into the CIF. The helium atmosphere is a protective measure and underpressure (around 300 mbar) is necessary due to the temperature rise during sealing the quartz tube. The temperature during the irradiation stays below 60°C , and oxygen diffusion, which would decrease the transition temperature, does therefore not occur. After the irradiation the sample remains in the reactor pool until it can safely be handled.

4.6. Focussed Ion Beam

A focused ion beam (FIB) system is a standard micro-machining tool, which allows to structure samples on the nanometre scale. It consists of a high-resolution liquid

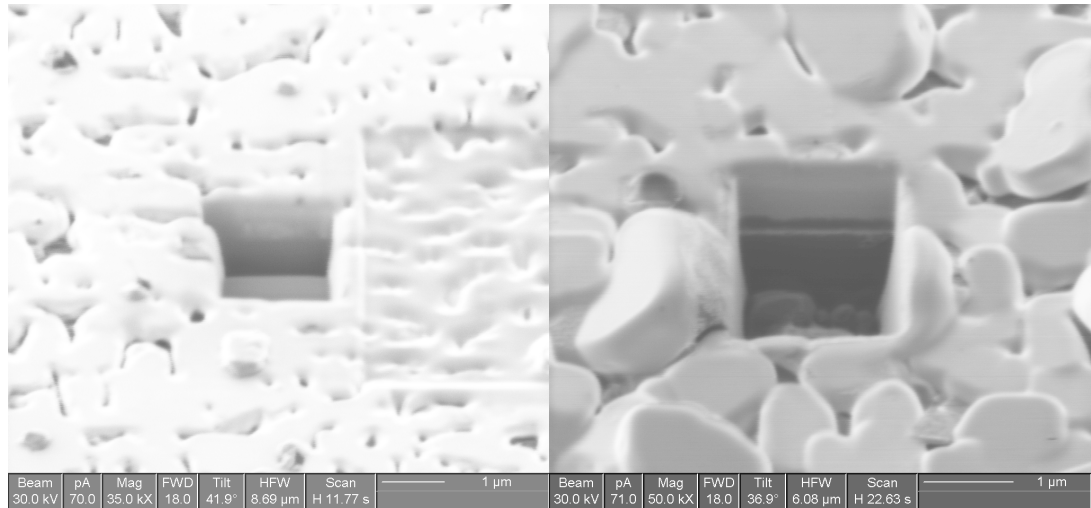


Figure 4.7. SEM images of HLPE samples made in an FIB system. (Left) YBCO appears bright and is hard to distinguish from the BaO-CuO flux covering the top sample surface. The quadratic area right to the hole is a result of the continuous imaging during the focusing process. The STO substrate appears dark. (Right) YBCO on metallic NiW. Individual buffer layers are clearly visible.

metal source, which provides the focused beam. The ions (usually Ga) are directed onto the sample surface and their impact sputters material at the focal point of the beam. Due to the interaction of the ions with the sample, secondary electrons are emitted from the surface. Their spectrum is detected by conventional SEM equipment and results in a high-resolution image when the beam is scanned across the specimen.

4.6.1. Thickness measurement in an FEI FIB200 system

The FEI FIB200 system was used to determine the thickness of the YBCO layer in HLPE samples, as follows. Firstly, an appropriate part of the sample, such as the contact pads, is selected to avoid sputtering sensitive regions, e.g., the tracks, during the imaging process. The selected area is then centred in the eucentric point of the stage, which guarantees that the field of view is maintained during tilts and the image remains focused. In the next stage a hole is milled by continuously scanning a small area of typically around $1 \mu\text{m}^2$ with the ion beam. Meanwhile, the current of emitted secondary electrons is monitored, which is characteristic for the material currently removed. When the beam starts to sputter the sample substrate, i.e., when an abrupt change in the current is observed, the procedure is stopped. In a second run one face of the hole is cleaned. Afterwards the stage of the instrument is tilted (about 45°) to image the entire cleaned face down to

the bottom (see Fig. 4.7). Finally, the distance between the individual layers at the actual perspective is measured and the thickness is calculated from the tilt angle.

Chapter 5.

Evaluation methods

5.1. Magnetisation critical current density

Within the widely used Bean model [24] a so-called critical current density

$$\vec{J}_c = \vec{\nabla} \times \vec{M} \quad (5.1)$$

is used to describe the gradient of the magnetisation \vec{M} established by the spatial variation of the vortex density (cf. chapter 1). This single material parameter characterises the flux pinning properties of the material and is assumed to be independent of the magnitude and direction of the magnetic induction \vec{B} .

Applying (5.1) to a thin film magnetised $H \parallel c$ has a simple solution, if the planar currents circulate in the same direction in the entire volume of the sample, i.e., if the last field change was greater than the penetration field. The magnetisation vanishes outside the sample (there are no flux lines); inside M is parallel to the c -axis and simply a function of the distance to the closest sample edge

$$M(x, y) = \vec{M}(x, y) \cdot \vec{e}_z = \begin{cases} J_c(a/2 - |x|) & \text{if } |x| - a/2 < |y| - b/2; \\ J_c(b/2 - |y|) & \text{if } |x| - a/2 \geq |y| - b/2. \end{cases} \quad (5.2)$$

(Here, a and b are the lateral dimensions of the film; the crystallographic c -direction is parallel to the z -axis.) The rooftop like magnetisation profile is depicted in Fig. 5.1 together with current streamlines, which are obtained by evaluating (5.1). Calculating the volume under the rooftop for a film of thickness c results in the irreversible magnetic moment

$$m_{\text{irr}} = \iiint dx dy dz M(x, y) = J_c \frac{ab^2c}{4} \left(1 - \frac{b}{3a} \right), \quad (5.3)$$

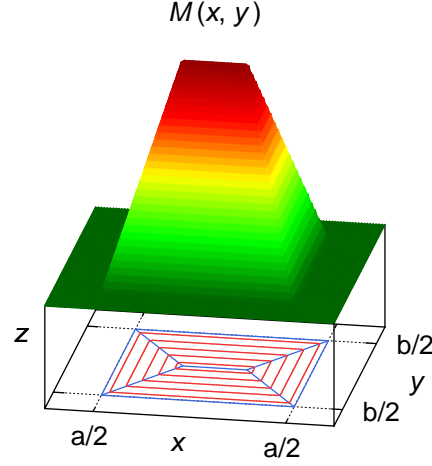


Figure 5.1. Bean model for an infinitely long bar. The magnetisation M is a function of the distance to the closest sample edge and decreases towards the centre of the sample. The gradient of the magnetisation is constant, which results in equidistant streamlines of the critical current density J_c .

which relates the magnetic moment to the critical current density and allows calculating the material constant J_c from magnetisation data.

The irreversible magnetic moment m_{irr} , which represents pinning in the material, must be separated from the reversible contribution. This is achieved by selecting two branches of a hysteresis loop, where either H or $E \propto \partial_t H$ change sign, and by calculating

$$m_{\text{irr}}(H) = \frac{|m(+H) + m(-H)|}{2} = \frac{|m(H|_{+\partial_t H}) - m(H|_{-\partial_t H})|}{2} \quad (5.4)$$

with all other parameters held constant. In this case the reversible magnetisation cancels due to the symmetry $m_{\text{rev}}(H) = -m_{\text{rev}}(-H)$. The average critical current density of the sample is then calculated to be

$$J_c(H) = \frac{4m_{\text{irr}}(H)}{ab^2c \left(1 - \frac{b}{3a}\right)}. \quad (5.5)$$

5.1.1. Limitations of the Bean model

It is important to notice that the evident field dependence of the critical current density $J_c(H)$, determined by applying the Bean model, does not per se contradict the initial assumption of a field independent critical current density. The application of the model only requires that the variation of the magnetic induction within the

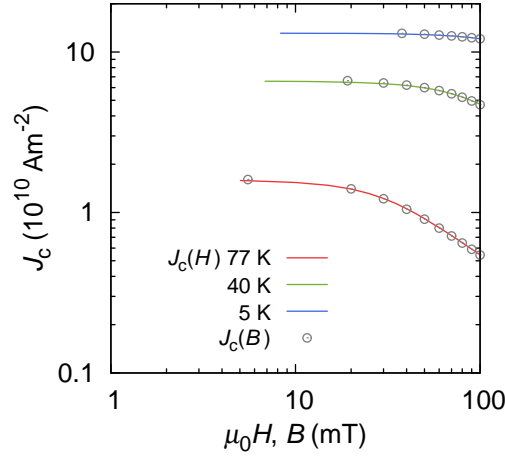


Figure 5.2. Evaluation of magnetisation loops taking self-field into account. At low applied fields the self-field prevails and $J_c(B)$ clearly differs from $J_c(H)$. When the temperature is lowered, the effect becomes more pronounced as J_c rises. At high fields the self-field contribution can be neglected and $J_c(B)$ matches $J_c(H)$. The field dependence of J_c further reduces the sample's self-field.

sample is negligibly small. As research magnets provide highly homogeneous fields, only the field created by the critical current flowing in the sample (self-field, B_{sf}) can violate this vital assumption.

Especially at zero applied field, $H = 0$, it is obvious that $J_c(H)$ and $J_c(B)$ will differ as the magnetic induction B is now solely due to the self-field (usually of the order of a few mT in thin films). Consequently, a more elaborated technique is necessary to evaluate magnetisation loops at low fields ($\mu_0 H \lesssim B_{\text{sf}}$). This is accomplished by an evaluation procedure [25, 26], which accounts for the self-field by calculating a weighted mean of the induction created by the supercurrents, \bar{B}_{sf} , after executing the standard evaluation of the hysteresis loop. In this way the procedure is able to replace the applied induction $\mu_0 H$ by the average magnetic induction, i.e., the sum of external and self-field, $B = \mu_0 H + \bar{B}_{\text{sf}}$. Evidently, the procedure is most effective at low applied fields, where the self-field prevails and $J_c(H)$ differs from $J_c(B)$ (cf. Fig. 5.2). At high fields, on the other hand, $J_c(B)$ becomes equal to $J_c(H)$ and the self-field contribution can be disregarded (the decreasing $J_c(B)$ further diminishes it). For the same reason demagnetisation is only significant at low fields, because it is in essence a self-field effect.

5.1.2. Granularity

In order to evaluate magnetisation measurements, the length scale of current flow must be known. It does not necessarily agree with the sample dimensions: large defects, for example, will cause substantial deviations of the current flow and the application of (5.5) will thus fail. Hall scans are a valuable tool to resolve such irregularities and were consequently performed before SQUID or VSM measurements.

Apart from inhomogeneities, more fundamental sample properties control the flow of the supercurrents. In particular in the presence of granularity, induced e.g. by a metallic substrate, the current will flow on two length-scales: within the grains as well as between the grains, crossing the grain-boundaries and spanning the entire sample. Due to the nature of grain-boundaries their magnitude can be vastly different [27] and it is not clear which contribution is dominant in magnetisation measurements. However, an inspection of (5.3) shows that $m \propto J_c l^3$, where l represents the typical lateral length scale. Hence, the magnetic moment of the grains (G) relative to the grain-boundary network (GB) is

$$\frac{m_G}{m_{GB}} = \frac{J_c^G}{J_c^{GB}} \left(\frac{l_G}{l_{GB}} \right)^3 \underbrace{\left(\frac{l_{GB}}{l_G} \right)^2}_{\text{Number of grains}} = \frac{J_c^G}{J_c^{GB}} \frac{l_G}{l_{GB}}. \quad (5.6)$$

The ratio l_G/l_{GB} is typically more than 100, much larger than the ratio of the current densities in all but samples with high-angle grain-boundaries. Thus the main contribution to the total magnetic moment stems from the currents flowing across the grain-boundaries, which enables a comparison to transport measurements.

5.1.3. Ferromagnetic substrates

A further source of unwanted background signal is the Ni contained in the substrate of coated conductors. Its signal can, depending on the applied field, temperature, and sample quality, exceed the superconductor's magnetic moment. It is therefore important to measure the sample at a temperature above the superconducting transition to check if the substrate signal is hysteretic, which would make the above evaluation scheme inapplicable. If no significant hysteresis is observed, which was indeed the case for all the samples, the ferromagnetic background is eliminated by the evaluation procedures described above, because it obeys the same symmetries as the reversible magnetisation.

For samples with low critical current the ferromagnetic background signal can prevail in the entire field and temperature range. Especially at elevated temperatures and higher fields it becomes increasingly hard to isolate the superconductor's signal even in a SQUID magnetometer, simply because the relative magnetic moment is so small. As a consequence it is desirable to reduce the background as much as possible. Any attempt to cut the sample will, however, fail since the magnetic moment of the superconductor scales with $m_{\text{sc}} \propto l^3$, while the ferromagnet shows a weaker dependence $m_{\text{ferro}} \propto l^2$. Hence, one should always aim to maximise the size of sample, in order to reduce the substrate's relative signal.

5.2. Transport critical current density

In the flux creep regime (cf. chapter 1) the assumption of a logarithmic dependence of the activation energy on the current density leads to a power-law

$$U = U_c \left(\frac{I}{I_c} \right)^n, \quad (5.7)$$

which describes the I - V curve in terms of the exponent n -value and the critical voltage U_c . Thus, an arbitrary electric field criterion of $E_c = U_c/d = 1 \mu\text{V}/\text{cm}$ is commonly used to define the critical current, given the voltage contact spacing d . No physical reason is available for this choice; it simply results from experimental convenience: at a typical voltage contact spacing of several millimetres the voltage criterion is well above the experimental noise (typically $\approx 100 \text{ nV}$). For patterned thin films with a track length below 1 mm the above criterion is not feasible and a voltage criterion of $U_c = 1 \mu\text{V}$ was applied as an alternative.

It has to be noted that, due to the steepness of the I - V curve, the criterion has only a minor effect on the magnitude of I_c and all the features of the critical current anisotropy are usually preserved (see Fig. 5.4). This may be proved by inserting two different criteria into (5.7). The ratio of the two resulting critical currents is

$$\frac{I_{c1}}{I_{c2}} = \left(\frac{U_{c1}}{U_{c2}} \right)^{1/n(\phi)} \quad (5.8)$$

and thus weakly dependent on the voltage criterion as long as n is high (typically around 10 in the superconductors investigated here). Further, the shape of the anisotropy curve will remain unchanged, if n does not depend on the angle ϕ .

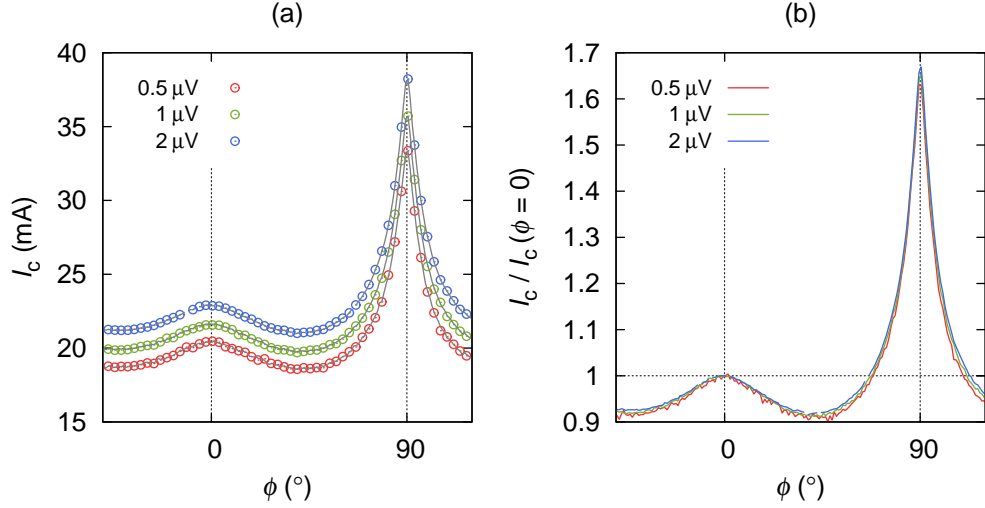


Figure 5.3. Role of the voltage criterion in defining I_c . (a) The application of different voltage criteria has only a minor effect on $I_c(\phi)$. The intersection of the I - V curve (points) with the voltage criterion and curve fitting (grey lines) result in almost identical values. (b) The features of the anisotropy are preserved due to the steepness of the I - V curve (n -value ≈ 7 .)

5.2.1. Determination of the critical parameters

In the presence of voltage noise comparable to the voltage criterion U_c the most stable way to identify I_c is to intersect U_c with the interpolation between the last point below U_c and its successor. Moreover, the parameters I_c and the n -value can be identified by non-linear least squares fitting as displayed in Fig. 5.4 for a curve with a large number of datapoints. The graph shows that (5.7) satisfactorily describes the measurement in the entire current range. Furthermore, the fit error is below $\approx 0.1 \mu\text{V}$ and approximately independent of the current (see inset of Fig. 5.4). This points to a constant voltage noise due to thermal fluctuations or the interference of external signals.

The power-law is revealed on a double logarithmic scale and, if valid, the I - V curve has linear slope, $\log(U) \propto n \log(I)$, determined by the n -value (see Fig. 5.4(b)). This promotes the rather geometrical approach of fitting a linear function on a log-log scale to obtain the n -value, as is suggested in [28]. However, it is important to note that this procedure attempts to *approximate* the I - V curve in the low voltage range; in this case the n -value is only the exponent of a reasonably simple analytic representation of the curve. This work follows a different approach: it is assumed that the n -value reveals information about pinning and thus tries to *identify* the free parameter of a physical model.

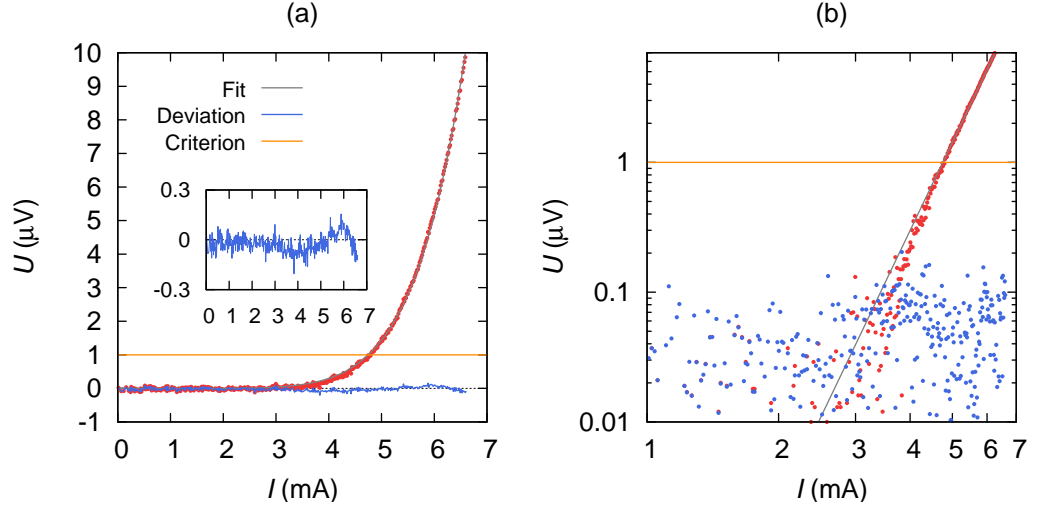


Figure 5.4. (a) Identification of the n -value by a least squares fit showing that the power-law represents an excellent fit to the data. The fit error does not increase at higher currents and is roughly $0.1 \mu\text{V}$. (b) The power-law becomes immediately evident on a double logarithmic scale.

Although the difference is relatively small, the parameter identification should consequently be carried out on a linear rather than a logarithmic scale for the following reasons: First, a logarithmic scale requires an arbitrary threshold voltage below which the data are rejected because of negative voltages; a linear scale does not require such a cut-off. Second, and most important, measurement errors in a least squares regression must always be accounted for. The voltage noise is, however, compatible with a constant, absolute error, which can be disregarded on a linear voltage scale. In contrast, if one does so on a logarithmic voltage scale (the current scale has no effect) the measurement errors are implicitly rescaled and the lower voltages are emphasised (because their errors are now relatively lower) without any rigorous physical justification.

A logarithmic representation may, however, serve to find a suitable initial guess for the n -value

$$n_0 = \frac{\log(U_{\max}/U_c)}{\log(I_{\max}/I_c)} \quad (5.9)$$

using the data point with the highest voltage of the I - V curve; a good starting value I_{c0} is, of course, the critical current determined by the intersection. A proper measure of the fit error is the mean deviation from (5.7) and the fit is rejected, if it exceeds a certain fraction of the voltage criterion U_c . The above procedure

along with the subtraction of bias voltages was implemented using `Scilab` [29]; the routine `datafit` is employed to identify the free parameters.

If successful, the critical current obtained by fitting the power-law usually shows good agreement with the critical current determined by intersection (cf. Fig. 5.3). Once I_c is evaluated, the average critical current density

$$J_c = I_c/A \quad (5.10)$$

can be calculated if the sample cross-section A is known.

5.3. Irreversibility line

The irreversibility line (IL) indicates the field and temperature domain, above which the vortex lattice is not able to withstand a driving force, i.e., a flux density gradient or a transport current is maintained only at the expense of dissipation resulting from the movement of the vortices. Although the definition is quite clear, the Anderson-Kim flux-creep theory predicts the occurrence of dissipation also at the lowest driving forces due to thermally activated depinning (cf. chapter 1). As a consequence, the detection of the irreversibility line depends on the measurement technique and the resolution of the device in use. It is therefore rather ill-defined, but it is elucidating to examine the thermally assisted flux flow (TAFF) regime by transport measurements, particularly before and after neutron irradiation.

There is no generally accepted experimental procedure for a resistive determination of the irreversibility line. Commonly temperature sweeps at a certain constant background field are employed and the voltage drop across the sample is measured. In any case, a specification of the current density J and the electric field E is required to define the irreversibility line.

One approach is to mimic transport J_c -measurements and to use an electric field criterion of $E_c \approx 1 \mu\text{V}/\text{cm}$ but to apply a current density orders of magnitude lower than the sample's critical current density (typically $J \approx 10^6 \text{ Am}^{-2}$ was used). Although the limits of applicability are explored in this way, the result is not practical, as any application will require to operate the conductor at more stable conditions (where it is not prone to thermally activated depinning).

In this work it was attempted to probe the vortex state at a minimal excitation of the system, i.e., by reducing the current as much as possible. This was achieved by setting a current, which creates a voltage drop well above the noise level, when the sample is in the normal conducting state just above T_c . If the driving force is

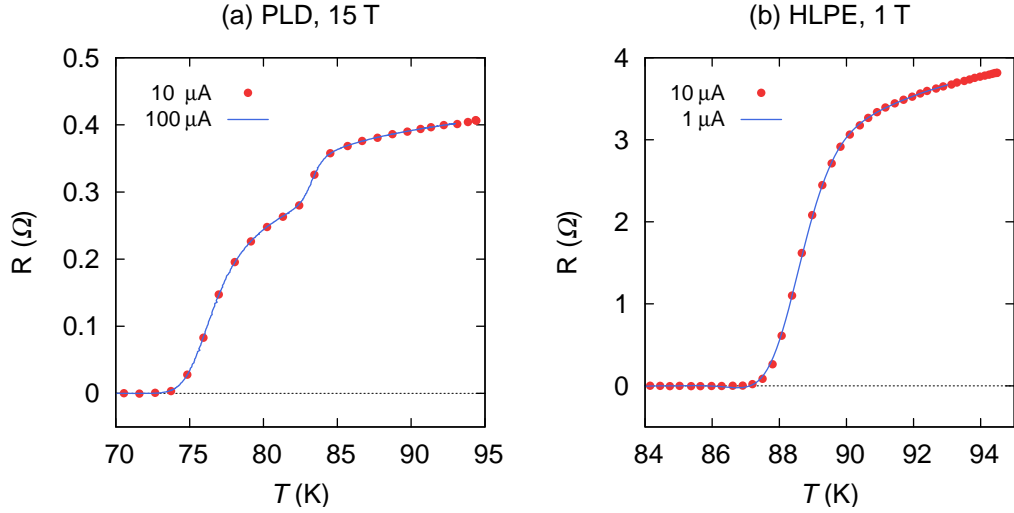


Figure 5.5. Determination of the irreversibility line. In the TAFF regime superconductors show ohmic behaviour. The resistivity was found to be independent of the current in PLD films at 15 T (a) and in HLPE samples at 1 T (b) supporting a resistive criterion to determine the irreversibility line.

now sufficiently small, one expects the sample to be in the thermally assisted flux flow (TAFF) regime with its characteristic ohmic behaviour (cf. chapter 1). Using a resistive criterion instead of a voltage criterion is thus in full agreement with the physics of the vortex lattice. In this work, 10% of the resistance, where the curve starts to deviate from linear behaviour and superconductivity becomes effective, was used to define T_{irr} (see Fig. 5.6).

Moreover, the evaluation procedure is independent of the current density in the sample, which effectively rules out problems with uncertain or even unknown sample dimensions hampering the application of a J_c criterion, and different samples can safely be compared. That the resistance does indeed not change with the current is representatively depicted in Fig. 5.5 for two samples at 1 and 15 T, respectively.

5.4. Transition temperature

5.4.1. Transport

A number of different evaluation methods is available to determine the critical temperature and no particular argument highlights any of them. Generally, any method can be applied, which reliably quantifies the properties already evident in a plot of the data. In this work the resistive T_c measurements were evaluated

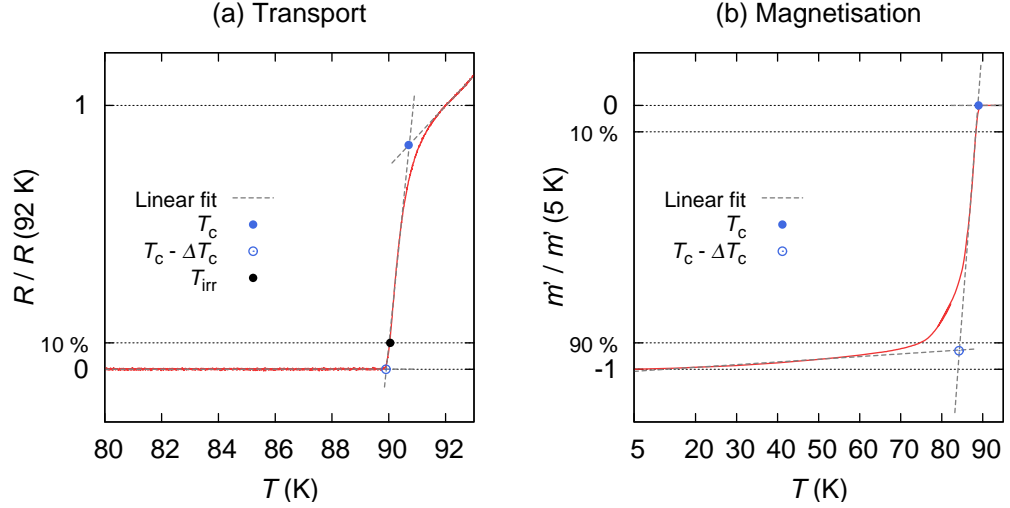


Figure 5.6. Comparison of different evaluation methods for T_c and ΔT_c . (a) Linear fits and intersection were used to evaluate transport measurements. If the transition is sharp, T_c is close to $T_{irr}(H = 0)$. (b) A similar scheme can be applied to magnetisation measurements. The results of the experiments differ if the sample is inhomogeneous (indicated by the double peak in m'' and the broad tail of m' at low temperatures). In such a case the tangent criterion compares better to resistive measurements as evaluating 10 % and 90 % of the Meissner signal, especially with regards to ΔT_c .

by employing a so-called tangent criterion. Here, the intersection of a linear fit to the steepest part of the transition with a linear extension of the normal state resistance defined T_c ; by extrapolating to zero resistance the transition width ΔT_c was found. The T_c value determined in this way is usually somewhat higher than the irreversibility temperature at zero field, $T_{irr}(H = 0)$, as defined by the resistance criterion discussed in the previous chapter. But the difference is very small, if the superconducting transition is sharp as depicted in Fig. 5.6.

5.4.2. Magnetisation

The same scheme was applied to evaluate SQUID AC measurements and fits to the settling Meissner tail at low temperatures and the normal state signal were used in this case. Although the procedure is technically identical to the evaluation of transport measurements, the results can differ significantly (cf. Fig. 5.6), because different processes are observed. In a transport measurement a single superconducting path, able to support the applied current, is sufficient to short both voltage contacts and the percolative path with the highest T_c determines the resistive transition. All other current paths play no role and weak spots with low critical

temperatures are consequently not detected. In magnetisation measurements, on the other hand, currents from the entire volume of the sample add up to the magnetic moment and the method is more susceptible to inhomogeneities with lower T_c , thus broadening the transition.

This makes a comparison of both methods difficult, especially if the sample is inhomogeneous. In such cases the tangent criterion, which utilises the steepest part of the transition, was found to compare better to resistive measurements, than, for example, evaluating 10 % and 90 % of the Meissner signal (cf. Fig. 5.6).

Part III.

Results

Chapter 6.

Magnetoscan

The magnetoscan, a device capable of swiftly characterising the homogeneity of the supercurrent flow in long superconducting tapes, was developed in cooperation with R. Fuger [30] and extends the existing Hall scan system [21]. This chapter contains the only magnetoscan measurements presented in this work; they are used to demonstrate the application of a simple interpretation scheme and for a comparison to other methods. Generally, standard Hall maps of the remanent state in a film are preferred, if the size of the samples is small enough, because the local current density can be calculated from the flux density profile (see chapter 7). But there is also a number of samples (not discussed here), which were important for investigating whether or not growth on a poly-crystalline substrate was successful. The magnetoscan was particularly helpful to map films, which were grown with partial success onto metallic tapes, because the most promising areas of a conductor are easily selected for further characterisation in this way.

6.1. Interpretation

The moving magnet induces a complex current distribution in the conductor and numerical methods are necessary to calculate it. An important result of the simulation employed in [31, 32] is that the currents are mainly directed parallel to the tape in an area of about the magnet's diameter, if the magnet is not too close to the tape surface. Further, the established current pattern has an odd symmetry in this region, i.e., the currents change sign at the centre of the conductor as one would expect from magnetisation experiments. Note that a change in field by at least $2B^*$ is required to erase the current distribution stemming from the last position of the magnet. As a consequence the most homogeneous currents flow at a position shifted towards the scanning direction and the optimal Hall probe position is therefore off-centre (see Fig. 6.1).

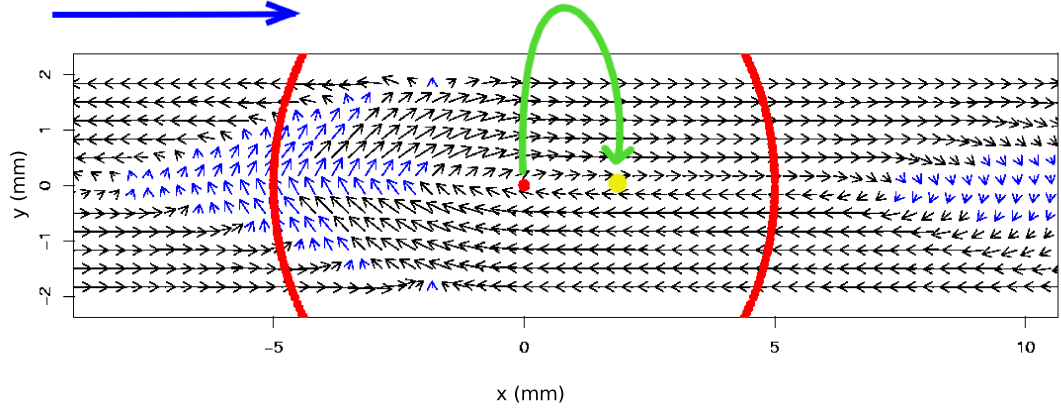


Figure 6.1. Simulation of the current distribution induced in a homogeneous tape during a magnetoscan (the scanning direction is indicated by the blue arrow). In an area of about the magnet's size (red circle) supercurrents flow parallel to the tape. Due to the movement of the magnet the currents are most homogeneous right to the magnet. Therefore, the optimum Hall probe position is off-centre in the experiment (yellow point). Here it senses a magnetic induction comparable to a magnetisation profile in a homogeneous magnetic field. (Courtesy of M. Zehetmayer.)

Despite the complexity of the current flow in the magnetoscan some basic properties can be grasped by simplifying the problem considerably. Let's assume that the current is thickness independent and can thus be replaced by a sheet current, flowing strictly parallel to the tape, $J_y(x, y) = 0$. Current conservation requires that the current density is a function of y only, $J_x = J_x(y)$, and the Biot-Savart law for the perpendicular field component $B = \vec{B} \cdot \vec{e}_z$ reduces to

$$B_z(y) = \frac{\mu_0 c}{2\pi} \int_{-a/2}^{a/2} dy' \frac{J_y(y')(y - y')}{(y - y')^2 + d^2}. \quad (6.1)$$

Here, a is the width and c the thickness of the tape whereas d represents the scanning gap. It becomes obvious in this special case that the magnetoscan senses a weighted signal of the currents passing through the cross-section and thus measures the local current carrying capability at the position right underneath the Hall probe.

If we further assume that the magnitude of the current density is constant and has odd symmetry, $J(y) = -J(-y) = J_c$, which implies that no net current passes through the actual cross-section, one finds

$$B_{\max} = (\mu_0 c J_c / \pi) \ln [1 + (a/2d)^2] \quad (6.2)$$

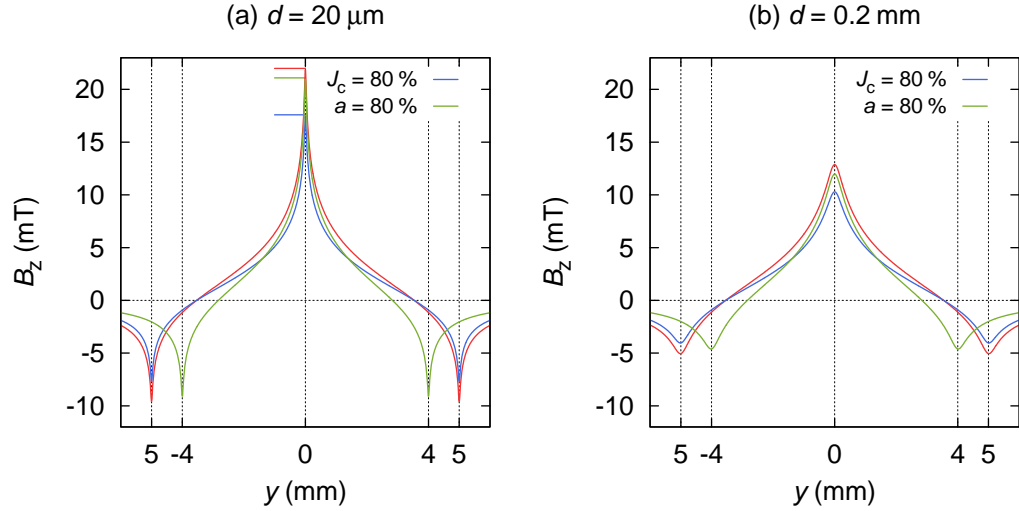


Figure 6.2. Field profile of a coated conductor carrying an odd current distribution $J(y) = -J(-y) = J_c$. Calculations of the perpendicular magnetic field $B_z(x)$ are for a model conductor (red), a conductor with J_c reduced by 20 % but identical width (blue), and with the same J_c , but 80 % of the width (green). The latter two configurations carry the same critical current. (a) For distances close to the tape top surface the maximum negative field precisely indicates the margins of current flow. The maximum positive field depends only weakly on the sample width and scales with J_c . (b) Same calculations for a more realistic distance. Although the extrema are smeared, the field profile still enables a determination of the actual tape width.

for the maximum field located above the centre of the conductor ($y = 0$). The fact that the signal has a maximum at this position and depends linearly on J_c , suggests a scan along the centre of the conductor for a fast characterisation of the tape, which is discussed in more detail in the following section.

Changes in the magnetoscan signal can be related to a decrease of the critical current density (possibly due to changing growth conditions), a reduced cross-section (resulting, e.g., from defects in the material or in the buffer layers) or a combination of both. The latter case is too complex for the simple model, but the first two cases can be distinguished, if the current flow is not too much distorted by the inhomogeneity and reasonably parallel in the neighbourhood of the Hall probe. Calculations based on (6.1) are depicted in Fig. 6.2 for a 1 cm wide conductor carrying a critical current density of 10^{10} Am^{-2} . Two defect scenarios are considered: in the first one J_c is decreased by 20 % while in the second one the width of the conductor is reduced to 80 %, which results in identical critical currents.

For distances very close to the sample top surface ($d = 20\ \mu\text{m}$) the sharp negative field peaks precisely indicate the width of the current distribution (see Fig. 6.2a). It is a peculiarity of the thin film geometry that the maximum trapped field in the centre depends mainly on the sheet current density $K_c = cJ_c$ and weakly on the tape width (cf. (6.2)). Weaker pinning (negative peaks coincide with sample edges, the trapped field is reduced) can easily be distinguished from a narrowed tape width (negative peaks shifted towards the centre, the trapped field is hardly affected), even if both configurations conduct the same critical current (see Fig. 6.2b).

The right panel shows results for a realistic scanning gap of $d = 0.2\ \text{mm}$. Although all the peaks are smeared, the maximum negative fields still coincidences with the tape edges. On the other hand the maximum field at the centre depends more strongly on the tape width. This emphasises the importance of a small scanning gap in the magnetoscan, besides the evident loss of signal strength with distance.

6.2. Comparison to alternative techniques

6.2.1. Transport measurements

In homogeneous conductors the magnetoscan signal along the centre of the conductor, the “central line scan”, is related to the critical current passing through the actual cross-section [31]. A comparison with transport measurements is thus of great interest to confirm that the technique is able to locate the position limiting the end-to-end current carrying capability of the conductor.

Such a measurement is displayed in Fig. 6.3. Two spots with high magnetoscan signal were used as current contacts (I_1, I_2). Three voltage pads were positioned in between: one is located in an area with low magnetic response and presumably lower critical current density (V_a); two contact a region with high magnetic response (V_b, V_c). Initially the critical current of the tape was determined using the outermost voltage contacts (V_a, V_b) and was found to be 13 A. The identical critical current was obtained when the voltage across the low response region was measured using pads (V_a, V_b). No voltage dropped between the contacts located in the area with high magnetoscan signal for currents of up to 15 A, showing indeed that the region, where the central line scan is lower, dissipates first [33].

Hence, the defects that act as bottle-necks for the current flow and consequently limit the end-to-end performance are easily identified by the magnetoscan. The method is thus particularly well suited for a swift and effortless characterisation of

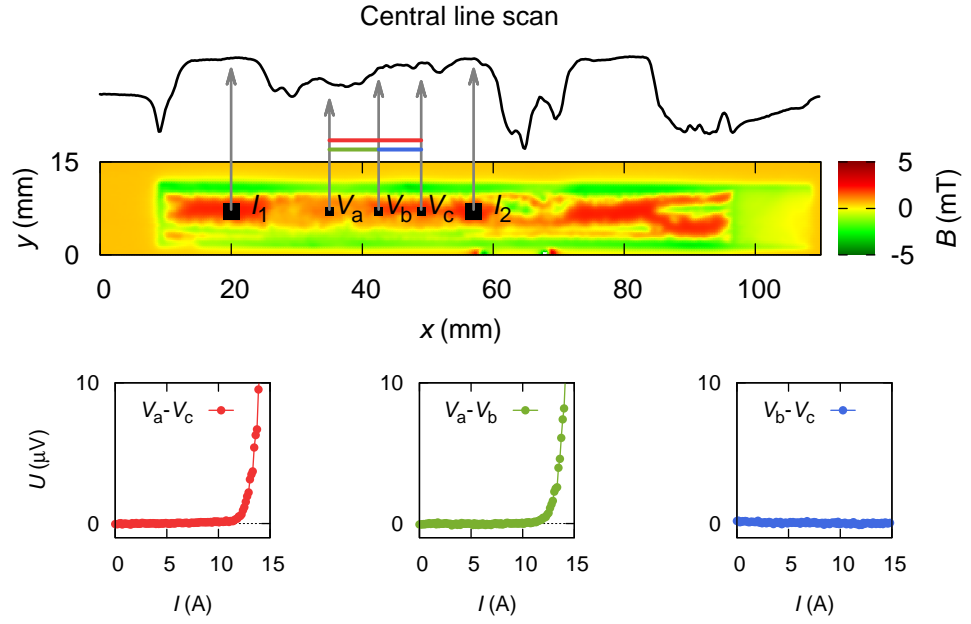


Figure 6.3. Comparison between magnetoscan and transport measurements. The central line scan is sufficient to identify the cross-section limiting the end-to-end performance: the voltage drops in the region, where the central line scan is low.

long conductors, and an implementation into reel-to-reel production systems for quality control is feasible.

6.2.2. Cryoscan

The cryoscan is a commercially available test equipment for superconducting thin films manufactured by THEVA. Its measurement principle similar to [34] and consists of a small coil placed on top of the conductor, which excites currents in the superconducting layer underneath by applying an alternating magnetic field; the time dependent response is detected in the same coil by employing a lock-in technique. During a measurement the amplitude of the field is continuously increased until the occurrence of third harmonics indicates that currents have penetrated the entire thickness of the tape at the actual position. After calibrating against a reference sample a critical current map can be obtained by scanning the sample.

The measurement time is of the order of a few seconds, which is considerably longer compared to the magnetoscan, and results in a relative coarse scanning mesh. The advantage of the technique is the direct assessment of the critical current density, whereas rather complex mathematical modelling is necessary [32] to obtain

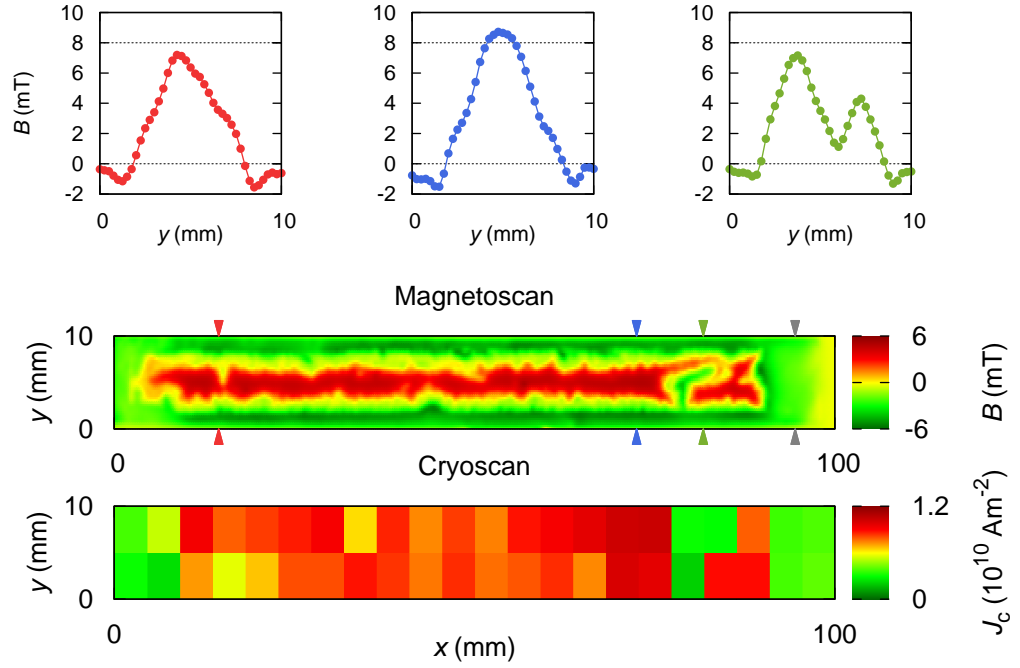


Figure 6.4. Comparison between magnetoscan and cryoscan. Some prominent features, such as a region with comparatively high critical current (blue arrows) or an L-shaped defect extending over the full width of the tape (green arrows), as well as the uncoated end of the tape (grey arrows) are detected by both methods. The magnetoscan provides detailed information the cryoscan is not able to represent due to the coarse scanning mesh of the instrument. The cross-sectional profile (the substrate signal is subtracted), reveals a decreased J_c (red arrows) and two separated current paths (green arrows).

the critical current distribution, which generates the field pattern recorded by the magnetoscan. For a mapping of the sample's overall homogeneity or for the detection of defects forming bottlenecks and thus limiting the end-to-end critical current, a calculation is not necessary, because the defect state of the conductor is evident in the magnetoscan signal.

A comparative measurement on a PVD coated conductor grown by Nexans is depicted in Fig. 6.4. (The cryoscan measurement was a pre-characterisation carried out at the company and supplied with the sample.) Features extending over several millimetres, such as an L-shaped defect or an uncoated region at the end of the tape, are clearly identified by both methods. An area with high critical current density in the cryoscan is revealed by the increased magnetic field in the magnetoscan. However, considerable deviations between both measurements are found in the left half of the tape. This might result from the coarse scanning mesh of the cryoscan, which assigns the critical current sampled at the central

position to the entire pixel. If the tape is not sufficiently uniform, i.e., the length scale of the variation is below the step width, the cryoscan measurement is less representative. This is, for example, the case close to the sample edge, where a corrugated field profile is revealed by the magnetoscan.

Even more information can be obtained from the cross-sectional magnetoscan data using the simple interpretation scheme presented in section 6.1. Figure 6.4 displays such profiles after subtraction of the substrate's ferromagnetic signal taken from the uncoated area at the end. A pronounced defect (red arrows) appears to constrict the current flow and the contour lines suggest two defects close to the edges, which reduce the cross-section. The appearances are, however, deceptive, which is evident after a comparison to the best area of the tape (blue arrows). The demagnetisation peaks are located at the same position, which demonstrates that current flows across the entire width of the tape and a reduced J_c is hence the most likely cause for the low signal.

The strong dip in the profile of the L-shaped defect, on the other hand, results most likely from two overlapping peaks. An interpretation in terms of two current distributions separated by a highly defective or even insulating area is plausible. All this information is not contained in the cryoscan data.

Chapter 7.

Inversion of Hall maps

In transport and magnetisation measurements the average J_c of a sample is directly related to the measured quantity and the application of simple procedures (see chapter 5) is sufficient to extract the desired information from the data. This is different in flux density maps, where the spatially recorded magnetic field $B(x, y)$ depends in a more complex manner on the currents in the sample. According to the Biot-Savart law currents from all over the sample add up to the magnetic induction at a certain position, while the currents flowing right underneath the Hall probe are not detected due to the sensor geometry as discussed in section 4.4.

Thus, there is no direct relation between $B(x, y)$ and $J(x, y)$ and a more elaborated scheme, which is discussed in detail below, is necessary to resolve the local critical current density $J(x, y)$ in the sample.

7.1. Numerics

Figure 7.1a depicts the coordinate system used in the following: the top sample surface lies in the x, y -plane and is perpendicular to $B = \vec{B} \cdot \vec{e}_z$ scanned at a constant scanning height d , which is the distance between the top sample surface and the active area of the Hall probe (gap), using $n_x \times n_y$ equidistant steps of width s . Due to the small thickness c of the film the currents flowing in the sample are modelled by a planar z -independent current density distribution $J(x, y)$.

7.1.1. Analytical formulation

The magnetostatic Maxwell equations ($\vec{\nabla} \cdot \vec{B} = 0$ and Ampere's law $\vec{\nabla} \times \vec{B} = \mu_0 \vec{J}$) are treated by splitting the magnetic induction B into a sum of two fields

$$\vec{B} = \mu_0(\vec{\Omega} + \vec{M}), \quad (7.1)$$

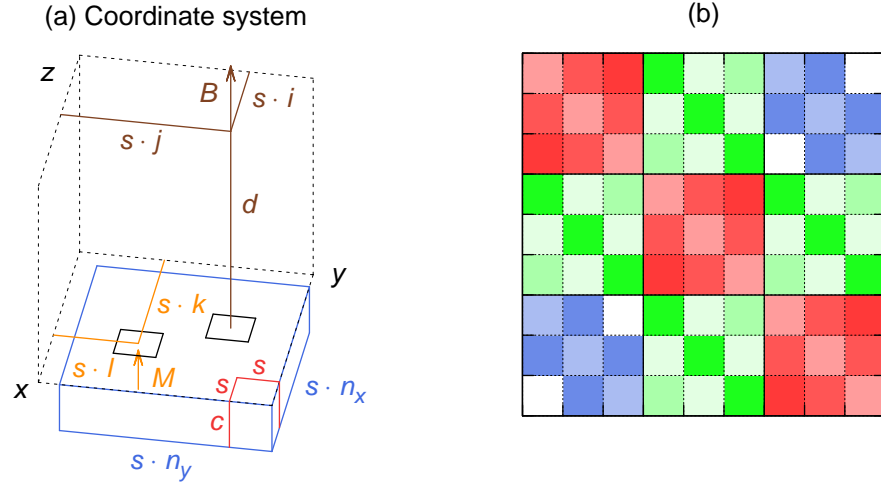


Figure 7.1. (a) Coordinate system employed in the derivation. (b) The matrix reflects the symmetry of the problem and consists of Toeplitz blocks; the individual block constitutes again a Toeplitz matrix. Only the block superstructure indicated by colours is exploited in the inversion.

where \vec{M} is chosen to satisfy the differential equation

$$\vec{\nabla} \times \vec{M} = \vec{J} \quad (7.2)$$

in the entire space. Equation 7.2 implicitly satisfies current conservation $\vec{\nabla} \cdot \vec{J} = 0$, but defines \vec{M} only apart from a gradient field and an arbitrary constant, which are both chosen to be zero. As a consequence, \vec{M} vanishes outside the sample and can be interpreted as a magnetisation, which is confined to the sample volume and establishes the current density \vec{J} by spatial variations. Due to the definition (7.2) Ampere's law can be rewritten as a homogeneous equation for the field $\vec{\Omega}$

$$\vec{\nabla} \times \vec{\Omega} = \vec{J} - \vec{\nabla} \times \vec{M} = 0, \quad (7.3)$$

which can thus be derived from a scalar potential

$$-\vec{\nabla}\Phi = \vec{\Omega}. \quad (7.4)$$

The divergence of the above expression reads

$$\vec{\nabla}^2 \Phi = \vec{\nabla} \cdot \vec{M} \quad (7.5)$$

after substitution of the second Maxwell equation ($\vec{\nabla} \cdot \vec{B} = \vec{\nabla} \cdot (\vec{\Omega} + \vec{M}) = 0$) and the problem can be solved by the method of Green's functions

$$\Phi(\vec{r}) = -\frac{1}{4\pi} \int dV' \frac{\vec{\nabla}' \cdot \vec{M}(\vec{r}')}{|\vec{r} - \vec{r}'|} + \frac{1}{4\pi} \oint d\vec{f}' \cdot \frac{\vec{M}(\vec{r}')}{|\vec{r} - \vec{r}'|}. \quad (7.6)$$

If the planar z -independent current flow is represented by $\vec{M} = M(x, y) \vec{e}_z$ the first term vanishes, because $\vec{\nabla} \cdot \vec{M} = \partial_z M_z = 0$ holds in the entire sample volume. Further, only the surfaces perpendicular to \vec{M} contribute to the second term and (7.6) simplifies to

$$B(\vec{r}) = \mu_0 M(\vec{r}) + \underbrace{\frac{\mu_0}{4\pi} \iint dx' dy' \frac{M(x', y') \Delta z}{(\Delta x^2 + \Delta y^2 + \Delta z^2)^{3/2}}}_{\mu_0 \Omega(\vec{r})} \Big|_{d+c}^d, \quad (7.7)$$

which expresses the measured quantity B solely in terms of the magnetisation M . Here $\Delta x = x - x'$, $\Delta y = y - y'$, $\Delta z = z - z'$. The notation for evaluating antiderivatives is used to indicate the positive contribution from the top ($z' = d$) and the negative from the bottom ($z' = d + c$) surface.

The corresponding set of linear equations for the discrete data $B_{i,j}$ is formulated by approximating the sample as an array of cubes with constant magnetisation.¹ Summing over all elements results in the two-dimensional matrix equation

$$\mu_0 M_{i,j} + \sum_{k=1}^{n_x} \sum_{l=1}^{n_y} K_{i,j,k,l} M_{k,l} = \mu_0 (M_{i,j} + \Omega_{i,j}) = B_{i,j}. \quad (7.8)$$

Here, the matrix entries $K_{i,j,k,l}$ are calculated by evaluating the antiderivative

$$\begin{aligned} F(\Delta x, \Delta y, \Delta z) &= \frac{\mu_0}{4\pi} \iint dx dy \frac{\Delta z}{(\Delta x^2 + \Delta y^2 + \Delta z^2)^{3/2}} \\ &= \frac{\mu_0}{4\pi} \tan^{-1} \left[\frac{\Delta x \Delta y}{\Delta z (\Delta x^2 + \Delta y^2 + \Delta z^2)^{1/2}} \right] \end{aligned} \quad (7.9)$$

at the eight corners of the cubes

$$K_{i,j,k,l} = F(\Delta x, \Delta y, \Delta z) \Big|_{s(i-k-\frac{1}{2})}^{s(i-k+\frac{1}{2})} \Big|_{s(j-l-\frac{1}{2})}^{s(j-l+\frac{1}{2})} \Big|_{d+c}^d. \quad (7.10)$$

After solving (7.8), the current density can be calculated by employing a discretisation of (7.2). The induction B at any location, in particular at the position of the currents in the centre of the sample ($d = -c/2$), can be obtained from (7.8). In

¹ This approach is equivalent to an ensemble of cubic permanent magnets of strength $M_{i,j}$ constituting the magnetisation profile.

order to compare the scans to magnetisation measurements, the magnetic moment m can be evaluated by summing

$$m = s^2 c \sum_{i=1}^{n_x} \sum_{j=1}^{n_y} M_{i,j} \quad (7.11)$$

over the entire sample. This procedure is less sensitive to errors compared to the actual current distribution, which is calculated using a numerical derivative.

7.1.2. Numerical solution

Note that Ω vanishes for the case of an infinitely long slab (zero demagnetisation) as $\Delta z \rightarrow \infty$ in (7.7). In this case the induction is simply determined by the magnitude of M at a certain position and $B = \mu_0 M$ inside and $B = 0$ outside, because $M = 0$ there. However, for finite geometries the contribution from Ω in (7.7) renders the relation between B and M non-local and the equation system must be solved in order to attain the magnetisation.

Equation 7.8 can be mapped one-to-one to one dimension for example by substituting $i' = i + j(n_x - 1)$, $k' = k + l(n_y - 1)$. Outside the sample, where the magnetic field is assessed and $M_{i,j}$ is zero, the equation reads

$$\sum_{k'=1}^{n_x n_y} K'_{i',k'} M_{k'} = B_{i'}. \quad (7.12)$$

The linear system is defined by (7.9) and (7.10) and can be tackled by matrix inversion algorithms.

The nature of the problem is the translation invariance of the Biot-Savart law ($K_{i,j,k,l} = K_{|i-k|,0,|j-l|,0}$), which is reflected by the symmetry of the problem. The matrix is in fact a Toeplitz block Toeplitz matrix, i.e., a number of blocks with Toeplitz symmetry constitute a Toeplitz matrix (see Fig. 7.1b), as pointed out in [35]. In this work the structure of the system is, however, only exploited for efficient storage and the method of conjugated gradients combined with a fast Fourier transform (FFT) is implemented in the algorithm. Although the procedure is fast, the suggestive use of an FFT [35, 36] implies the unnecessary assumption of periodicity in B outside the measurement area, which may create artefacts, if currents are flowing close to the edge of the scanning area.

Matrices with Toeplitz block structure are familiar in a number of fields, such as image reconstruction or system identification. An efficient library for these matrices was developed by the NICONET project [37]. Although the structure

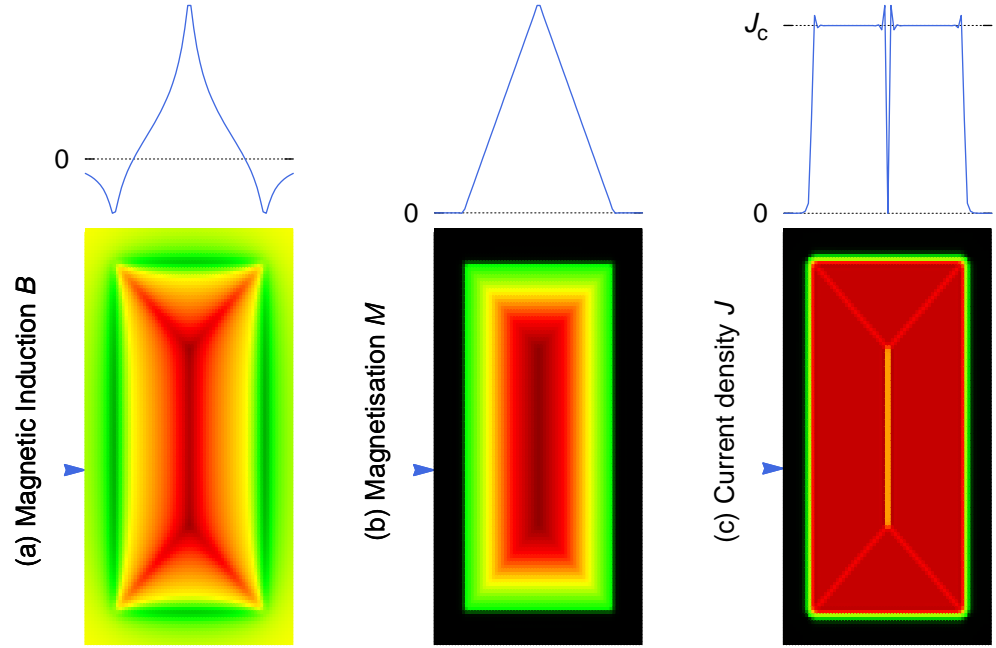


Figure 7.2. Illustration of the inversion procedure. The two-dimensional B profile was calculated for a thin film in the Bean critical state. By solving (7.12) the roof top profile of the magnetisation M is found (see also section 5.1). Computing the current J by deriving M results in a homogeneous constant current distribution. Close to the edges and at the centre, where the current is zero due to symmetry, discretisation errors play a role.

in the individual blocks is ignored by the algorithm² and only the Toeplitz super-structure of the blocks constituting the matrix is exploited [38], the computation time is about ten minutes for a typical 200×200 system on a desktop PC. Although this is presumably longer than FFT based algorithms, it is faster than the actual measurement, in other words fast enough, and allows to solve the system directly without any additional assumptions.

Calculating the numerical derivative is straightforward and a formula was chosen, which calculates the current in the centre of a pixel using the four corners (nearest neighbours) and linear interpolation

$$\vec{J}_{i,j} = \frac{1}{4s} \begin{pmatrix} M_{i,j+1} + M_{i+1,j+1} - M_{i,j} + M_{i+1,j} \\ M_{i,j} + M_{i,j+1} - M_{i+1,j} + M_{i+1,j+1} \end{pmatrix}. \quad (7.13)$$

The magnetic induction was evaluated in the centre plane inside the conductor by employing (7.8) and averaging over the values at the four corners, which introduces moderate smoothing in B .

7.1.3. Condition number

A numerical treatment of a problem is not complete without an assessment of the error propagation. Although the residuum of the solution is of the order of the machine error, i.e., a magnetisation M is found by the algorithm, which creates an induction B numerically equivalent to the measured data, it does not necessarily mean that the solution is correct.

This problem is illustrated in Fig. 7.3: At a large scanning gap or, equivalently, at a small step width, the summation of the single contributions averages the profile because nearby positions have almost identical weight in the summation due to the Biot-Savart law. The process will thus act as a low-pass filter, remove the noise in M and create a smooth B approximating a coarser discretisation with average values. But this has important consequences for the current calculation: taking the derivative of M increases higher frequencies [39] and thus enhances the noise. If, for instance, fluctuations locally destroy the monotony in M , currents will flow even in the reverse direction.

² According to the on-line manual [37] Householder transformations, modified hyperbolic rotations and block Gaussian eliminations in the Schur algorithm are used to solve the linear equation. All matrices were found to meet the prerequisite of being symmetric and numerically positive definite.

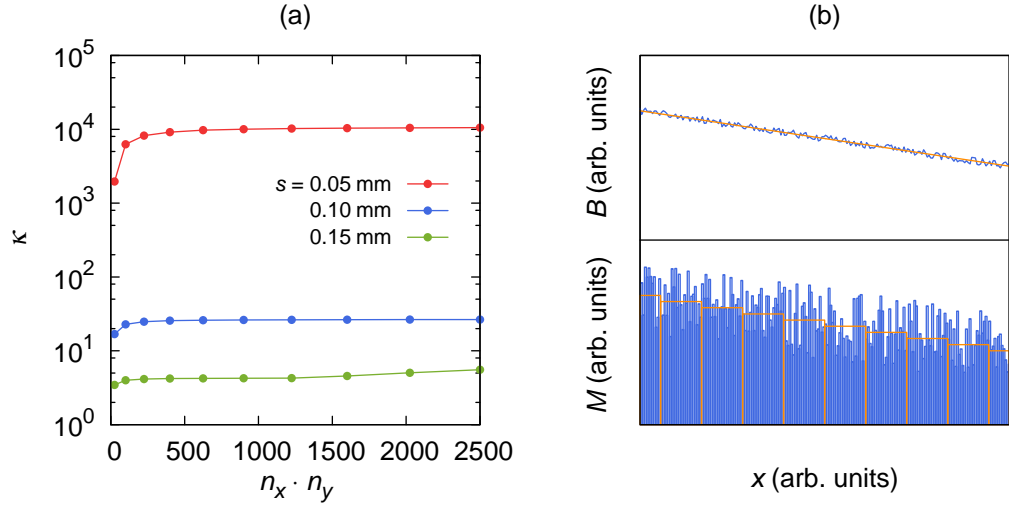


Figure 7.3. Condition number and illustration of the condition problem (a) The condition number κ (here for a $1\text{ }\mu\text{m}$ thin film and a gap $d = 0.15\text{ mm}$) was estimated for increasingly larger system (the convergence is evident). The system is tolerably well conditioned, if the stepwidth s is equal to the gap d . (b) This is because if the discretisation is too fine, averaging effects will smooth the induction B despite the noise in M . The associated current distributions, which are proportional to the derivative of M , will, however, differ vastly: the coarse distribution is equivalent to a constant current distribution and the noise creates large current fluctuations; if the monotony is destroyed, the currents will even change sign.

The above discussion contains the fact that the spatial resolution of an object is related to the distance to the object; the limit depends on the nature of the problem. The equivalent mathematical formulation is the amplification of errors in a matrix inversion: a relative measurement error ϵ_B in the right-hand side of (7.12) introduces an unknown, *larger* error in the calculated magnetisation density ϵ_M . The maximum amplification can be estimated, e.g., in Euclidean norm by the condition number κ of the system

$$\|\epsilon_M\|_2 \leq \kappa(K') \cdot \|\epsilon_B\|_2. \quad (7.14)$$

Special attention has to be paid to the choice of the scanning parameters, if one attempts to calculate the currents. In particular, the step width s and the gap d are crucial, because they define the perspective the discrete elements are viewed at. For not too large matrices, κ can be approximated by the condition numbers estimator implemented in the `Scilab` numerical computation software. As a rule of thumb one aims at a condition number κ such that

$$\|\epsilon_M\|_2 < 1 \quad (7.15)$$

holds. Generally, it was found that the matrix inversion is reasonably well conditioned ($\kappa \approx 10$) as long as the step width is larger than the scanning gap and satisfactory condition can be thus reached by adapting s , but noise and coarseness of the mesh have to be counterbalanced.

Calculating the current density involves computing a numerical derivative, which implies that the relative error in $\vec{J}(x, y)$ will be high, if the change in $M(x, y)$ (the current at this position) vanishes, as for example outside of the sample or in defects. This is, however, a peculiarity of measuring the relative error of a quantity close to zero. Note that (7.14) also bounds the absolute error in M and hence also limits the absolute error in $\vec{J}(x, y)$, which is expected to be acceptably low inside the sample where M does not vanish, as long as (7.15) holds.

7.2. Application to bulks

Bulk superconductors represent a good test system for the inversion, because the samples are large and robust, allowing to cut pieces from any position for a comparison with magnetisation measurements. It was demonstrated in [40] that the condition number is notoriously high for samples with centimetre height and a reduction of the thickness becomes mandatory. Therefore, a YBCO bulk

superconductor was cut near the upper surface using a diamond saw. A disk with a diameter of 26.5 mm and thickness of 0.55 mm was achieved by a final grinding stage. The actual choice of $s = 0.2$ mm is adequate to resolve the spatial variations of the critical current on a sub-mm scale and the system is reasonably well conditioned, $\kappa \approx 9$. Combined with a rough estimate of the relative measurement error $\|\epsilon_B\|_2 \approx 0.01$ this results in $\|\epsilon_M\|_2 \approx 0.09$ satisfying (7.15) and allows to apply the inversion [41].

7.2.1. A test case

An interesting test case for the inversion procedure was unintentionally created during the course of initial alignment checks. In the first few measurements insufficient time was allocated for cooling of the sensor head and the metal housing was still warm when it was brought in contact with the top sample surface. This heated the bulk underneath the probe to presumably above T_c and resulted in the peculiar flux density profile depicted in Fig. 7.4a, showing a shallow minimum in the centre of the bulk instead of the cone shape, which is usually observed. Initially it was assumed that this was due to incomplete flux penetration, although this is admittedly unphysical because the applied field of 1.4 T exceeded the maximum trapped field by nearly a factor of ten, which is more than sufficient to establish the critical state in the entire sample under zero field cooled (zfc) activation. Nevertheless a field cooled magnetisation in the same field was performed, but the overall picture remained the same.

The application of the inversion elucidates the nature of this peculiarity. It shows (cf. Fig. 7.4b) that no currents flow in the centre of the disk. The central area was found to have the same circular shape and diameter (14 mm) as the Hall probe's housing, suggesting local heating by the sensor head. The measurements presented below were started after sufficient cooling time and showed the well-known cone-like flux density profile. This is in fair agreement with the interpretation that the metal housing of the Hall probe heated the disk (presumably to above T_c) and expelled the flux from the region underneath the probe. It demonstrates that the current calculation is a useful tool for the resolution of the local critical current and for the understanding of flux density maps.

7.2.2. Correlation between the critical current and the magnetic field

Scanning the disk twice on the bottom and on the top surface is a good test of the vital prerequisite that the critical current does not vary too much over the sample

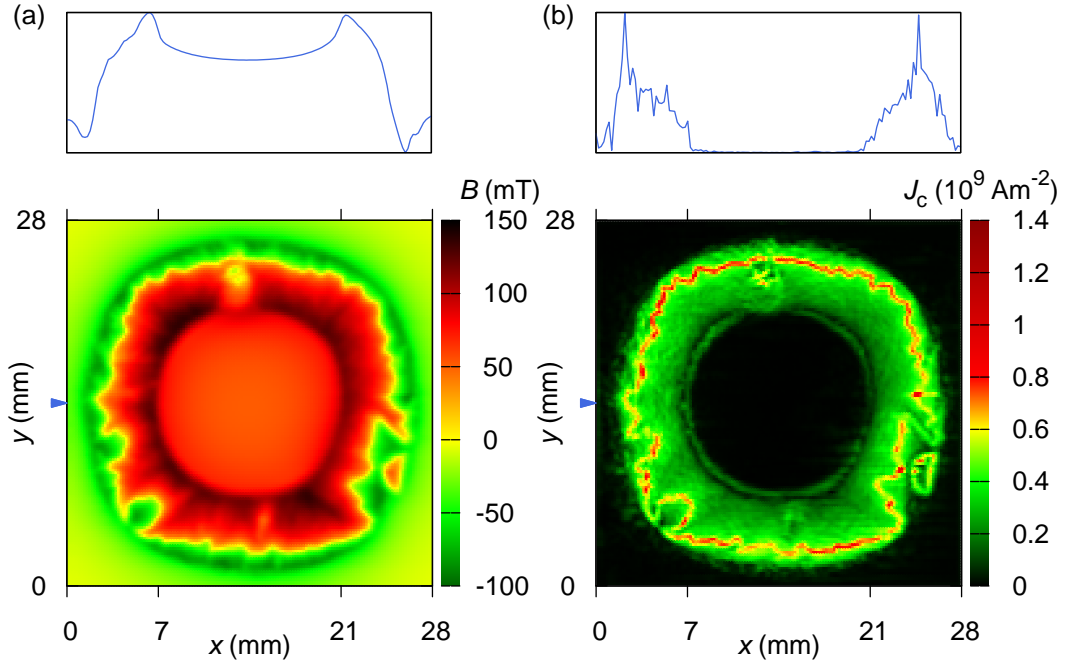


Figure 7.4. Flux profile and current density of a bulk heated in the centre. The top surface of the disk was touched with the warm metal housing of the Hall probe, thereby heating the central region. (a) The Hall scan shows that flux was expelled from the heated area, evident in the cross-sectional profile of B (blue curve), which reaches its maximum close to the edge and decreases towards the centre. (b) The inversion of the flux density map reveals that no currents flow in an circular area of about the housing's diameter.

thickness. Indeed, the recorded magnetic field patterns were alike in all details and the maxima of the trapped field were equal within one percent (252 mT). Moreover, the high reproducibility between a number of measurements shows that the gap remains constant during several runs and was estimated to be roughly 0.15 mm.

At a first glance (see Fig. 7.5) the inversion reveals the most prominent defects as areas carrying very low critical current. A further remarkable result is the detection of the central c -growth sector, which is known to have weaker pinning at low fields and is correctly displayed as a rectangular region with low critical current density.

But a closer inspection of the current and flux density maps shows that the highest currents (exceeding 10^9 Am^{-2}) are located close to the edge of the disk, at those positions, where the magnetic field changes sign and is thus close to zero. This is exactly what would be expected from a field dependent critical current and indeed the local J_c is closely correlated to the magnitude of the magnetic field at a

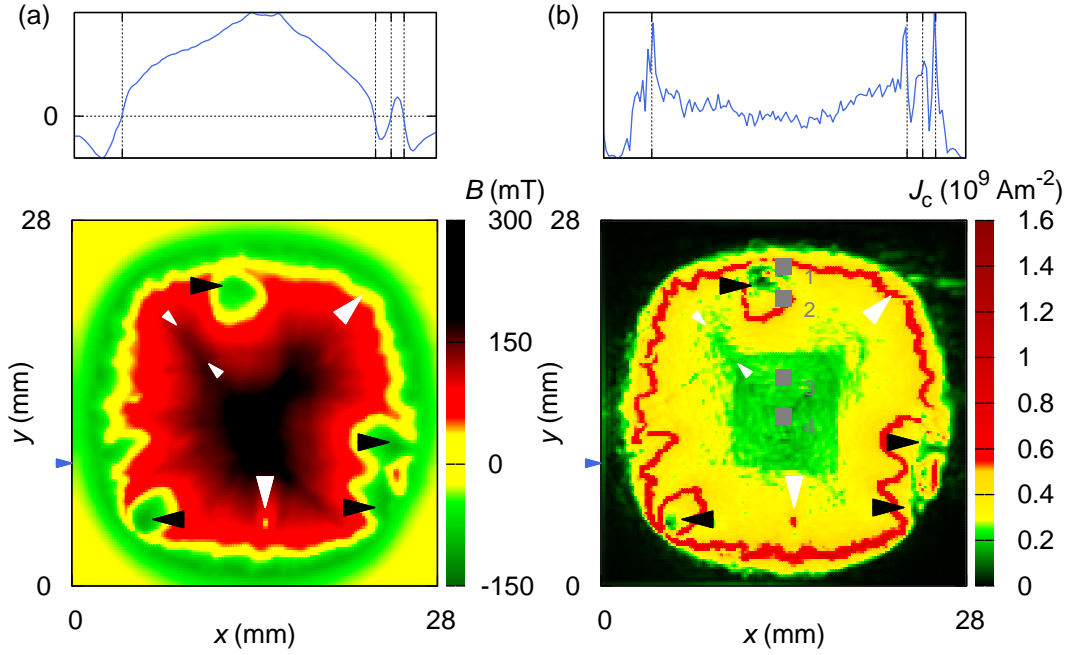


Figure 7.5. Correlation between J_c and B in bulk superconductors. The highest critical current densities are located, where the magnetic induction B is close to zero (large white arrows). This is clearly evident in cross-sectional profiles at the position of the blue arrows as depicted in the top panels. Also inside the disk, for example at the growth sector boundary (indicated by the small white arrows) a clear $J_c(B)$ relation is detected by the inversion. Large defects, where J_c is drastically reduced, are indicated by black arrows. The visualisation of the c -axis growth sector, which is known to have weaker pinning, is another confirmation of the technique. (The grey boxes mark cubes cut for magnetometry.)

certain position. Also inside the bulk a small spot with comparatively low field is (reproducibly) detected: it clearly exceeds the surrounding area in critical current.

Even inside the disk field and current are correlated (eminent for example close to a growth sector boundary) and an overall $J_c(B)$ curve can be plotted (see Fig. 7.6a). Although there is some scatter in the data, which results from both the numerical uncertainty and the inhomogeneity of the bulk material, it suggests a comparison to magnetisation measurements for validating the above results. Here it is important to consider the time scales, i.e., the magnetic moment of a more relaxed state, similar to the bulk in the scans, should be assessed; SQUID magnetisation measurements are therefore particularly well suited.

For this purpose four cubes were cut out of the bulks (cf. Fig. 7.5b) and measured at the temperature of the liquid nitrogen bath. The critical currents calculated by the standard method showed, in agreement with the scans, a relatively large sample

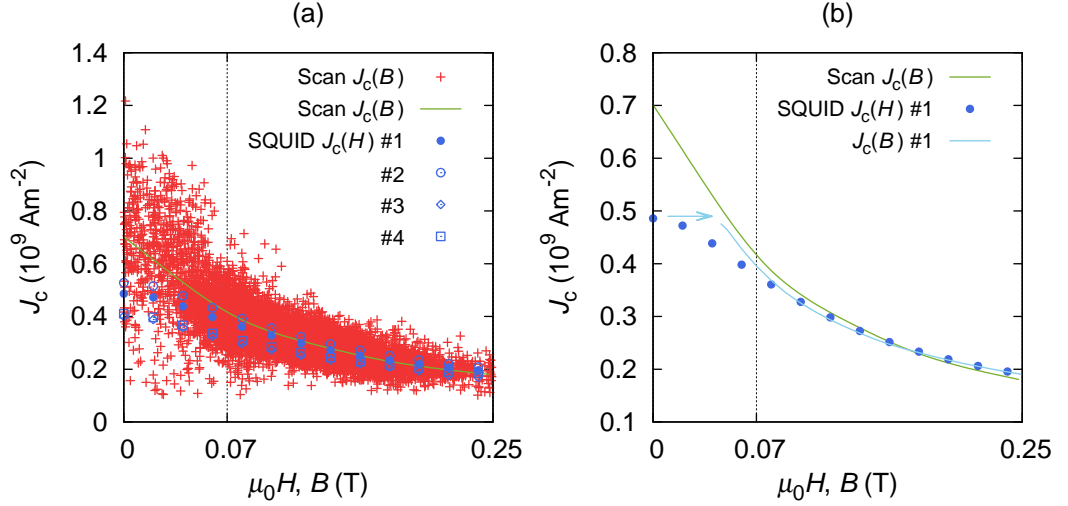


Figure 7.6. Comparison to magnetometry. Although there is scatter in the $J_c(B)$ data taken from the inversion of the Hall scan, good agreement between the mean value and magnetisation $J_c(H)$ measurements is found at higher fields. In the low field region there is a significant deviation, which is related to the self-field of the sample. If it is accounted for, the curves are similar, which is exemplarily depicted for one of the samples cut from the bulk.

to sample variation of J_c , the lowest critical currents being located in the central c -axis growth sector. The SQUID $J_c(H)$ curve confirmed the Hall scan $J_c(B)$ data at high fields; for lower fields the SQUID $J_c(H)$ started to differ significantly from $J_c(B)$. This effect is attributed to the self-field of the sample. After accounting for this contribution (see Fig. 5.1.1b) good agreement was found between the two measurements in the field range accessible to the SQUID, i.e., above the self-field of the sample. In contrast the current calculation provides the important average field dependence of the critical current down to the lowest fields, which is not accessible to magnetic and transport measurements of the macroscopic average J_c (see chapter 8). There is no indication for a plateau in $J_c(B)$ and the critical current density also depends on the field at the lowest magnetic inductions [41].

7.3. Application to thin films

7.3.1. Detection of defects

Hall maps of superconducting films represent an important pre-characterisation technique and were consequently applied to the majority of the samples investigated in this work. In particular, if a film exceeds the SQUID or VSM sample space,

a small homogeneous area can easily be identified and selected. In this way two rather prominent defects (cf. Fig. 7.7) were, for instance, located in the multilayer PLD sample KT046 deposited on a $1 \times 1 \text{ cm}^2$ STO substrate and a 3 mm wide strip was cut from the homogeneous area in between.

Defects noticeably change the nearby local flux density distribution, but their true size and critical current can be obtained only by the inversion. Figure 7.7 shows the result for the two defects in the above mentioned multilayer: Although they appear to have quite similar dimensions in the Hall scan, the one at the left edge is revealed as a rather small spot with zero J_c , possibly because a small piece splintered away during handling. In comparison, the defect located in the middle of the sample is larger, but still carries significant critical current and was most likely created during sample growth.

Apart from the strength of the current density, which changes at the defect position, the vector-field shows that the currents are directed away from the inhomogeneities (see Fig. 7.7). The equipotential lines of the magnetisation M , which are a beneficial by-product of the calculation, represent the streamlines [42] of J . They come to further assistance in the interpretation of the current flow and illustrate how the currents bend and flow around defects.

7.3.2. Correlation between the critical current and the magnetic field

The currents in the sample amount to a magnetic moment of $1.03 \times 10^{-3} \text{ Am}^2$. Evaluating the corresponding mean critical current density using the Bean model results in $J_c = 3.1 \times 10^{10} \text{ Am}^{-2}$. This value deviates by only about 10 % from the VSM measurement carried out on the part cut from the sample (cf. Tbl. 9.1) despite the uncertainty in temperature of the liquid nitrogen bath, scanning gap and, most importantly, geometry (the sample was only approximately rectangular after cutting).

However, the current density is far from being constant in the film. A closer inspection of Fig. 7.7a,c reveals that the same star-like pattern emerges in the current density and in the flux density and map, because J_c and B are closely correlated in thin films and the local J_c of the c -axis growth sector is absent. Again the highest current densities flow close to the edge of the sample, where demagnetisation reverses the sign of the induction and B is thus low; towards the centre of the sample J_c decreases with increasing B (cf. Fig. 7.7a). The cumulative plot Fig. 7.7b, which shows only positive fields, presents strong evidence for a $J_c(B)$ dependence down to the lowest fields.

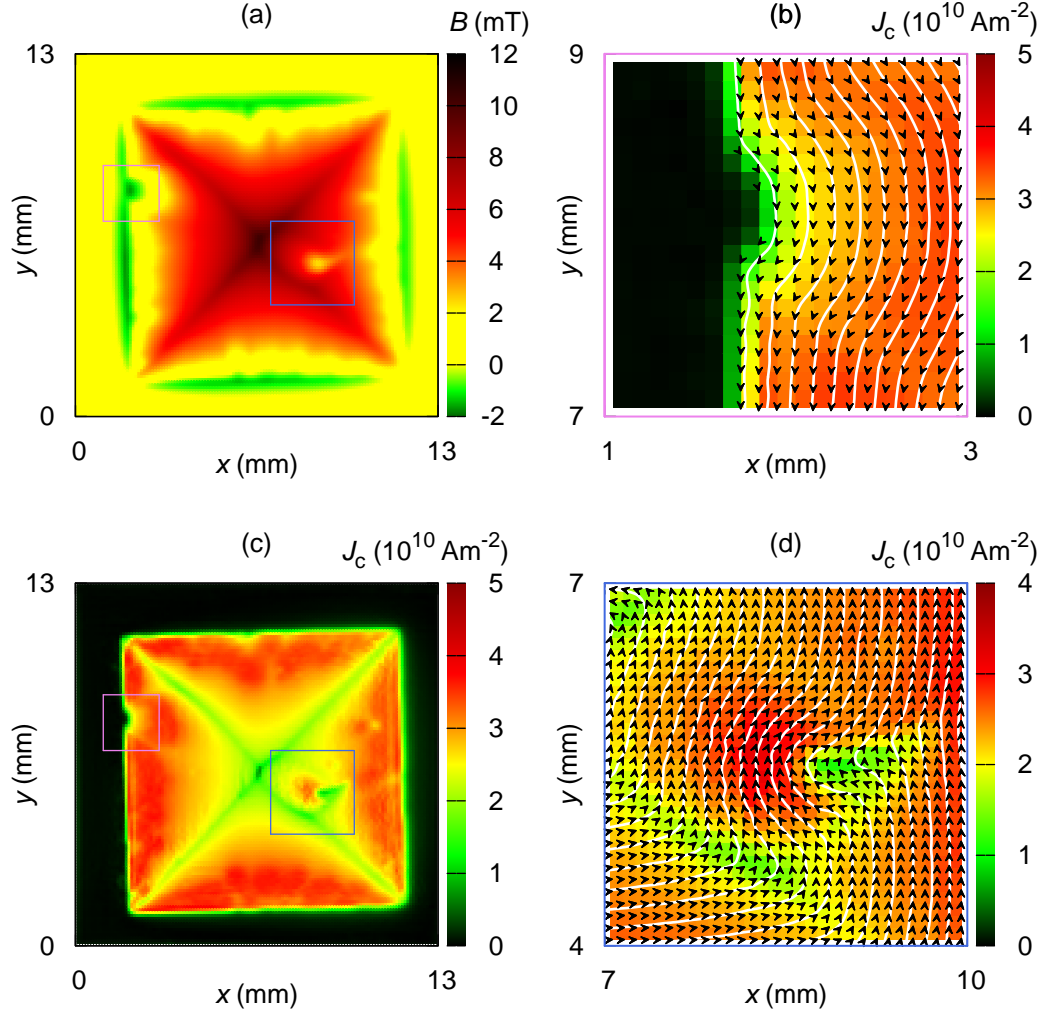


Figure 7.7. Detection of defects and $J_c(B)$ in thin films. Current calculation reveals that the defect at the left edge (magenta square) carries no critical current and is rather small compared to the defect in the middle of the sample (blue square) although they appear to be of similar size in the flux density map. How the inhomogeneities distort the current flow, can be seen in the current vector-field (black arrows) and the streamlines (white). (a,c) The same star-like pattern in the flux density and in the current density map indicates a correlation between J_c and B .

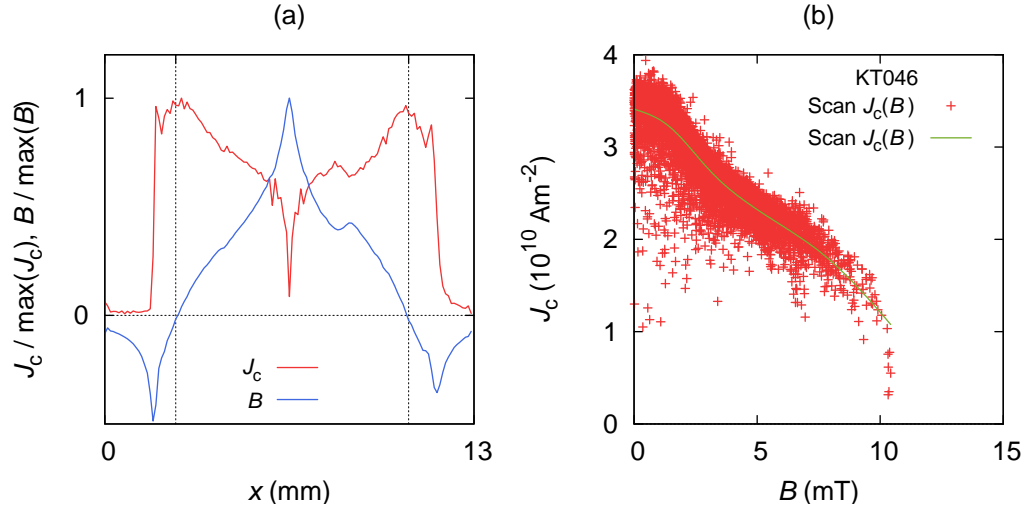


Figure 7.8. Correlation between J_c and B in thin films. (a) Similar to the inversion of bulk superconductors there is a strong local correlation between J_c and B : the maximum current densities are located, where $B \simeq 0$, J_c decreases with increasing B towards the centre. (b) The entire data set $J_c(B > 0)$ shows a clear dependence on the magnetic field.

7.3.3. Comparison to magnetisation measurements

The fair agreement between the magnetic moment derived from the Hall scans and the VSM measurements suggests further comparisons under applied fields. For this purpose a solenoidal coil was designed (see Fig. 7.9), which allows to set background fields of up to 70 mT (several times the typical B^* of thin films) with a standard 3 A current supply. Due to symmetry the magnetic field has only an axial component in the central plane of the solenoid and Hall maps confirmed that the induction was reasonably homogeneous varying by less than 5 % within the measurement area. Although films of up to 1 cm^2 can be contained by the sample holder machined in the coil body, a $5 \times 5 \text{ mm}^2$ sized HLPE sample (FH724) was selected for the experiments, with magnetisation measurements in mind.

A first interesting test was made in the following way: Initially the sample was scanned in the remanent state after applying 70 mT, in order to determine the maximum trapped field, which serves as a good lower estimate for the penetration field B^* and was found to be approximately 8 mT. After heating the sample above T_c , it was subjected to a second zfc magnetisation loop with a maximum field of 8 mT. When shutting down the current in the coil, the field changes by less than $2B^*$ and, as a consequence, oppositely directed currents should circulate in the centre and close to the edge of the sample. This was confirmed by inverting the

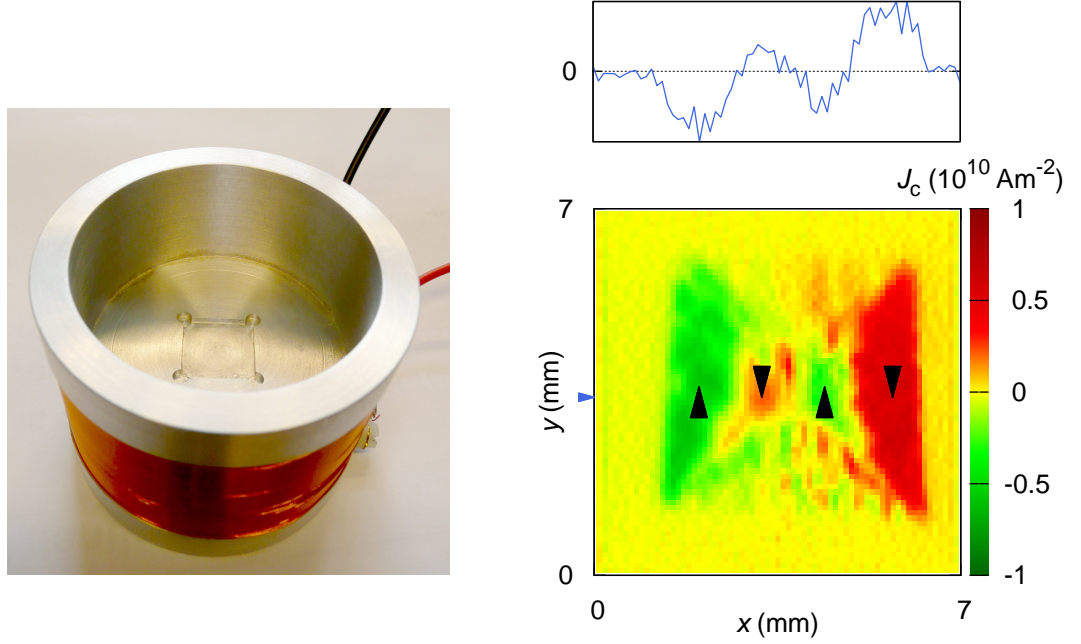


Figure 7.9. (Left) Coil used to magnetise thin films. The machined sample space in the centre contains the film and protects the top surface from scratches. (Right) Partial reversal of flux in a sample. After applying a field approximately equal to the penetration field, shutting down the current in the coil reverses only the outermost currents.

remanent flux density profile (see Fig. 7.9), which clearly shows that, for instance, J_y changes three times its sign in the central cross-sectional profile.

For measurements at applied fields the weakly inhomogeneous background field of the coil must be subtracted, in order to calculate the currents in the sample. Removing the sample requires to evaporate the liquid nitrogen, which is impractical and time consuming. Thus another strategy was employed to eliminate the sample's contribution: By touching the top surface of the film with an Al rod³, the sample is heated above T_c . After removal of the rod the film is field cooled and no flux density gradients are established. Hence the film is invisible to the Hall scan and the background field of the coil can be assessed. Test measurements at zero applied field confirmed that no currents were left after this procedure.

In the following experiments the field was ramped up to 70 mT before setting the background field of the measurement (0, 30 and 50 mT), which subjected the sample to a field change of at least 20 mT. This is more than twice the estimated B^* at zero applied field and thus sufficient to reverse the currents in the entire

³ Initial tests with acrylic glass, which is much softer and minimises the risk of scratching the film, were not successful due to the small thermal conduction coefficient of the material.

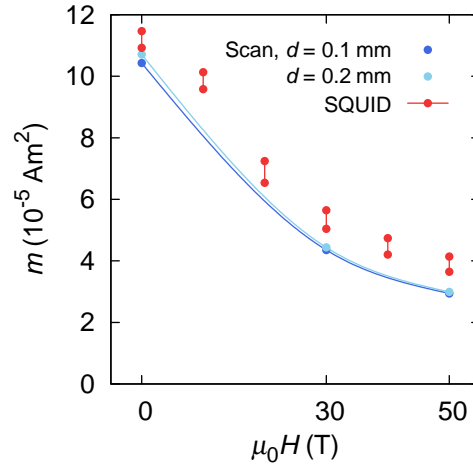


Figure 7.10. Comparison of the magnetic moment assessed by SQUID and Hall scan measurements. Good agreement is found at zero applied field, if relaxation effects are taken into account. (The red points correspond to measurements directly and 20 minutes after the field change, which is approximately the scanning time.) At higher fields both measurements show a similar $m(H)$ dependence, but the Hall scan results in somewhat lower values. The scanning gap d has only a minor influence on the magnetic moment.

sample. After scanning the sample the background field was assessed, subtracted from the data and the magnetic moment was evaluated using the inversion.

Considering the large relaxation time, the SQUID is preferable for in-field measurements and for a comparison with the Hall scan, which ended typically 20 minutes after the activation with the coil. In particular the capability of the SQUID magnet charging system to avoid field overshoots secures measurements on thin films with their small penetration fields.

A comparison between both measurements is shown in Fig. 7.10. The decreasing magnetic moment, which was recorded directly and 20 minutes after sweeping the magnetic field in the SQUID, demonstrates that relaxation processes are relevant. In the remanent state (zero applied field) good agreement between the scan and the more relaxed state is found. At higher fields both methods indicate a strong decrease of J_c (m decreases by more than a factor of 2 at 50 mT). The Hall scan results, independently of the actual choice of the scanning gap, in somewhat lower in-field values. One reason might be that the power supply makes small undershoots when ramping the field down from the maximum to the desired background field, which subjects the sample to a minor hysteresis loop and decreases its moment. Further it must be noted that the temperature of the nitrogen bath is not known

exactly, because the PT100 temperature sensor is inaccurate to almost 1 K at liquid nitrogen temperature. The temperature of the nitrogen bath is presumably above 77.2 K, which could explain the lower critical current density.

Chapter 8.

Simulation of self-field effects

The Bean critical state in thin superconducting films is successfully described in [4, 2] (see chapter 2). However, field independent critical currents have never been observed in high-temperature superconductors at all but the lowest applied fields: Apart from the results of the previous chapter, which strongly indicate a field dependent J_c also at the lowest fields in bulk superconductors as well as thin films of YBCO, a power-law field dependence $J_c(H) \propto H^{-\alpha}$ is commonly observed in YBCO films at fields in the Tesla range and temperatures not too close to T_c (cf. Fig. 8.1). As pointed out earlier in section 5.1.1 the field dependence $J_c(H)$, clearly evident in both magnetisation and transport measurements, does not necessarily contradict the application of the Bean model, which is valid as long as the variation of the magnetic induction B *inside* the sample is negligible.

Two contributions, the homogeneous applied field $\mu_0 H$ created by the currents in the magnet and the self-field B_{sf} generated by the supercurrents flowing in the sample, constitute the magnetic induction. The latter contribution can be estimated to be of the order of the characteristic field of a thin film

$$B_f = \mu_0 c J_c / \pi \quad (8.1)$$

introduced in chapter 2 and two different regimes can thus be distinguished: At high applied fields ($\mu_0 H \gg B_f$) the self-field of the sample can safely be ignored and the Bean critical state model can be employed to determine the material law $J_c(B)$ by measuring the critical current density as a function of the applied field because $J_c(B) \simeq J_c(H)$. If, on the other hand, the applied field is comparable to the self-field ($\mu_0 H \approx B_f$), which is typically in the mT range for the samples investigated here, the self-field cannot be neglected, the Bean critical state model is inapplicable and the material law $J_c(B)$ cannot be assessed by a measurement of $J_c(H)$.

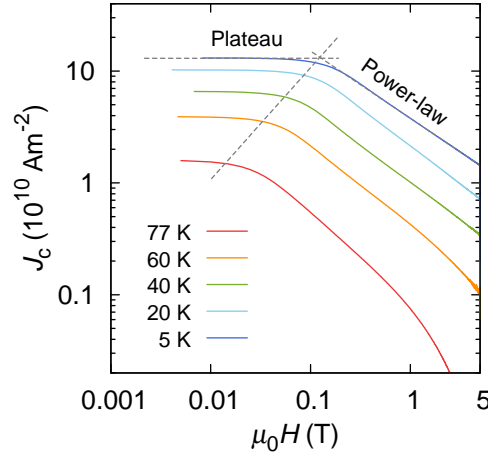


Figure 8.1. Low field plateau and power-law field dependence of $J_c(H)$ determined by magnetisation measurements. The linear slope on a double logarithmic scale reveals the power-law regime at high fields. At low fields J_c is almost constant, which results in a plateau in $J_c(H)$. The transition between the two regimes is indicated by the grey line and occurs at fields roughly proportional to the critical current density of the plateau.

Figure 8.1 shows typical magnetisation measurements carried out at temperatures ranging from 5 to 77 K and evaluated without accounting for the self-field. Two different regimes can be distinguished at first glance. At high fields a power-law field dependence is observed in all the samples, while J_c saturates and remains approximately constant below a certain field. The transition between the two regimes, the low field plateau and the strong decrease at high fields, is shifted to higher fields at lower temperatures. But also the critical current density at zero applied strongly increases with decreasing temperature, which enhances the self-field of the sample according to (8.1).

This suggests that the low field plateau does not characterise the material, but is an effect of the self-field of the sample, which obscures the identification of $J_c(B)$. (Here, $J_c(B)$ refers to the material law, which describes the physics of flux pinning, while $J_c(H)$ is the critical current density as a function of the external applied field.) In order to gain further insight into this regime a numerical simulation was used to simulate magnetisation and transport measurements.

Initialise current distribution

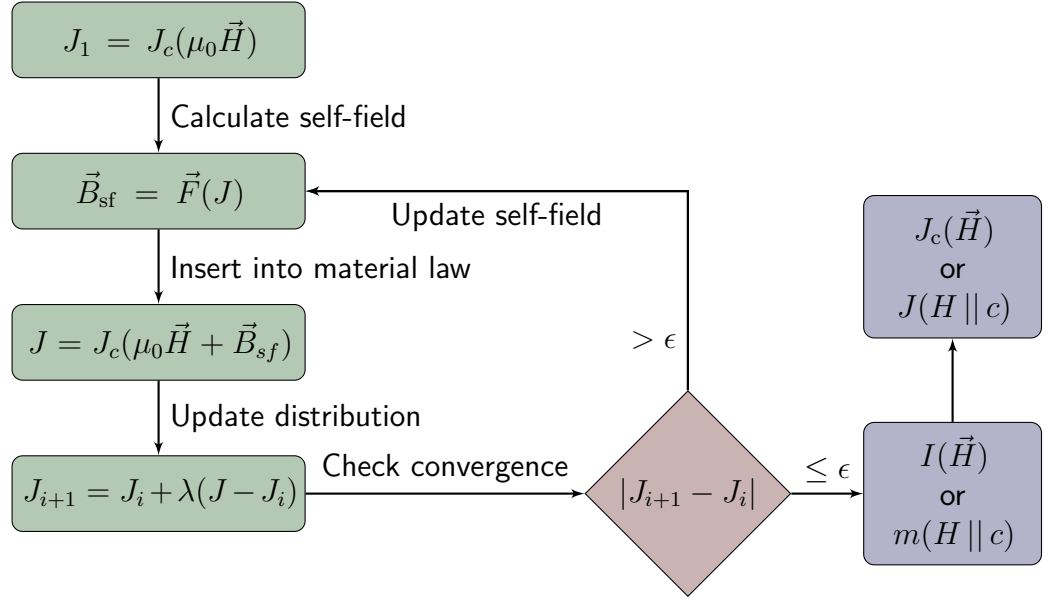


Figure 8.2. Flow chart sketching the iterative procedure employed to calculate the current distribution for an arbitrary material law $J_c(\vec{B})$. Within the iteration, J refers to a current density distribution; the end is a single macroscopic current density.

8.1. Numerics

Two geometries are considered in the iterative procedure employed to calculate the current distribution in the sample for a material law $J_c(\vec{B})$. A thin sheet with rectangular cross-section models the current transport through a coated conductor and a flat disk simulates magnetisation measurements. In the latter case it is assumed that the currents circulate around the centre of the disk. This implies that only fields directed parallel to the symmetry axis can be treated, which is sufficient because SQUID and VSM magnetisation measurements were always carried out with the applied field parallel to the c -axis. No restrictions are imposed on the applied field direction when simulating transport measurements and anisotropy effects can be studied in this geometry.

In both geometries the cross-section is subdivided into an array of rectangular elements. (Due to current conservation only one half of the cross-sectional area must be considered when magnetisation measurements are simulated.) The flow chart in Fig. 8.2 illustrates the iterative procedure. Initially, the self-field is disregarded and a constant current density $J = J_c(\vec{B} = \mu_0 \vec{H})$ is assigned to each of the elements because the applied field is homogeneous. In the next step the self-field \vec{B}_{sf} is

computed at the centre position of the individual rectangles and added to the applied magnetic field. The material law $J = J_c(\vec{B} = \mu_0 \vec{H} + \vec{B}_{sf})$ is evaluated at every position and the position dependent self-field results in a current density distribution. For stability reasons only a small step, typically half the way (cf. the λ -step in Fig. 8.2), is made towards the new distribution at each step. Although this approach consumes more time it damps oscillations, i.e., successive over- and underestimations of the currents, and guarantees a smooth convergence.

When a stable solution is iteratively found, i.e., the last update of the current density is below a certain limit at all positions, the observable quantities $I(\vec{H})$ or $m(H || c)$ are calculated. Generally a relative coarse discretisation, typically less than 1000 elements, is sufficient and the final current and field distribution is obtained within a few seconds on a desktop PC. In order to enable a comparison with experimental data a macroscopic current density is computed, which is in the case of transport measurements identical to the critical current density $J_c(H)$. For a comparison to magnetisation measurements two branches of a hysteresis loops must be simulated, in order to apply the evaluation procedure described in section 5.1.

8.2. Simulation of magnetisation measurements

This section addresses magnetisation measurements in order to introduce some of the basic properties of the magnetic field and current distribution in thin films at low applied fields. More emphasis is laid on a comparison with experimental data in the following section, where transport measurements are treated.

Figure 8.3 shows the results of simulating a $1\text{ }\mu\text{m}$ thick disk with a radius of 2 mm and a monotonically decreasing $J_c(B)$. At zero applied field the circulating currents create a positive maximum of magnetic field at the centre of the disk and a negative field peak is created at the edge of the sample due to demagnetisation. As a consequence, the magnetic induction is zero at a certain position close to the edge of the sample (core). The associated current distribution is not shown, because it is easy to deduce from the field distribution: as J_c is a decreasing function of B , the current reaches its highest value at the core and is minimal at the centre of the disk.

The behaviour in small applied fields can be understood by superposing the self-field distribution at $H = 0$ with the homogeneous applied field. If the applied field is positive, it will compensate the negative fields close to the edge and the position where the applied field cancels the self-field will be shifted further towards

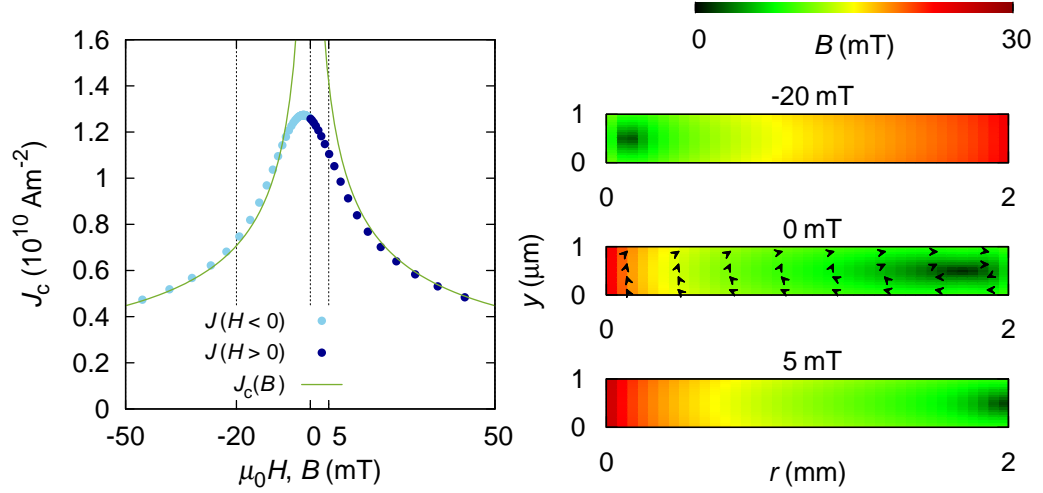


Figure 8.3. Magnetic field distribution in a thin disk at low applied fields. Due to the large demagnetisation a position with zero magnetic induction (core) is found close to the edge of the disk (dark green region). Applied fields smaller than the self-field shift the core either towards the edge or to the centre of the sample and $J(H)$ clearly differs from $J_c(B)$. The critical current peaks at negative applied fields, when the applied field optimally compensates the self-field of the sample.

the edge of the sample. The opposite is true, if a negative field is applied and the core will move to the centre of the sample. It is important to notice that as long as the self-field is comparable to the external field, i.e., as long as there is a core with zero field inside the film, $J(H)$ and $J_c(B)$ clearly differ. (The magnetic moment of two branches of the loop was directly converted into the macroscopic current, in order to allow a direct comparison with the material law.) Both curves start to match, either when positive applied fields shift the core beyond the sample edge, or at negative applied fields, which are sufficiently large to move the core to the centre of the disk, where the associated current distribution has negligible influence on the magnetic moment of the sample.

The macroscopic current of the sample peaks, when the applied field optimally compensates the self-field and a current distribution is established which maximises the magnetic moment of the film. It was found in agreement with [43, 44] that the peak occurs at negative applied fields (see Fig. 8.3). This shows that lowering the inner positive fields is more beneficial than reducing the outer negative fields, which flow only close to the edge, although the outside loops at negative fields have higher weight when calculating the magnetic moment. Experimental data on films grown on single-crystalline substrates generally support this result. Exceptional

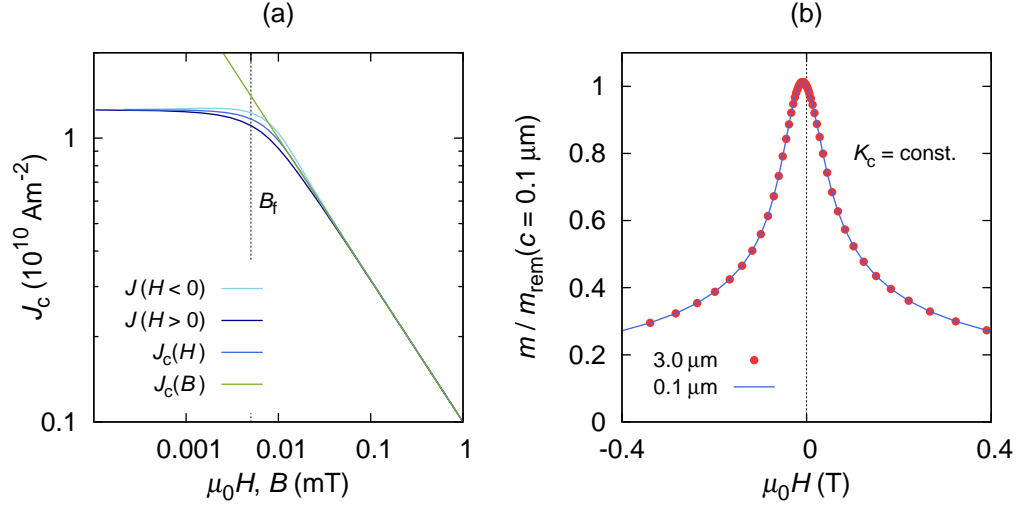


Figure 8.4. Simulated $J_c(H)$ using a power-law $J_c(B)$ and the role of the sheet current K_c in thin disks. (a) The simulations are evaluated similarly to transport measurements, i.e., two branches of a magnetisation loop are used to calculate $J_c(H)$. The critical current density saturates at low applied fields despite the power-law $J_c(B)$, which diverges at zero field, as a material law. (b) The critical current density J_c and the sample thickness c have similar effects on the magnetic properties of thin films, which are a function of the sheet current density.

cases, where the peak is located at positive fields may be due to granularity [45], which could also be present in these films.

Figure 8.4a depicts how two $J(H)$ branches of the loop in Fig. 8.3 are combined to $J_c(H)$ by the standard evaluation of magnetisation measurements. A comparison with experimental data (cf. Fig. 8.1) shows, that all the features of the experimental curve have correctly been reproduced by the simulation: at high applied fields $J_c(H)$ matches $J_c(B)$ and saturates at low fields. Inserting $J_c(H = 0)$ into (8.1) results in $B_f \approx 5$ mT, the field, where the transition between the high and the low field regime occurs. The generation of the plateau at low fields is insofar remarkable as the power-law $J_c(B) \propto B^{0.5}$, which was used in all the calculations presented so far, diverges at zero applied field.¹ As discussed above the flat $J_c(H)$ is a self-field effect and its characteristics is the existence of a core with zero magnetic induction inside the sample.

It is evident that assuming disk geometry to simulate the quadratic or rectangular films investigated in this work is not important for understanding self-field effects. This is because the nature of the results stems from the compensation of the sample's

¹ To avoid numerical problems a maximum current much higher than $J_c(H = 0)$ was introduced but it came into effect only in the very first iteration and thus did not affect the final result.

field by the external applied field, which occurs in all samples independently of the exact geometry below a certain field. Thus, all features can be reproduced by employing this simple geometry.

Another feature of thin films, which is valid also for transport measurements and important for the discussion of the thickness dependence of the critical current $J_c(c)$ in the next section, is depicted in Fig. 8.4b. It shows that $m(H)$ is a function of the sheet current density $K_c = cJ_c$ and that thickness c and critical current density J_c cannot be distinguished by a measurement of the magnetisation curve (a fact already familiar from section 2.2).

8.3. Simulation of transport measurements

The simulation shown in Fig. 8.5 was carried out on a sample with the same cross-section ($1 \times 10 \mu\text{m}^2$) as the bridged HLPE samples discussed in chapter 10, again under the assumption of the typical exponent $\alpha = 0.5$ in a power-law $J_c(B)$. In order to enable a comparison with the above results anisotropy effects were disregarded and the field was always applied $H \parallel c$ (parallel to the shorter dimension). The fact that the aspect ratio is much lower compared to the sample of the previous section, plays no particular role, because self-field effects are not related to the thin film geometry. However, it is shown below that also a sample with an aspect ratio of 10 is thin in the sense that the thickness and not the width is the determining dimension and B_f is still a suitable measure.

At zero applied field the field distribution wraps around the centre of the conductor, which is the position of the core at self-field. The sample conducts a critical current density of $1.3 \times 10^{10} \text{ Am}^{-2}$ in this state, which corresponds to $B_f \approx 5 \text{ mT}$. Figure 8.5 shows that the estimate is in fair agreement with the simulated data: the self-field regime occurs approximately below this field.

Hence, self-field effects are to be expected as long as the external applied field is comparable to B_f . If it is raised to 5 mT the field profile in the conductor shows that the core, initially located at the centre, is shifted towards the edge of the conductor, which would be expected from simply adding the applied field to the self-field profile. Analogous to the simulated magnetisation measurement the sample still conducts approximately the self-field critical current density and $J_c(H)$ remains consequently almost unchanged.

An applied field of 10 mT shifts the core beyond the edge. This causes $J_c(H)$ to decrease rapidly and to follow the material law $J_c(B)$, indicating that the external applied field controls the current distribution in the sample at higher fields.

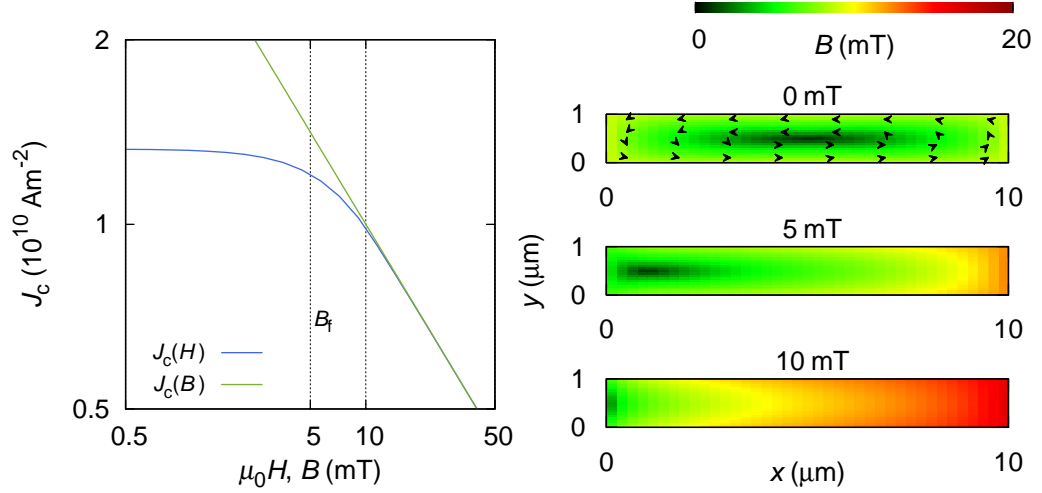


Figure 8.5. Magnetic field distribution in a thin conductor at low applied fields. The self-field of the sample is circular and is thus zero at the centre. Small applied fields shift the core towards the edges of the conductor and the critical current remains approximately constant as long as the core is located inside the tape. Although the aspect ratio of the sample is rather low, the typical field of a thin films B_f properly estimates the transition into the self-field regime.

In essence the same pattern emerges in magnetisation and transport geometry: the characteristic field B_f splits $J_c(H)$ into two domains, a high field decay according to $J_c(B)$ and a plateau at low fields. It must be stressed that $J_c(H = 0)$ remains finite even if a material law $J_c(B)$ is used, which diverges at zero field. This result is unexpected and novel, because earlier work [46, 44, 47, 48] employed variations of the Kim model or an exponential dependence. In these cases a saturation at low fields is thus a self-fulfilling prophecy.

8.3.1. Comparison with experiment

Transport measurements on the patterned HLPE sample FH750 (cf. chapter 10) serve best for a comparison with the experiment, because the bridge's cross-sectional dimensions are accurately known and all the input parameters of the simulation are thus well-defined. The width ($10\ \mu\text{m}$) was determined by optical microscopy and the thickness ($0.72\ \mu\text{m}$) was measured in an FIB system (see section 4.6). Although the latter technique is more sophisticated and requires expensive equipment, the optical measurement is—besides the pure interest in the absolute value of the critical current density—more important, because the self-field regime is controlled by the sheet current density and the thickness thus

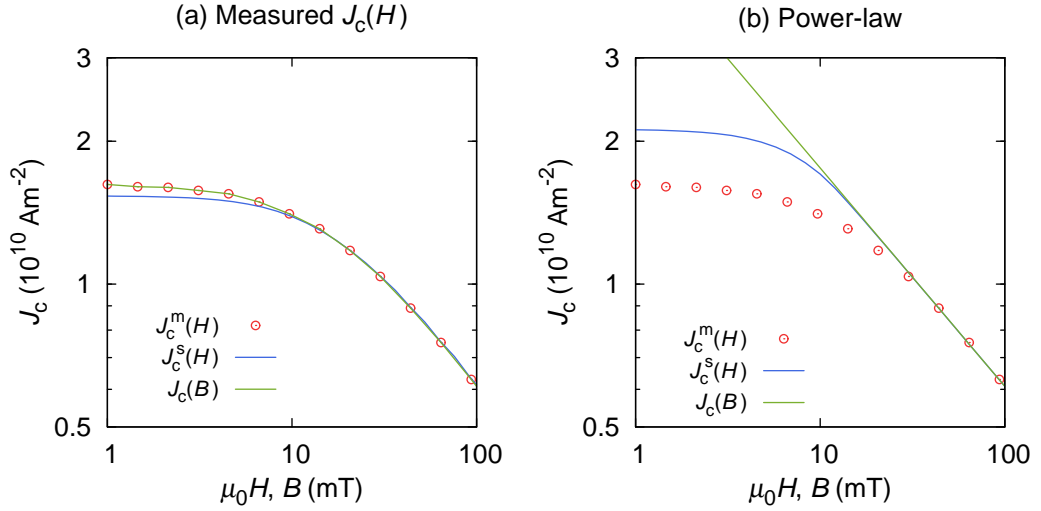


Figure 8.6. Simulations at low applied fields. (a) If $J_c(B)$ is equal to the measured $J_c(H)$, the simulation underestimates the critical current in the self-field regime. The deviation is small but significant, demonstrating that a measurement of $J_c(H)$ does not reveal the low-field $J_c(B)$. (b) Although an extension of the power-law $J_c(B)$ down to the lowest fields results in a finite $J_c(H = 0)$, it fails to reproduce the measurement.

does not play an important role. All the measurements presented in this section were carried out in the 6 T-system; the field was always applied $H \parallel c$.

First, it is necessary to show that a measurement of $J_c(H)$ is not sufficient to determine the $J_c(B)$ behaviour at low fields. Therefore, the material law $J_c(B)$ of the simulation was set equal to the interpolated $J_c(H)$ data of the measurement. (For clarity, m for measurement and s for simulation label the according critical current densities in the graphs of this section.) The computed $J_c(H)$ curve is not consistent with experiment: the current density is underestimated (see Fig. 8.6a) as soon as the low field regime starts, i.e., the power-law dependence ends and the current begins to saturate. Although the difference is small (approximately 5 %), the effect is significant and reproduces, when the discretisation or the geometry are varied. This demonstrates that $J_c(H)$ and $J_c(B)$ are two distinct quantities in the self-field regime.

It was shown above, that the simulated field dependence forms the self-field plateau, even if the power-law $J_c(B)$ is extended down to the lowest fields. The qualitative agreement promotes simulations using $\alpha = 0.46$ identified by a fit to the high field behaviour and a quantitative comparison of simulation and measurement (cf. Fig. 8.6b). But the result is a strong over-estimation of $J_c(H)$ at low fields—the zero field critical current density is too high by about 25 %. Hence, the power-law,

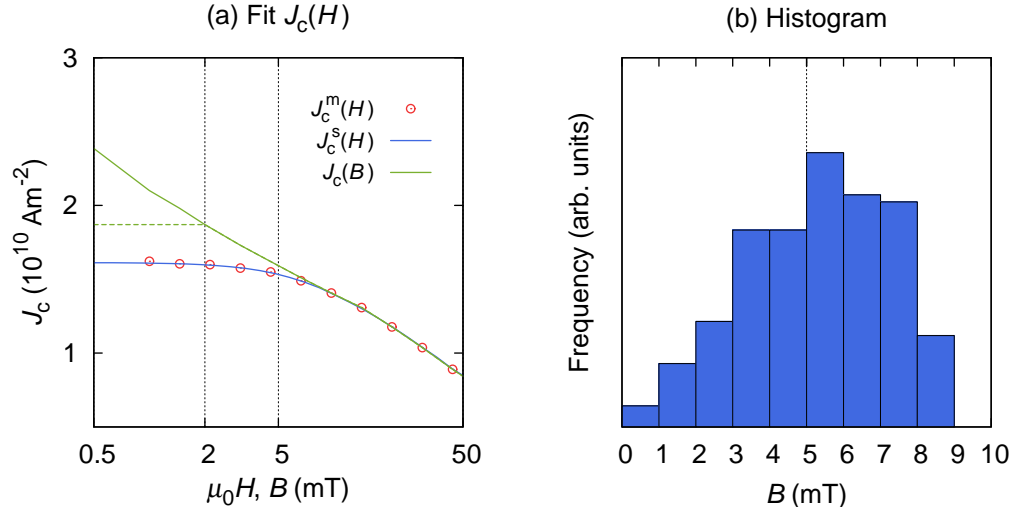


Figure 8.7. Fitting the material law to the measured data. After tailoring $J_c(B)$ the simulation matches the experimental data in the entire field range. The low field $J_c(B)$ is, however, not unambiguously defined: two material laws (solid and dashed green line), which are strongly distinct at low fields produce an identical $J_c(H)$ curve, because the self-field inside the sample has a broad distribution around $B_f = 5$ mT and the currents flowing at the lowest fields have insignificant weight.

although technically applicable in the entire range of applied fields, does not serve as a single material law.

8.3.2. Assessing the critical current density at low fields

Because the self-field critical current density was both under- and overestimated in the above attempts, it should be possible to find a material law, which reproduces $J_c(H)$ in the entire field range. Iterative manipulation of $J_c(B)$ on a discrete set of fields (intermediate points are defined by linear interpolation) is indeed successful (see Fig. 8.7) and the computed $J_c(H)$ matches the experimental data.²

This does, however, not per se mean that the successfully adapted $J_c(B)$ reveals the intrinsic material law. Figure 8.7a shows that there is some degree of freedom in the actual choice of $J_c(B)$ at the lowest fields: The tailored material law can, for instance, be shaped in a way that the slope of $J_c(B)$ increases with decreasing field, showing that a low field plateau in $J_c(H)$ does not necessarily indicate a saturation of $J_c(B)$. If, on the other hand, $J_c(B)$ is held constant for fields smaller than $B_f/2$ (approximately 2 mT for this film) the result is identical.

² Similar attempts to identify the low-field $J_c(B)$ were undertaken for example by [49, 47], who varied the parameters of a refined Kim-model to reproduce the experimental $J_c(H)$.

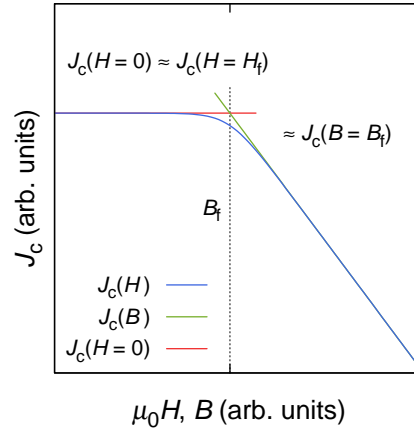


Figure 8.8. Approximations used to derive $J_c(c)$ from $J_c(B)$. At applied fields below B_f the field dependence $J_c(H)$ is constant, at fields above B_f it is equal to $J_c(B)$. On a double logarithmic scale $J_c(H)$ forms a knee—the low field plateau kinks at B_f .

The reason why changes to the low field $J_c(B)$ leave $J_c(H)$ unaffected becomes clear, if the field distribution in the sample is considered (see Fig. 8.7b). At zero applied field the omnipresent self-field ranges from zero to about two times B_f and the frequency of currents flowing in fields below $B_f/2$ is too low to contribute significantly to I_c . The simulation is thus not sensitive to the low field $J_c(B)$ and the low field critical current density, in particular the zero-field $J_c(B) = 0$, cannot be determined in this way and remains inaccessible to a measurement of the transport critical current.

8.3.3. Thickness dependence of the critical current density

The prominent thickness dependence of the critical current density $J_c(c)$ in superconducting thin films and coated conductors is of great importance for understanding flux pinning in this material and has therefore been subject of extensive research. If the defect structure of the film is homogeneous, in particular, if film degradation with thickness and the influence of the substrate interface are negligible, valuable information about the pinning scenario can be obtained by comparing the experimental $J_c(c)$ dependence to theoretical predictions.

But it was recognised in [48] that the self-field of the tape depressed the critical current with growing thickness c , if $J_c(B)$ is not constant. Thus, one cannot a

priori rule out the influence of the self-field on $J_c(c)$ and it is desirable to estimate the self-field's influence on the thickness dependence of the critical current density.

Derivation

An equation relating $J_c(B)$ to $J_c(c)$ can be derived as follows. It was shown above, that $B_f = \mu_0 H_f$ is a proper estimate when the self-field comes into effect. The observation that $J_c(H)$ remains approximately constant at fields below B_f (see Fig. 8.8) leads to

$$J_c(H = 0) \approx J_c(H = H_f). \quad (8.2)$$

Moreover, we have seen that the self-field does not play a role at high fields—here, $J_c(H)$ is equivalent to the material law $J_c(B)$. If we assume that this approximation is still valid at the beginning of the self-field regime, we can write

$$J_c(B = \mu_0 H_f) \approx J_c(H = H_f) \quad (8.3)$$

and combining (8.2) and (8.3) results in

$$J_c(B = \mu_0 H_f) \approx J_c(H = 0). \quad (8.4)$$

If we assume H_f to be proportional to the sheet critical current density at self-field ($H_f \propto cJ_{c,\text{sf}}$) we arrive at

$$J_c(B = \mu_0 \gamma c J_{c,\text{sf}}) \approx J_{c,\text{sf}}. \quad (8.5)$$

(The factor $1/\pi$ of the initial definition of B_f is replaced by an arbitrary factor γ to be identified by least squares fitting.) The above implicit equation allows calculating the depression of the self-field critical current density with thickness, if an analytic expression for $J_c(B)$ is available. Two commonly used expressions for $J_c(B)$, the power-law and the Kim model, are treated in the following sections simulating a sample with a cross-section of $1 \times 100 \mu\text{m}^2$.

Power-law

While (8.5) must be solved numerically in the general case, there is an analytical solution for the power-law:

$$J_c(B) = J_1 \left(\frac{B}{B_1} \right)^{-\alpha} \quad \rightarrow \quad J_c(c) = \left[\frac{J_1 B_1^\alpha}{(\mu_0 \gamma c)^\alpha} \right]^{\alpha/1+\alpha}. \quad (8.6)$$

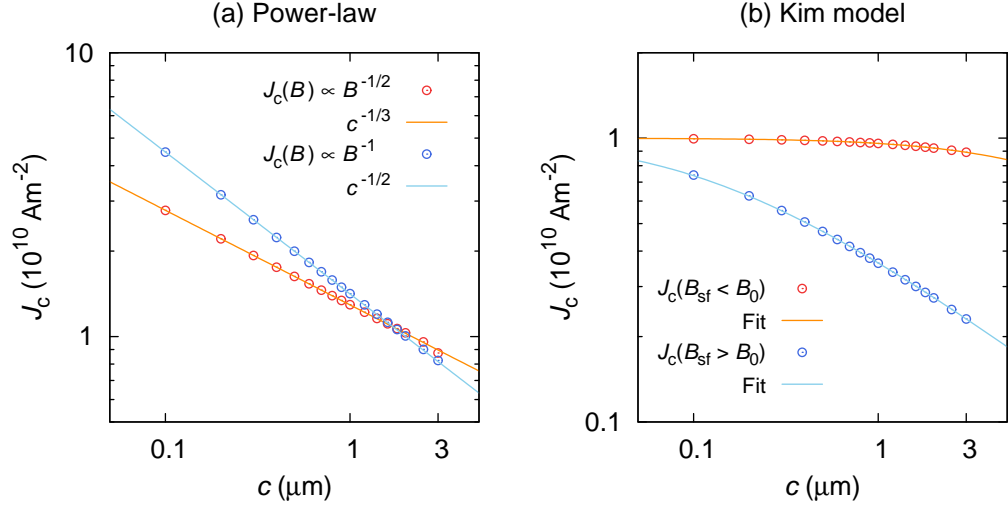


Figure 8.9. The derived equation agrees excellently with the computed data and holds in the entire thickness range. If the self-field is smaller than B_0 of the Kim model, the thickness dependence is very weak (red curve). But if the self-field exceeds B_0 , $J_c(c)$ is equal to a power-law with exponent $\alpha = 1$ (approximately above $1 \mu\text{m}$ for the blue curve).

Here, α is the power-law exponent; B_1 is 1 T and J_1 , the critical current density at $B = B_1$, was set to 10^9 Am^{-2} in all the simulations.

Figure 8.9a demonstrates that (8.6) is in very good agreement with the simulation for two different sets of parameters; the equation correctly predicts $J_c(c)$ in the entire thickness range typically covered by experiments (100 nm up to several microns). Fitting the simulated curve to (8.6) identifies the factor $\gamma \approx 0.37$. The value is reasonably close to $1/\pi \approx 0.32$, which proves that B_f correctly measures the self-field effects.

Kim model

Equation (8.5) can be solved also for the Kim model

$$J_c(B) = \frac{J_0}{1 + B/B_0} \quad \rightarrow \quad J_c(c) = \frac{B_0}{2\mu_0\gamma c} \left(\sqrt{1 + 4\mu_0\gamma c J_0/B_0} - 1 \right), \quad (8.7)$$

parametrised by $J_0 = 10^{10} \text{ Am}^{-2}$, the current density at zero magnetic induction. The second parameter, B_0 , remained uninterpreted in the original work [50]. It simply induces a transition between $J_c \propto 1/B$ at fields above and the flat $J_c \approx J_0$ at fields below B_0 . Again the equation derived above agrees excellently with the simulation (see Fig. 8.9b). Moreover, almost identical values are found for γ .

Exploring the limits of small and large B_0 elucidates the results of the computation. If $B_f \ll B_0$, the magnetic induction in the sample will be below B_0 almost everywhere and $B \ll B_0$ can safely be assumed. Taylor expansion of the root in (8.7) results in

$$J_c \approx J_0 = \text{const.} \quad (8.8)$$

independent of the sample thickness, because the self-field is too low to decrease the critical current density significantly. This is approximately the case for the entire first run of the simulation, where $B_0 = 100 \text{ mT}$ does not exceed B_f (approximately 10 mT at a thickness of $3 \mu\text{m}$).

For fields $B_f \approx B \gg B_0$ on the other hand

$$J_c(c) \approx \sqrt{\frac{J_0 B_0}{\mu_0 \gamma c}} \quad (8.9)$$

because the self-field controls the thickness dependence, which is the case in the second run ($B_0 = 1 \text{ mT}$). Consequently the same inverse square-root thickness dependence is found in agreement with the result derived in the previous section for a power-law with exponent $\alpha = 1$.

Chapter 9.

Magnetisation measurements

Due to the large number of samples investigated, the following discussion will emphasise specific aspects of individual samples and compare the best available films of each growth technique.

Magnetisation measurements of the critical current density were carried out in a VSM at temperatures ranging from 5 to 77 K and in fields of up to 5 T. Before the magnetic characterisation, the samples were scanned in the remanent state to check their homogeneity and, as for instance the PLD samples, cut to fit into the sample space of the instrument. The transition temperature was determined by AC SQUID measurements.

On single-crystalline substrates the highest J_c , exceeding $2 \times 10^{10} \text{ Am}^{-2}$ at liquid nitrogen temperature and self-field, is obtained for the PLD samples. The best MOD film are similar, but samples grown by HLPE conduct a significantly lower J_c of typically 10^{10} Am^{-2} , which compares well to [13]. The critical current density is uncorrelated with T_c (about 90 K in all the samples) and independent of the transition width ΔT_c , which is below 1 K in nearly all the samples. (Table 9.1 summarises the key parameters of the samples discussed in this section.)

Although J_c is closely related to flux pinning in the material, the sheet current density K_c is more important from a technical point of view, because it measures the current per unit width the film conducts in the critical state—a key quantity for any application. The PLD films were only grown to a thickness of 200 nm and thus conduct a small sheet current density K_c of around 50 A/cm despite their high J_c ; the same is true for the MOD samples provided by ICMAB (SS1646 and SS1648). From this perspective these samples are inferior to the HLPE conductors. For HLPE, the relatively low J_c is compensated by the large thickness of the films: the 2.9 μm thick sample HR60 carries a current of nearly 300 A per centimetre width. This is a unique feature of the liquid mediated growth process, which allows to deposit thicker films without deterioration [51]. Only a 1 μm thick MOD sample

grown by Nexans (C020306C) approaches the current carrying capability of the best HLPE sample.

The most prominent feature is the difference between samples grown on single-crystalline substrates and poly-crystalline tapes: J_c is lower by a factor of five if the sample is deposited on a metallic substrate. This is primarily a consequence of the early stage of the optimisation of the growth methods—today high performance conductors on metallic substrates are routinely fabricated by PLD as well as by MOD.

9.1. Field dependence of the critical current density

Figure 9.1 shows the field dependence of the critical current density $J_c(B)$ for the best undoped sample of each growth method after correcting for the self-field (cf. section 5.1.1). The effect of the evaluation procedure, which replaces the applied field $\mu_0 H$ by the magnetic induction B , is to shift the measured J_c data to higher values of B ; $J_c(B)$ can therefore not be attained below a certain induction (see also chapter 8). Lowering the temperature increases J_c and thus enlarges the $J_c(B)$ domain inaccessible to magnetisation experiments.

Using the typical field $B_f = \mu_0 c J_c / \pi$ of a thin film in the critical state we can sketch the self-field regime $J_f(B)$ in the J - B plane for a thin film as follows: Owing to the Biot-Savart law the correction depends linearly on the currents flowing in the sample and we can write $J_f(B) \propto B$, because the correction must vanish, when the current is zero. The condition, that a measurement at zero applied field is shifted by about B_f reads

$$J_f(B = B_f) \approx J_c(H = 0). \quad (9.1)$$

Employing the zero field critical current density a second time to estimate $B_f \approx \mu_0 c J_c(H = 0) / \pi$ results in

$$J_f(B) = J_c(H = 0) B / B_f = \frac{\pi B}{\mu_0 c}, \quad (9.2)$$

which is, of course, the same as solving $B_f(J)$ for $J = J_f(B)$. Figure 9.1a–d shows, that (9.1) agrees well with the evaluation procedure—although the estimate is based on the simplest assumptions, it is sufficient to indicate the self-field domain in the single-crystalline samples.

After a more careful inspection it seems that, for example in HR55 (cf. Fig. 9.1b), the self-field is not properly accounted for, because the low field $J_c(H)$ plateau

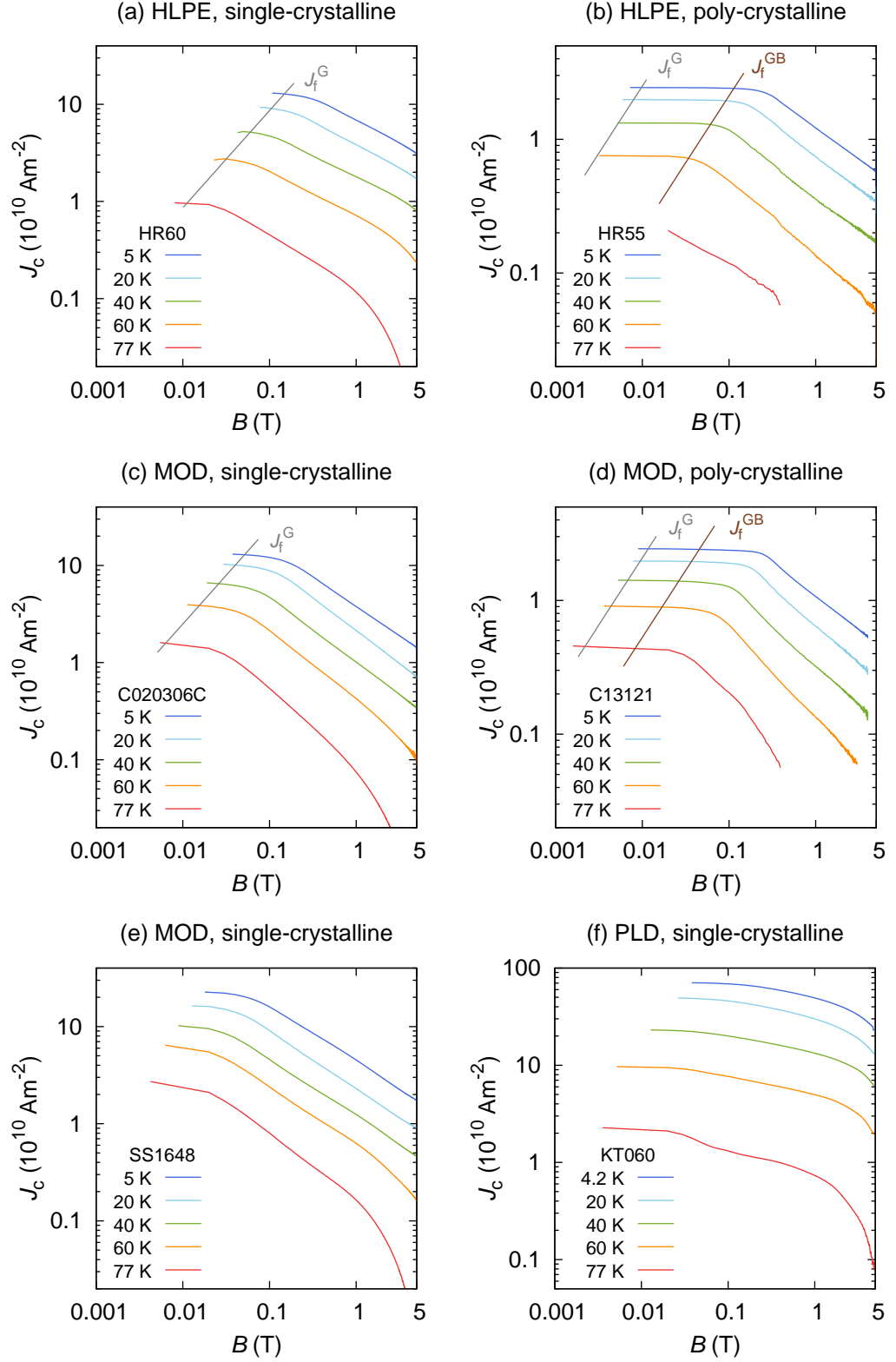


Figure 9.1. Field dependence of the critical current density in samples grown by various (HLPE, MOD, PLD) methods on poly- and single-crystalline substrates showing estimates of the self-field domain with (grey) and without (brown) accounting for the granularity in the sample.

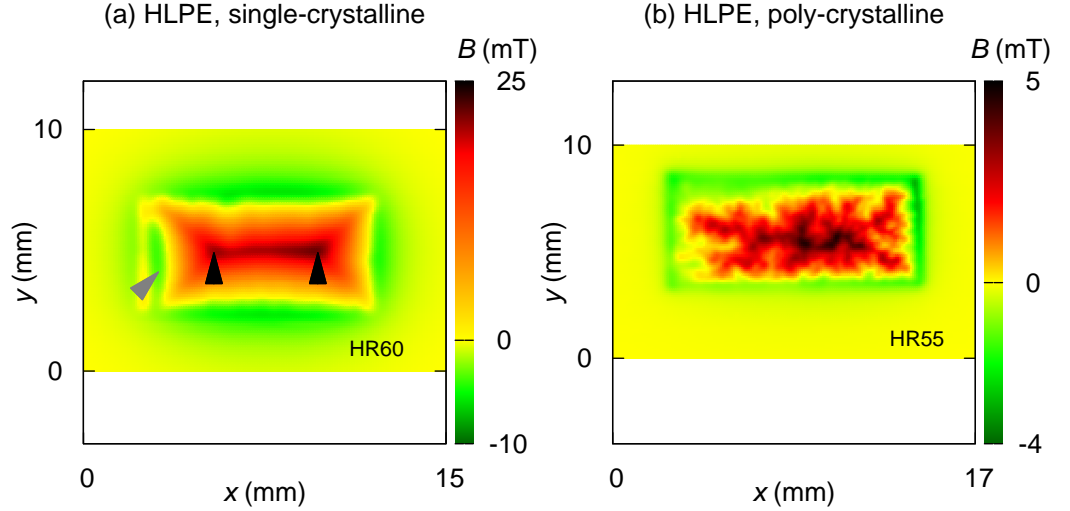


Figure 9.2. Hall scan of HLPE coated conductors. (a) Apart from the area close to the left edge (grey arrow), which was covered by a clamp during the deposition, the trapped field profile is smooth, if the sample is grown on single-crystalline substrates. According to the Bean model the profile resembles a rooftop, which peaks twice at the centre line of the sample (black arrows). (b) Growth on poly-crystalline samples induces a coarse granular pattern HR55, which indicates strong local variations of the critical current density.

is only partially removed by the $J_c(B)$ evaluation procedure. The puzzling effect can be interpreted in terms of the granularity of the sample and by distinguishing between the intra- and inter-grain critical currents. For any reasonable grain size in the sub-millimetre range the latter component establishes the magnetic moment of the sample alone (cf. section 5.1.2). The intra-grain currents can therefore affect the measurement only indirectly by influencing the inter-grain currents, for example by applying a field at the edge of the grain which suppresses the current crossing the grain-boundary.

It is possible to account also for this scenario. Suppose that J_c^G is unaffected by the granularity and remains high on a metallic tape, the field applied at the grain-boundary will be approximately as high as the mean self-field of a single-crystalline sample. Hence it is clear that the evaluation scheme, which computes the internal induction based on J_c^{GB} only, fails and the $J_c(H)$ plateau thus enters $J_c(B)$. Accordingly (9.2) can be reformulated for a grain-boundary critical current density J_c^{GB} by revising condition (9.1) to

$$J_f^{GB}(B = B_f^G) \approx J_c^{GB}(H = 0), \quad (9.3)$$

which states that the self-field J_c is shifted by the typical field of a single-crystalline film B_f^G and not by the self-field of the intergranular currents. The resulting equation

$$J_f^{GB}(B) = \frac{\pi B}{\mu_0 c_{GB}} \frac{K_c^{GB}(H=0)}{K_c^G(H=0)} \quad (9.4)$$

expresses the self-field domain in terms of the thickness of a granular sample c_{GB} and the relative decrease of K_c on a granular substrate.

Evaluating this ratio at an intermediate temperature of 40 K results in a satisfactory account of the self-field plateau in sample HR55, when using HR60 as a reference. Indeed Hall scans clearly show a smooth trapped field profile in single-crystalline and a granular pattern in the sample of poly-crystalline tape (cf. Fig. 9.2). It is important to note that the length scale of the field variation (about a millimetre) is not related to the grain size of the substrate, which is in the range of a few (tens of) micrometres [14] and below the resolution of the Hall probe. Nevertheless, the above equation applies here, because it does not explicitly contain the lateral dimension of the grains—it simply assumes that currents cross weak boundaries in the vicinity of strongly pinning area with a local trapped field comparable to a single-crystalline sample.

The same effect, although less quantitative agreement, is found in two MOD samples provided by Nexans (see Fig. 9.1c–d). The applicability of (9.4) to granular HLPE and MOD samples indicates that J_c^G is considerably higher than J_c^{GB} and probably similar to J_c on single-crystalline substrates. This emphasises that granularity and not a lack of pinning is the main source of the low currents.

9.1.1. Identification of the α -value

The decrease of J_c in a magnetic field is often well described by a power-law field dependence

$$J_c(B) \propto B^{-\alpha}, \quad (9.5)$$

which serves to quantify the strength of the decay by a single parameter. Fits to (9.5) were performed in the range between the end of the self-field domain and 1 T. Generally the power-law remains valid up to the highest fields, except at 77 K, where an exponential decay sets in at roughly 4 to 5 T, which is possibly due to thermal activation.

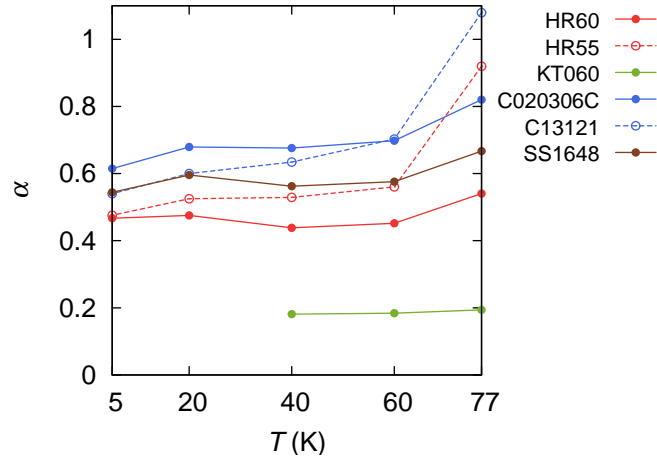


Figure 9.3. Temperature dependence of the α -value. The in-field decrease of critical current density relative to the self-field weakens at lower temperatures and the majority of samples arrives at $\alpha \approx 0.4 - 0.6$ regardless of the crystallinity of the substrate. In the applicable range the power-law exponent is by far the lowest in the PLD samples.

Among all the samples the performance of PLD films is the best. The exponent α is about 0.2 in the applicable temperature range (above 40 K) and not matched by any other sample even at a temperature of 5 K. The PLD sample also shows the strongest temperature dependence of J_c , which increases much faster with decreasing temperature than in all the other samples. It reaches $7 \times 10^{11} \text{ A m}^{-2}$ at liquid helium temperature; this points to a very effective defect structure in this material.

The strongest field dependence of J_c is observed in the MOD samples from ICMAB (SS1646 and SS1648). This demonstrates the need for additional pinning in the material, which was achieved by introducing BaZrO_3 nanoparticles [52]. At low temperatures α is approximately 0.5 in all the samples regardless of growth method and substrate. This value is frequently reported for YBCO thin films and usually interpreted by pinning of sparse large defects, in agreement with theory [53].

9.2. Effect of doping

Superconducting thin films already contain a high degree of structural imperfection because the growth conditions are far from the thermodynamic equilibrium. A direct consequence of these numerous as-grown defects is the high critical current

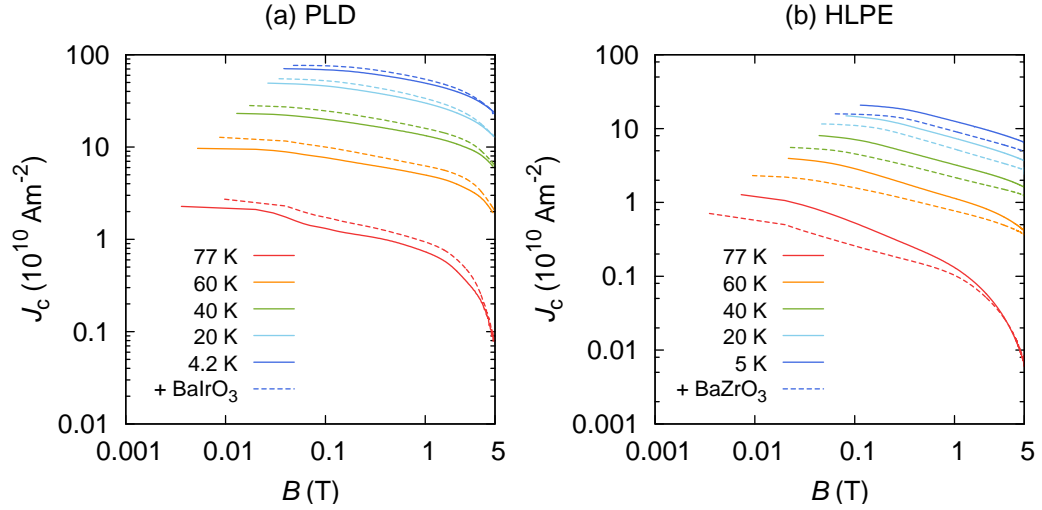


Figure 9.4. Critical current density in doped conductors. (a) The multilayer PLD sample KT046 contains BaIrO_3 and has a higher critical current compared to the reference sample KT060 in the entire field and temperature range. (b) The addition of BaZrO_3 in FH725 reduces the critical current, but enhances the field dependence relative to the standard sample FH719.

density, which is higher by about a factor of hundred compared to single crystals, but decays in applied magnetic fields. With technical applications in mind it was shown in [54] that the formation of nanometre sized precipitates of the secondary phase BaZrO_3 significantly increases the in-field performance. Up to now this idea has stimulated an ever-growing number of research papers dedicated to the precipitation of various phases in the film. About ten samples grown by PLD and HLPE with secondary phases were available for this work.

Two PLD multi-layer samples were created by alternately ablating an YBCO and a transition metal (KT046 and KT062 contained Ir and Hf) target (see also section 3.1). The theoretical thickness of the deposited dopand layer was below one unit cell, which leads to the formation of dispersed islands of nanometre size [9, 10]. Compared to the reference sample KT060 both multilayer samples show a higher critical current density in the entire field and temperature range; enhanced critical currents by BaIrO_3 doping (Fig. 9.4a graphs samples KT046 and KT060) were previously reported in [9]. It should, however, be noted, that the geometry is not accurately defined due to the (unavoidable) cutting of the samples.

Growth of BaZrO_3 in the HLPE film FH725 was achieved by preparing a stoichiometric laser target containing 5 mol % of the dopand; the formation of the phase was confirmed by X-ray diffraction (see Fig. 9.5). FIB thickness measurements enable an exact calculation of the critical current density and show that the critical

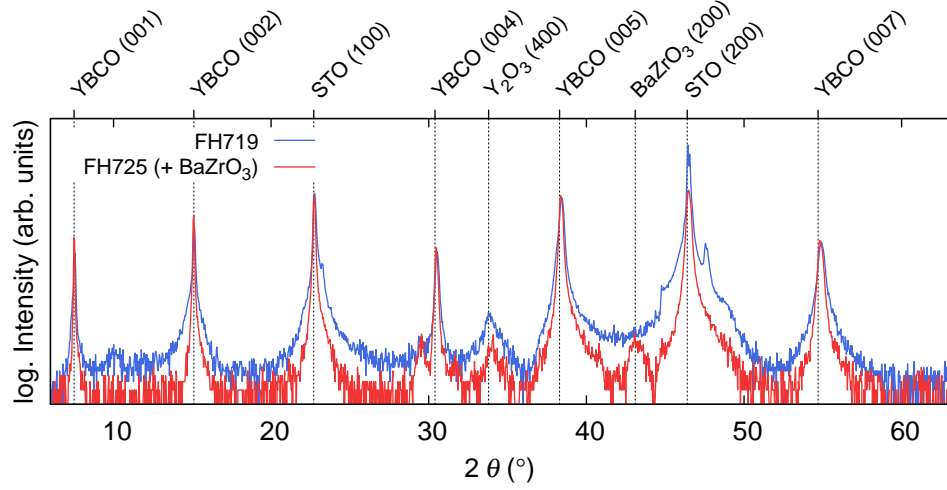


Figure 9.5. X-ray diffraction on HLPE films showing YBCO reflections and the signal of the STO substrate. Prominent Y_2O_3 peaks are common in all the samples; the formation of BaZrO_3 in FH725 is clearly seen in the θ - 2θ scan.

current density is lower in FH725 than in a standard sample grown under the same conditions, but from a pure YBCO target (FH719). However, the introduction of BaZrO_3 reduces the field dependence of $J_c(B)$ significantly and α decreases from about 0.55 to below 0.4 for $H \parallel c$. (see Fig. 9.4b). Consequently samples containing BaZrO_3 were grown for transport measurements.

Table 9.1. Key data of the samples used for magnetic measurements. HLPE samples are from UCAM and PLD samples from IFW Dresden. MOD samples starting C with are provided by Nexans, those starting with S were grown at ICMAAB. ([§]BaZrO₃ contents, [†]Ir doped, [‡]Hf doped, [£]resistive T_c measurement, [↓]FIB thickness measurement.)

	Code	Substrate	Thickness (μm)	$T_c/\Delta T_c$ (K)	$J_c(77\text{ K, sf.})$ (10^{10} Am^{-2})	$K_c(77\text{ K, sf.})$ (A/cm)
HLPE	HR22	Ni-NiO	1.5	—	0.27	41
	HR55	Ni-NiO	1.0	—	0.27	27
	HR60	STO	2.9	91.0/0.4	0.97	281
	HR66	STO	2.9	90.7/0.7	0.20	58
	FH719	STO	1.9 [↓]	90.3/1.7	1.27	241
	FH725 [§]	STO	1.4 [↓]	88.3/0.6	0.71	99
MOD	C020306C	YSZ	1.0	89.8/0.5	1.60	160
	C13121	RABiTS	1.2	—	0.46	55
	C22111	RABiTS	1.0	—	0.23	23
	SS1646	LAO	0.275	91.0/1.4	1.65	45
	SS1648	LAO	0.275	91.5/0.6	2.71	75
PLD	KT046 [†]	STO	0.2	90.1/0.4 [£]	2.71	54
	KT060	STO	0.2	90.7/0.6 [£]	2.27	45
	KT062 [‡]	STO	0.2	89.5/0.5 [£]	2.90	58

Chapter 10.

Transport measurements

10.1. Anisotropy of the critical current density

The previous chapter on magnetisation measurements discussed the critical current density exclusively for fields parallel to the crystallographic c -axis of the films.¹ But certain applications, as for example research magnets, require high performance at fields aligned parallel to the a,b -planes—the anisotropy of the critical current density is thus of great technological importance. Moreover, anisotropy measurements provide insight into the pinning mechanism, because the shape of the anisotropy curve $J_c(\phi)$ depends—apart from the intrinsic anisotropy of the material—on the dimension and density of the material defects, which pin the vortex lattice. To which extent secondary phases, which are the main candidates for improving $J_c(B)$ at high fields, shape the anisotropy curve, is of particular interest.

10.1.1. Doping

Transport measurements were carried out on four HLPE samples using the two-axis probe of the 6 T-system. All the samples were grown on single-crystalline STO: a standard HLPE film (FH750) serving as a reference sample, two samples containing 5 mol % BaZrO₃ and BaHfO₃ (FH751 and FH752), and a film deposited on an Y₂O₃ decorated substrate (FH753). In order to eliminate resistive heating of the contacts the critical current of the films was reduced by patterning the samples to 10 μm wide tracks as described in section 3.4. The thickness of samples FH750

¹ The vector VSM, which is equipped with a rotatable sample rod and two orthogonal coil sets, allows to measure magnitude and direction of the magnetic moment at arbitrary angles of the applied field. Due to the high aspect ratio of the sample cross-section the currents flow—similar to transport measurements—parallel to the a,b -planes. A magnetic determination of the critical current anisotropy based on the standard evaluation of hysteresis loops is, however, not straightforward; in this way encouraging results were obtained only in a narrow angular range around $H \parallel c$.

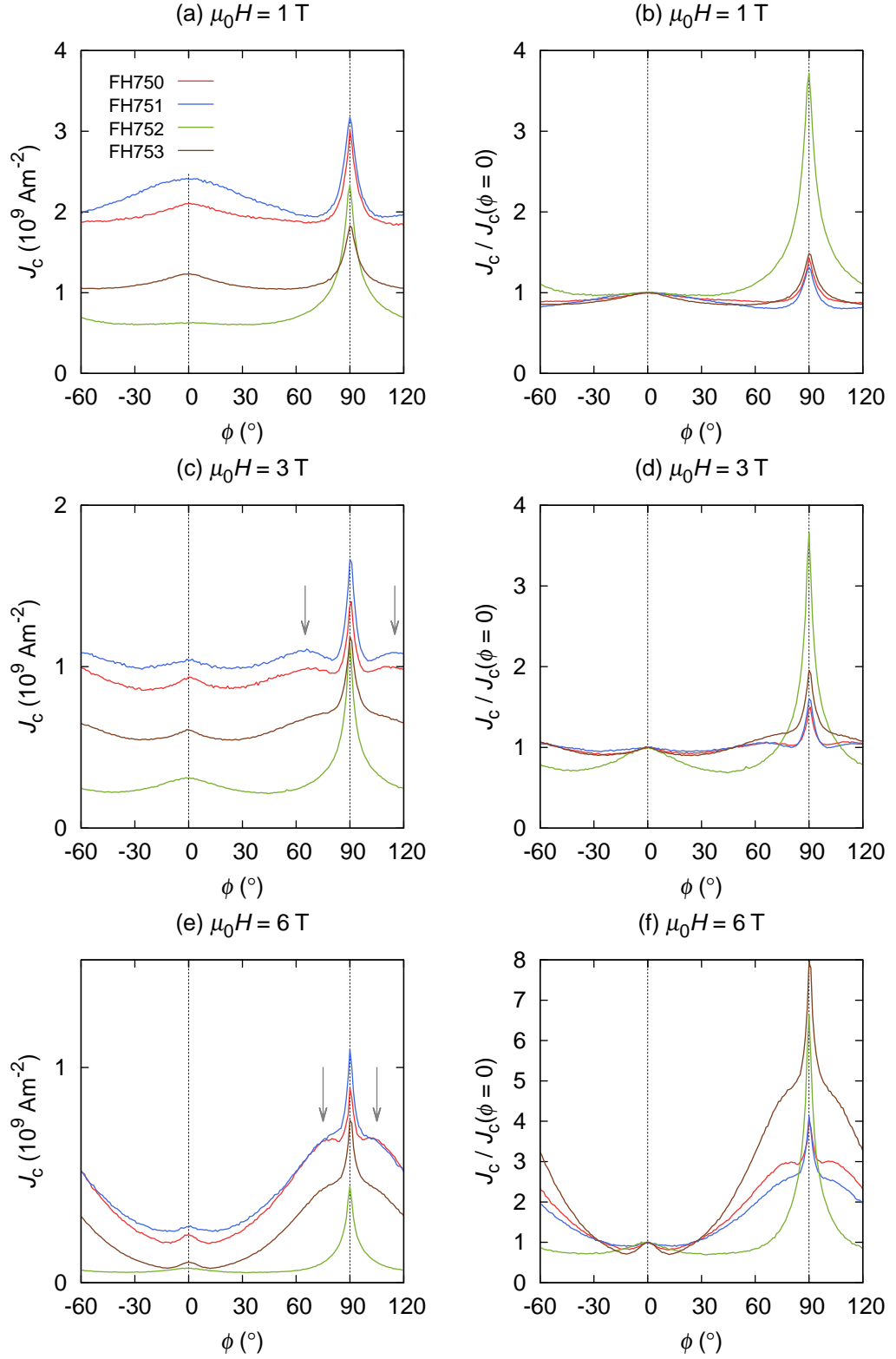


Figure 10.1. Anisotropy of J_c in doped HLPE films. The c -axis peak is most pronounced in the film containing BaZrO_3 at fields below 1 T. Prominent features are the sharp a,b -peak and the shoulders close to it (grey arrows), occurring in all samples except FH752 at fields above 3 T.

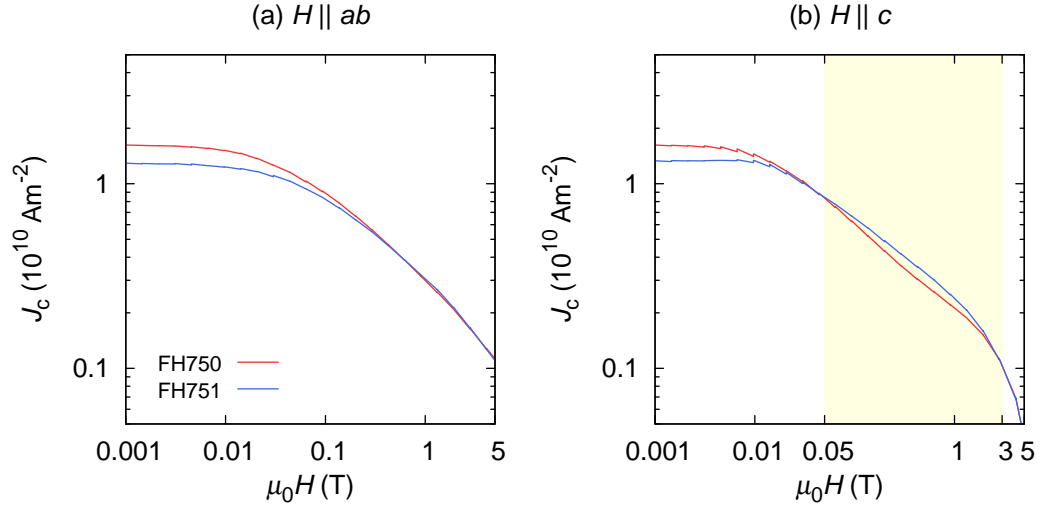


Figure 10.2. Field dependence of J_c in HLPE films. Although the film containing BaZrO_3 conducts a lower critical current at self-field, the secondary phase in FH751 enhances the critical current density for intermediate fields $H \parallel c$ (yellow area); the performance is similar at the highest fields for both main directions.

and FH751 is $0.72 \mu\text{m}$ and $0.8 \mu\text{m}$ as determined by FIB measurements; the other films are assumed to be $1 \mu\text{m}$ thick [55].

Table 10.1 summarises key properties of all the samples. The superconducting transition occurs at around 90 K in all the samples, which is similar to the results of the magnetic measurements. The transition temperature does not vary systematically with J_c in the expected way, i.e., the sample with the highest T_c (FH752) has the lowest J_c at 77 K and self-field, indicating the minor influence of the already small T_c variation. Comparing the magnetisation and transport measurements on all the HLPE samples, whose thickness is accurately known owing to FIB measurements, shows that the self-field J_c at this temperature is highest in the reference sample FH750 (about $1.6 \times 10^{10} \text{ Am}^{-2}$), but still significantly less than in the PLD or the best MOD samples. Moreover, the introduction of BaZrO_3 lowers J_c at self-field relative to the reference sample, an effect already seen in the magnetisation measurements (cf. Tbl. 9.1).

The critical current anisotropy, which was measured at 77 K and in maximum Lorentz force configuration, is qualitatively similar in all the samples except FH752: The anisotropy $J_c(H \parallel ab)/J_c(H \parallel c)$ is reduced to approximately 1.5 at 1 T by a pronounced c -axis peak (cf. Fig. 10.1), which indicates pinning centres preferentially aligned in this direction. Those defects are most effective at low fields: the c -axis peak decreases and the relative anisotropy increases at higher

fields. No c -axis peak is found in sample FH752, which is strongly anisotropic in the entire field range.

From a technological perspective a reduction of the field dependence for the weak pinning direction $H \parallel c$ is highly desirable. Similar to the results of the magnetisation measurements, the field dependence is reduced by introducing BaZrO₃ (α decreases from approximately 0.46 to 0.41); the effect is, however, limited to fields below 3 T (cf. Fig. 10.2). This is the range, where the c -axis peak is broader and higher than in the reference sample, which points to a higher density of c -axis correlated defects as the source of the additional pinning in FH751. The above result together with the magnetisation measurements suggests that BaZrO₃ additions are most promising for improving the field dependence $J_c(H \parallel c)$ in HLPE films [56].

10.1.2. Correlation between the n -value and J_c

Prominent features of the anisotropy curve are the sharp a,b -peak and the shoulders close to $H \parallel ab$, which occur at fields above 3 T in all the films except in FH752. This effect is frequently found in YBCO films (for example in [57] at the same temperature and field), but rarely discussed due to its puzzling nature. The standard interpretation, which explains an improved J_c at a certain angle in terms of a preferential alignment of defects, does not apply here, because there is no reason why material defects should strongly correlate in a direction, which does not coincide with a principle axis: the shoulders are neither parallel to the substrate (a,b -plane) nor aligned in the growth direction (c -axis).

More insight into pinning in these films can be gained by analysing the individual I - V curves. It was shown in chapter 1 that the electric field in the flux-creep regime follows a power-law, which is parametrised by the critical current density J_c and the n -value exponent at a fixed electric field criterion (cf. section 5.2.1). The two parameters are not completely independent: Generally, one expects that J_c is a function of the elementary pinning force $f_P = U_p/\xi$, where U_p represents the energy gain of a pinned flux line. Further, the n -value is, under the assumption of a logarithmic dependence of the activation energy on the current, proportional to the energy scale of the activation barrier U_0 (see chapter 1), a quantity similar to U_p . Combining these arguments results in a relation between the n -value and J_c for a certain pinning regime—although the functional dependence is unknown.

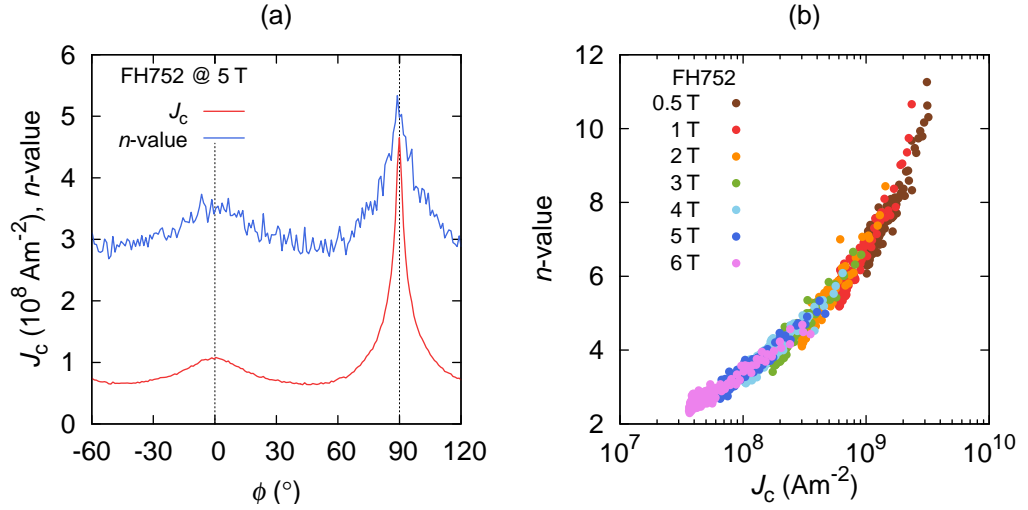


Figure 10.3. Correlation between the n -value and J_c in FH752. (a) Especially at high fields J_c and the n -value are closely correlated. (b) The entire data-set, which consists of more than 1000 points, collapses onto a single smooth curve, although both magnitude (0.5 to 6 T) and direction (more than 180°) of the applied field are varied.

Figure 10.3 provides evidence for such a relation in the sample without shoulders: all n -values collapse onto a single smooth curve.² The strong correlation is remarkable, because the plot contains the entire field and angular range of seven anisotropy measurements—a data-set with more than thousand points. Moreover, J_c varies by two orders of magnitude, which provides additional support for the argument that a functional dependence between the n -value and J_c exists within one pinning regime.

The situation is different in a sample with shoulders (FH750). Although at high fields the n -value clearly depends on the current within a broad angular range around $H \parallel c$, the curve kinks abruptly at a certain angle and the n -value remains constant, independently of the applied field (about 7). The effect is most pronounced at high fields (> 3 T), where the kink angle agrees with the beginning of the a,b -peak (see Fig. 10.4). This suggests a transition into another pinning regime at this angle, which is characterised by a different n -value/ J_c relation.

A sharp a,b -peak and a change in the n -value/ J_c correlation has previously been discussed in terms of intrinsic pinning by the a,b -planes [59]. Probably the prominent c -axis peak in the samples with shoulders is created at the expense of a,b -aligned defects, whose density is reduced similarly to HLPE films grown

² The n -values are generally smaller than in state of the art coated conductors [30], but similar to those reported for other HLPE films [58].

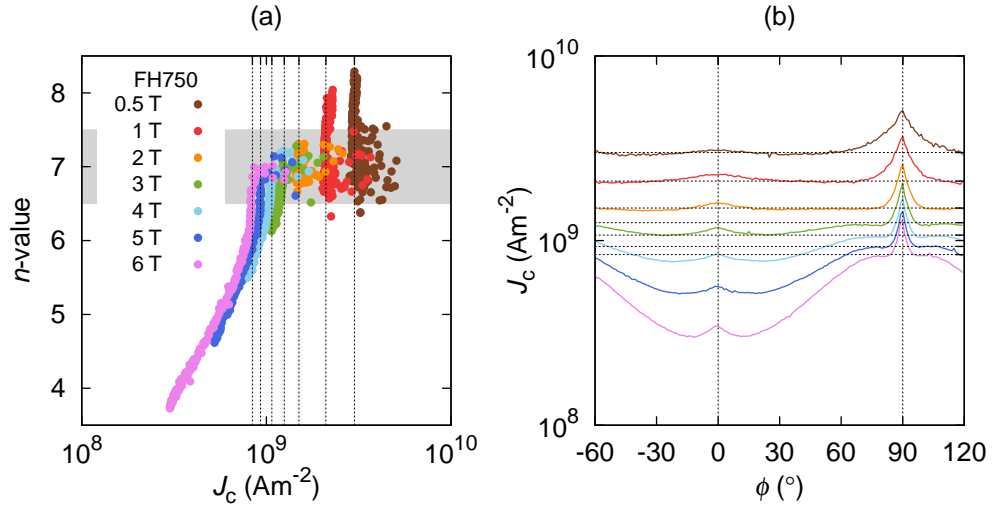


Figure 10.4. Correlation between the n -value and J_c at maximum Lorentz force. In particular at high fields the n -value clearly depends on J_c for a broad angular range around $H \parallel c$. Above a certain angle, the n -value remains constant and is about 7, independently of the applied field; the angle corresponds to the beginning of the a,b -peak in the anisotropy curve. This possibly indicates the transition into a regime, where another defects structure becomes effective.

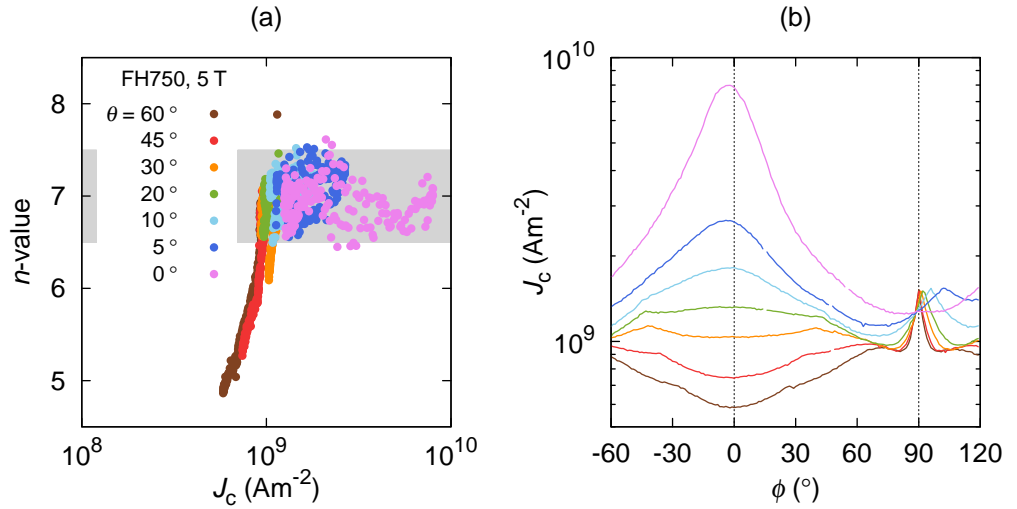


Figure 10.5. Correlation between the n -value and J_c at variable Lorentz force. Identical to measurements under maximum Lorentz force configuration, the n -value is about 7 as soon as the vortices are close to the a,b planes ($\theta = 0^\circ$) regardless of the magnitude of the Lorentz force. The current at $\theta = \phi = 0^\circ$ is approximately force free.

at low rate [58]. If this is the case, the reduced density of planar defects reveals the contribution of intrinsic pinning close to $H \parallel ab$ in these samples; the effect becomes more pronounced at elevated fields, where the a,b -planes outnumber all other defects.

Further experimental evidence for this scenario, i.e., that a transition into another pinning regime occurs close to $H \parallel ab$, can be obtained by exploiting the full angular range of the goniometer, which allows to set any direction between the magnetic field and the sample's crystallographic system. So far all the measurements have been carried out in maximum Lorentz force configuration, i.e., the magnetic field was rotated in a plane perpendicular to the current ($\theta = 90^\circ$). Decreasing θ reduces the angle between the magnetic field and the a,b -planes until the magnetic field is parallel a,b at $\theta = 0^\circ$ independently of ϕ , which varies only the Lorentz force (cf. Fig. 4.4). Such variable Lorentz force measurements at 5 T are in full agreement with the above results: the n -value is again 7, if the magnetic field is close to the a,b -planes. Moreover, the exponent is independent of J_c and the magnitude of the Lorentz force, which varies greatly between approximately force free (the eminent peak at $\phi = 0^\circ$) and maximum Lorentz force ($\phi = 90^\circ$), if θ is zero.

The high density of a,b -planes (the YBCO crystal cell is about 1 nm high) provides also a possible explanation for the field independence of the n -value close to $H \parallel ab$, because the a,b -plane distance is always shorter than the vortex spacing ($a_0 = \sqrt{\Phi_0/B} \approx 20$ nm at 6 T) and the a,b -planes will provide, in contrast to all the other defects in the film, unoccupied pinning positions at all applied fields—thermal activation processes will, therefore, be field independent and occur at an intrinsic rate.

10.2. Irreversibility line

The irreversibility field as a function of temperature $B_{\text{irr}}(T)$ was determined for a number of HLPE films deposited on single-crystalline STO and on metallic tapes. Strong resistive heating—presumably by the metal-YBCO interface of the contact pads—impeded measurements of the transport critical current at temperatures below 77 K, but is insignificant when determining the irreversibility field due to the low excitation currents.³ Irreversibility fields $H \parallel c$ exceeding 12 T at 77 K are found

³ Here, a current of 1 μA raises the voltage drop well above the noise level of the system. Although the exact value is arbitrary, it does not influence the result: the resistance remains the same at the tenfold current (cf. Fig. 5.5). This is exactly what a superconductor in the

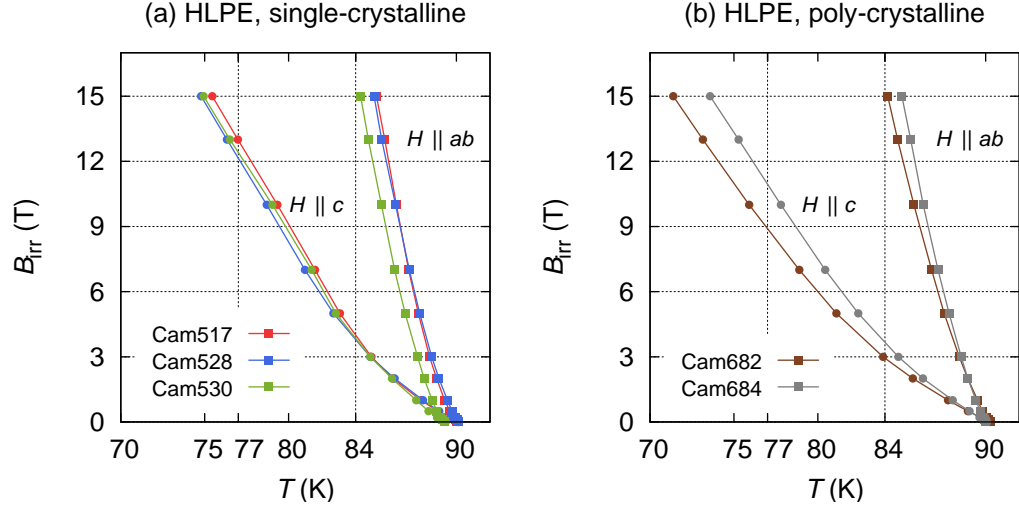


Figure 10.6. Irreversibility line in HLPE films and coated conductors. (a) Irreversibility fields B_{irr} exceeding 12 T at 77 K are reached in the samples on single-crystalline substrates for fields $H \parallel c$. (b) The irreversibility line is significantly lower in granular samples on metallic substrates.

in all the HLPE samples grown on single-crystalline substrates (see Fig. 10.6). The sample to sample variation is small, indicating reproducible material properties, which are unaffected by the BaZrO_3 content in Cam530. On granular metallic substrates, B_{irr} is clearly smaller (around 9 T for $H \parallel c$), which compares well with state-of-the-art conductors [30].

Approximately the same values of around 12 T for $H \parallel c$ at 77 K are obtained in PLD multilayer samples grown on STO. The values agree fairly with a Hf multilayer grown in the same way [10], which showed strongly enhanced irreversibility fields compared to an undoped reference sample. Here, the results were again almost independent of the dopant material: the highest irreversibility line belongs to the undoped reference sample KT060, whereas KT046 and KT062, which contain the transition metals Ir and Hf, have a slightly lower irreversibility field.

Only small variations are found for the other main field direction—the irreversibility temperature T_{irr} is approximately 84 K at 15 T in all investigated HLPE and PLD films for fields $H \parallel ab$.

10.2.1. Power-law fits

The irreversibility line is expected to follow a power-law

TAFF regime is expected to do and justifies an evaluation scheme using a resistance criterion relative to the normal conducting state as described in section 5.3.

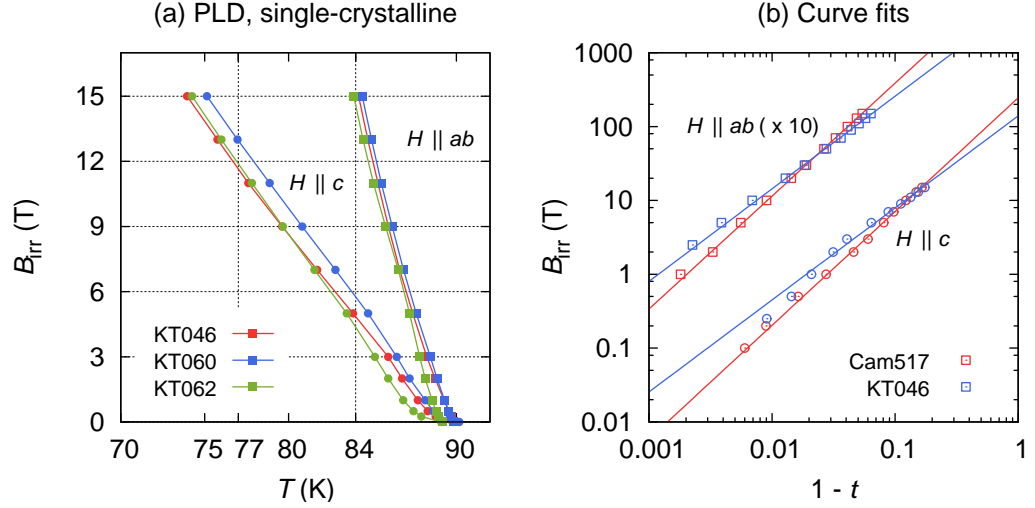


Figure 10.7. Irreversibility line in PLD films and best power-law fits to the curves. (a) Values similar to the single-crystalline HLPE samples are found in PLD samples deposited on STO for both main field directions. (b) The power-law ($\alpha \approx 1.5$) successfully describes the irreversibility line in the HLPE samples, but fails to account for the high temperature behaviour of the PLD films. (The curves are offset by the indicated factor for better visibility.)

$$B_{irr} \propto (1 - t)^\alpha \quad (10.1)$$

depending on the reduced temperature $t = T/T_c$. Although the parameter α is easily identified on a double logarithmic scale, this should be avoided for reasons already elaborated in section 5.2.1. Instead least squares fits were carried out on a linear scale and in a way that a broader transition ΔT_c , which is equivalent to a larger systematic error caused by the arbitrary 10 %-criterion, has proportionally less weight in the fit procedure.

Equation 10.1 fails to describe the irreversibility line in PLD films for $H \parallel c$, but fits the data on the HLPE sample in the entire range (examples are given in Fig. 10.7). Parameter identification results in $\alpha \approx 1.5$ independent of the field direction. The values are compatible with the flux creep model developed in [60] and similar to the exponents of the coated conductors investigated in [30].

Table 10.1. Key data of the samples used for transport measurements. HLPE samples are provided by UCAM; PLD samples from IFW Dresden were summarized in Tbl. 9.1. (§ BaZrO₃ doped, † BaHfO₃ doped, ‡ Y₂O₃ substrate decoration, $^{\downarrow}$ FIB thickness measurement.)

	Code	Substrate	Thickness (μm)	$T_c/\Delta T_c$ (K)	$J_c(77\text{ K, sf.})$ (10^{10} Am^{-2})	$K_c(77\text{ K, sf.})$ (A/cm)
HLPE	FH750	STO	0.72 $^{\downarrow}$	89.8/1.3	1.61	116
	FH751 §	STO	0.80 $^{\downarrow}$	89.8/1.6	1.31	105
	FH752 †	STO	1.0	90.7/1.8	0.62	62
	FH753 ‡	STO	1.0	89.5/0.6	1.16	116

Chapter 11.

Irradiation

Numerous models claim to describe flux pinning in high-temperature superconductors, but their applicability is not clear (see section 1.1). Especially predicting the influence of size and density of defects on the critical current density is a decisive criterion. Consequently, considerable effort has been undertaken to shape a well defined model defect matrix, for example by heavy ion irradiation, which creates columnar defects in the material, or by the spherical defects generated by fast neutrons (cf. section 4.5).

Neutron irradiation challenges theory as it affects primarily the irreversible parameters, while leaving the reversible parameters such as T_c at moderate fluences almost unchanged. Any change in the observable critical current density can therefore be attributed to the artificial defects of known size and density. In single crystals, for example, the critical current density can be raised considerably by irradiation. The experiment elucidates the puzzling nature of pinning in high-temperature superconductors, but a quantitative account in terms of available theoretical models fails, although the defect structure is now well defined [61].

Apart from pure theoretical interest, neutron irradiation was also applied to bulk superconductors to test their potential performance [62], an approach that is also important for coated conductors, because—in addition to upscaling the production—current research and development is focused on engineering crystal defects by precipitating secondary phases of nanometre size during the growth of the conductor. This represents another strength of neutron irradiation: comparative measurements on the same samples can be carried out, all other parameters being equal, except, of course, the defect matrix. Furthermore, the size of the pinning centres introduced by irradiation is similar to the “ideal size“ a secondary phase inclusion should have. From this perspective neutron irradiation serves as a benchmark, exploring the potential performance of a conductor at an elevated density of optimal defects.

It was further shown that neutron irradiation enhances pinning in the grains of $(\text{BiPb})_2\text{Sr}_2\text{Ca}_2\text{Cu}_3\text{O}_x$ tapes, while it deteriorates to a certain extent the grain-boundaries thus lowering the percolative current passing from one grain to another [63]. This effect was recently used to separate inter- and intragrain current flow in the course of extensive measurements on state-of-the-art YBCO coated conductors [30].

In this work, granularity was found to be more determining than the different growth methods of the samples. The results are therefore summarised according to the substrate the samples were grown on, i.e., single crystals and poly-crystalline tapes are separately discussed.

11.1. Single-crystalline substrates

The first irradiation was dedicated to analyse the potential pinning performance of several samples grown by a number of different methods such as HLPE, MOD and PLD on single-crystalline substrate. A moderate fast neutron fluence of $2 \times 10^{21} \text{ m}^{-2}$ was chosen, which is known to significantly enhance the critical current density J_c , if the sample lacks effective pinning centres and does not deteriorate superconductivity in the sample too much. In order to ensure the latter, the transition temperature was also checked after the first irradiation.

11.1.1. HLPE films

Two HLPE films grown on STO, the first at the optimum temperature of 860°C (HR60) and the second at an elevated temperature of 890°C (HR66), were irradiated. The growth temperature strongly influences the critical current densities: J_c is about $1 \times 10^{10} \text{ Am}^{-2}$ in the first and approximately 5 times lower in the second sample (cf. Tbl. 9.1), in agreement with [13].

The transition temperature T_c was determined by AC SQUID measurement. A moderate decrease by about 0.4 K was found in both samples, which is the result of oxygen disorder introduced by the irradiation; the transition width was not affected.

In order to rule out damages inflicted during handling or mounting of the samples, Hall scans were carried out before and after all measurements. No difference was found in the flux density profile and the change in J_c can therefore be attributed to the effect of neutron irradiation. A slightly increasing maximum trapped field

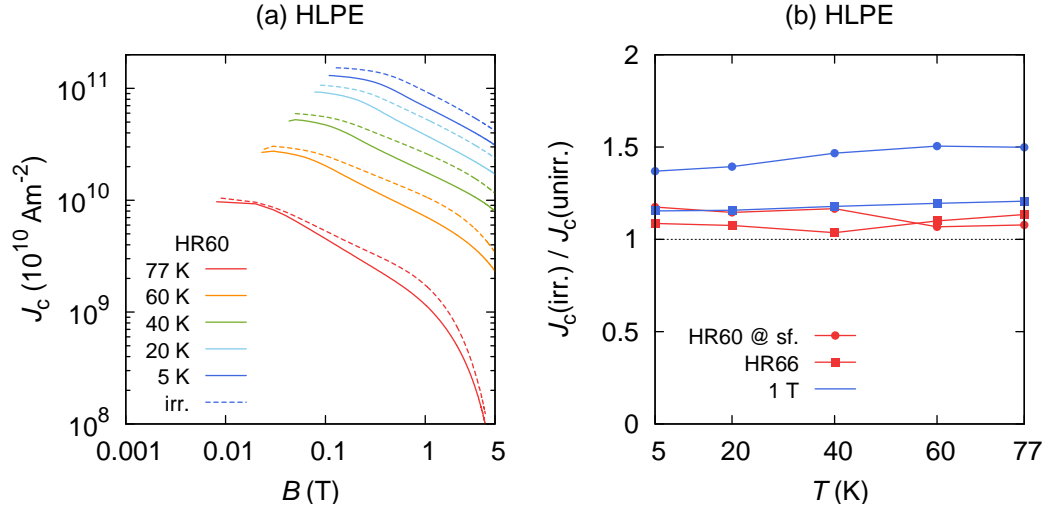


Figure 11.1. Irradiation of HLPE films. Sample HR60 shows an overall increase in J_c at temperatures below 77 K, where the T_c reduction plays no role anymore. The irradiation enhances the in-field performance and results in J_c improvements of up to 50 % at 1 T.

in both samples already indicates an improvement of the self-field J_c at liquid nitrogen temperature, although T_c decreased.

This result was confirmed by VSM magnetisation measurements. It was found that the lowered T_c affected J_c at temperatures close to the superconducting transition and competed with the additional pinning centres: an enhancement is only found above a certain magnetic field. This threshold field decreases with temperature until at liquid nitrogen temperature the irradiated samples show higher J_c also at self-field, in agreement with the scans.

As depicted in Fig. 11.1, sample HR60 responded much more to the irradiation than HR66, i.e., the highest absolute and relative increase in J_c is obtained in the better film. Moreover, the field dependence of $J_c(B)$ was lowered in this sample by the irradiation; at a temperature of 77 K, for example, the α -value decreased from 0.54 to 0.43 (the fit interval ends as in the previous chapters at 1 T). This improvement is comparable to the effect of BaZrO_3 on the transport $J_c(B)$ (see section 10.1.1), but is not limited to intermediate fields: J_c is strongly enhanced in the entire range from the self-field up to 5 T after irradiation. This demonstrates that a substantially higher in-field performance is possible in HLPE samples, where the pinning is optimised.

Generally, the in-field properties benefit most from the irradiation, i.e., J_c improvements of up to 50 % can be found at intermediate temperatures in HR60 at 1 T. The counterintuitive fact that the irradiation was most effective in sample

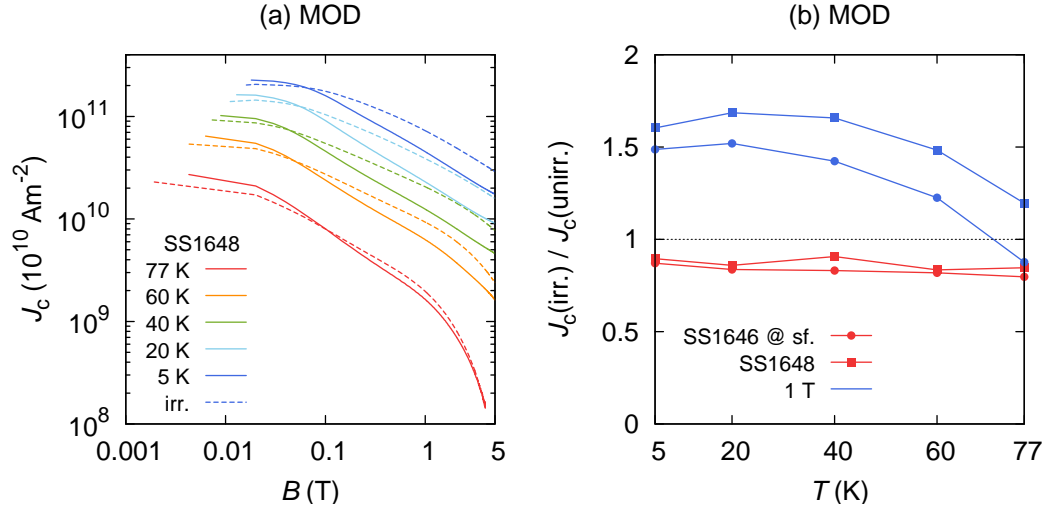


Figure 11.2. Irradiation of MOD films. The strong field dependence of J_c is significantly weakened by the irradiation and a relative J_c enhancement, quite similar to the best HLPE sample, is obtained in both films.

HR60, having an already high critical current density, shows that a lack of pinning centres is not responsible for the diminishing critical current density at elevated growth temperatures in samples grown by HLPE [64].

11.1.2. MOD films

Two 275 nm thick TFA-MOD (SS1646, SS1648) films with high J_c (cf. Tbl. 9.1) were irradiated together with the HLPE samples discussed above. As determined by AC SQUID measurements, the transition temperature decreased by 0.7 K in both samples, while the transition width was again not affected.

Analogous to HLPE coated conductors, J_c significantly increases at 1 T, with the peak enhancement being located at intermediate temperatures of 20 – 40 K. The maximum relative J_c enhancement amounts to 50 % (cf. Fig. 11.2), quite similar to the HLPE coated conductors. The strong field dependence, which characterises the samples, was reduced by the irradiation: the α -value decreased from 0.66 to 0.56 almost identically in both samples. The expected enhancement in pinning agrees with the improved $J_c(B)$ performance due to the successful growth of BaZrO_3 nano-rods and nano-particles in TFA-MOD films [52].

Unlike in the HLPE films there is, however, no improvement at self-field in the entire temperature range. This might result from the residual vacuum grease left on the surfaces, which glued both samples together at some time after sealing the quartz tube. Although the flux density profile indicates that the layers stayed

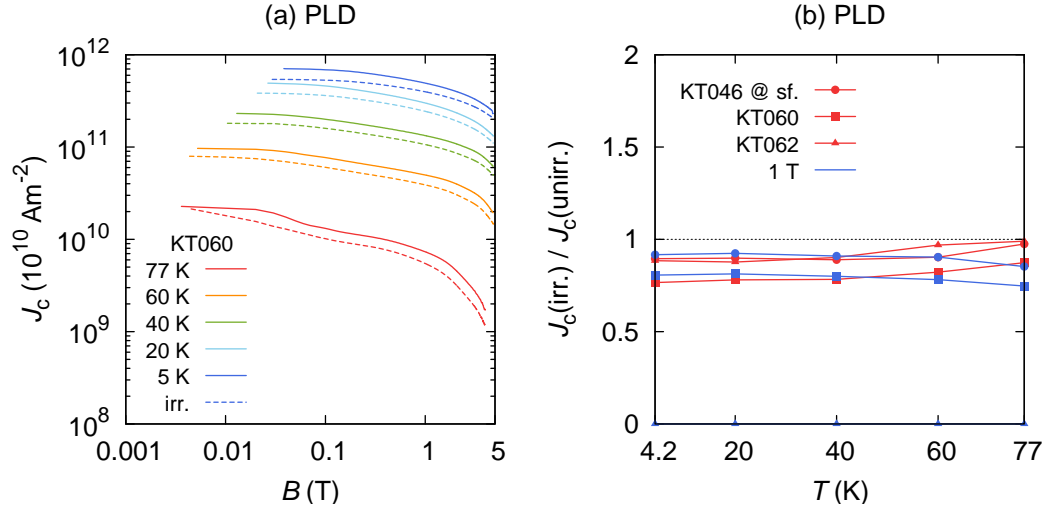


Figure 11.3. Irradiation of PLD multilayers. The films already represent an optimised pinning system and the irradiation does not improve the performance of the films in the entire temperature and field range.

intact after separation, a homogeneous deterioration of the uppermost layer, for example by residual moisture contained in between the films, cannot completely be excluded because the samples were, unlike the thin PLD films, not covered with a protective cap layer.

11.1.3. PLD multilayers

PLD multilayers already represent an optimised pinning system, which is evident from the low α -values (cf. section 9.1.1) achieved independently of the dopant in this material (KT046 and KT062 contain Ir and Hf, respectively, KT60 is a reference sample). The introduction of additional pinning centres by the irradiation does not improve the pinning characteristics in the entire field, also at the lowest temperature of 4.2 K, where the quite moderate T_c -decrease of about 0.4 K can safely be disregarded. One might speculate that the additional defects frustrate the flux line lattice, i.e., the attraction of nearby defects promotes the depinning of vortices.

It is further interesting to note that the irreversibility is only slightly altered by the irradiation and shifted towards smaller fields. While the overall shape of the curve was not affected, the irreversibility field still remained at high values of around $B_{irr} \approx 11$ T at 77 K. However, it is expected that close to the transition temperature the reduction of T_c takes effect and must be taken into account. It becomes evident that this is indeed the case, when plotting the data on a reduced

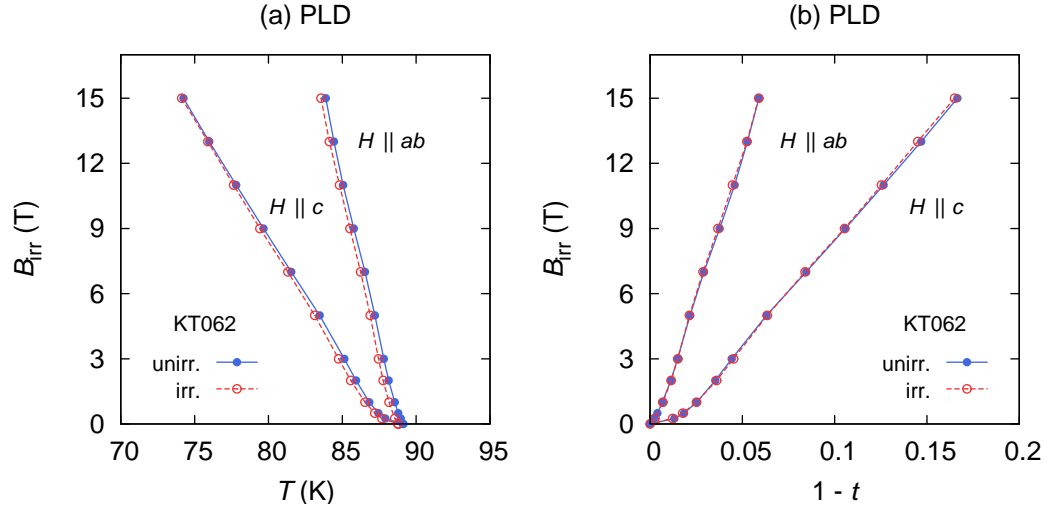


Figure 11.4. Irreversibility line of PLD multilayers before and after neutron irradiation. (a) Neutron irradiation decreases the irreversibility field H_{irr} somewhat, but the shapes of the irreversibility line remains the same. (b) On a reduced temperature scale ($t = T/T_c$), there is almost no difference between the irradiated and the unirradiated state because the change of H_{irr} results mainly from the reduction of T_c .

temperature scale $t = T/T_c$. The irradiated state is now closely matched by the unirradiated state, indicating that the reduction in T_c is mainly responsible for the slight shift of irreversibility line (see Fig. 11.4).

11.2. Poly-crystalline substrates

The second batch of irradiated samples consisted of films on both single- and poly-crystalline substrates and was mainly focused on the influence of neutron irradiation on the granularity in the conductors. In order to compare the results with previous measurements, the samples were exposed to a fluence of $2 \times 10^{21} \text{ m}^{-2}$, identical to the first irradiation.

11.2.1. Hysteresis loops

Two MOD coated conductors grown on metallic tapes (C22111, C13121) and a reference sample grown on single-crystalline YSZ (C020306C) provided by Nexans as well as two HLPE coated conductors grown on surface oxidised NiO (HR22 and HR55) were irradiated.

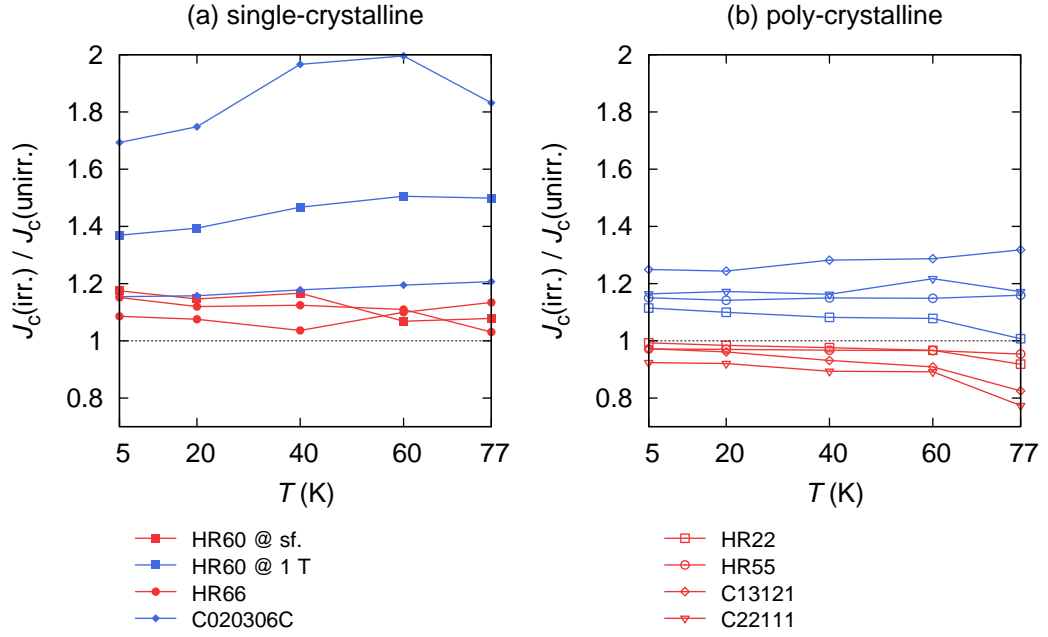


Figure 11.5. Relative enhancement in J_c after neutron irradiation. (a) All samples on single-crystalline substrates with counterparts on metallic tapes show enhanced pinning at self-field and at 1 T. (b) Samples deposited on poly-crystalline metal tapes show a decrease in J_c at self-field, while the critical current is enhanced at 1 T.

It turned out that the single-crystalline MOD film behaved similarly to the HLPE samples on STO discussed above: a substantial (up to twofold) increase of J_c was observed (see Fig. 11.5) in the entire temperature and field range of the VSM magnetisation measurements. This is a further indication that the surfaces of the MOD samples SS1646, SS1646 deteriorated, when they stuck together in the course of the irradiation.

If we now disregard these samples and compare only films with counterparts on poly-crystalline substrates, i.e., HLPE and Nexans MOD samples, we find that the J_c improvement relative to the unirradiated state is only moderate in all the samples on poly-crystalline tapes (see Fig. 11.5). Also with the additional pinning centres J_c is significantly less compared to the unirradiated single-crystalline films. The low J_c on tapes is thus not due to a lack of pinning, as already indicated when discussing the self-field effects of intra- and inter-grain currents (cf. section 9.1). A possible explanation is severe granularity in the film and the suppression of the order parameter at the grain-boundary positions, which keeps the transport current low, even if the material provides enough pinning centres for much higher currents.

Unlike in single-crystalline samples, the self-field J_c decreases in all the samples on metallic substrates, independently of the deposition technique (MOD, HLPE), in the entire temperature range. At higher magnetic fields, however, a weakly temperature dependent cross-over in $J_c(B)$ between the irradiated and the unirradiated state was found (cf. Fig. 11.6). This behaviour, i.e., irradiated samples show enhanced J_c only above a certain cross-over field, is consistently observed in all the granular samples and clearly distinguishes them from the single-crystalline films.

This peculiarity of the $J_c(B)$ curve can be interpreted in terms of a transition from grain boundary to grain controlled current transport. If the neutron irradiated samples on single-crystals are considered as a model system for the grains in the granular samples, the enhancement in J_c indicates increased pinning in the individual grains. On the other hand, a reduction of J_c at self-field can be attributed to the damaging influence of disorder on the grain boundaries. Therefore, the cross-over sketches the field domain, where the current carrying capability is limited by grain boundaries or by pinning in the grains: At low fields the grain boundaries limit the current transport and their deterioration reduces J_c . This effect is disabled at high fields, where the grains govern J_c and the introduction of additional pinning centres in the grains is responsible for the improvement of the in-field J_c .

It should be noted, that despite the lower quality of the samples, the results obtained here are similar to those obtained in commercially available conductors [30] regarding to the magnitude and temperature dependence of the cross-over field, and show, that the high field domain, important for applications, is controlled by the grains rather than by the grain-boundaries.

11.2.2. Remanent magnetisation

Another elucidating way to probe the grain-boundary network is measuring the remanent magnetic moment m_{rem} as a function of the maximum applied field H_{max} for successively larger fields [65]. Initially the vortices penetrate the sample via the weakly pinning grain-boundaries and inter-grain currents define m_{rem} . At a certain maximum applied field, the critical currents flow across the entire grain-boundary network and the magnetic moment levels off until vortices are forced to penetrate the grains by further increasing the applied field. This gives rise to a shoulder in $m_{\text{rem}}(H_{\text{max}})$ which separates the inter- and intra-grain current domains. Any

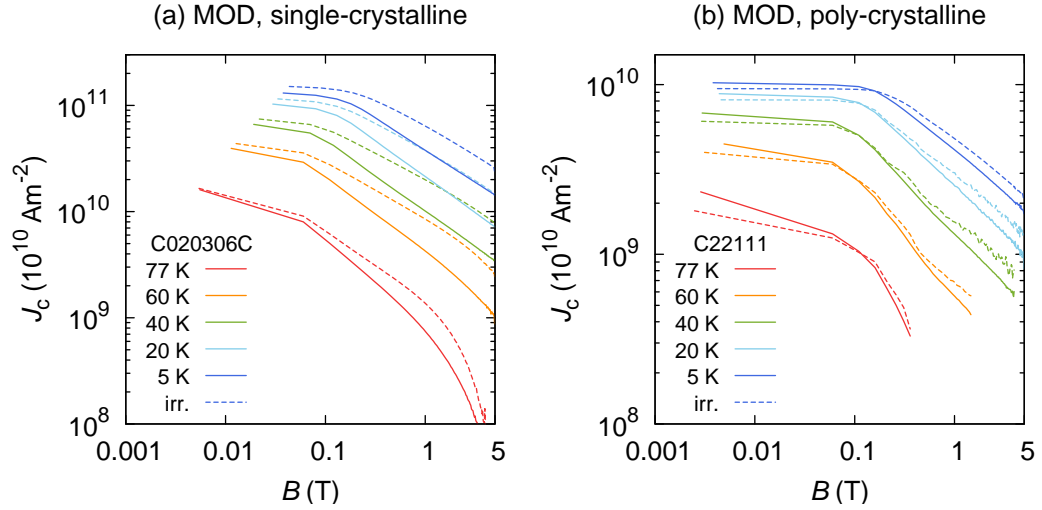


Figure 11.6. Cross-over in poly-crystalline samples. The cross-over field indicates the transition from the low field grain-boundary- to the high field grain-controlled current transport in granular samples.

additional contribution to m_{rem} stems from intra-grain critical currents and the $m_{\text{rem}}(H_{\text{max}})$ curve levels off a second time when the grains are saturated.

Although this procedure proved to be successful in $(\text{BiPb})_2\text{Sr}_2\text{Ca}_2\text{Cu}_3\text{O}_x$ conductors [63], it is not applicable to YBCO tapes, because the grains contribute insignificantly to the total magnetic moment (see section 5.1.2). However, there is evidence that the grain critical current J_c^G affects the magnetic moment indirectly [45], because the grain-boundary critical current density $J_c^{\text{GB}}(B)$ depends on field. At zero applied field the sample's self-field is generated either by J_c^{GB} flowing across the whole sample or by J_c^G circulating in the individual grains. When the grain-boundary critical currents have saturated, the magnetic field at the grain-boundaries is henceforth controlled by the saturating grains, which increase the magnetic induction at the edges of the grains. The remanent magnetic moment of the sample will thus peak and decrease when the grains saturate.

This view is supported by experiment as depicted in Fig. 11.7 showing measurements of $m_{\text{rem}}(H_{\text{max}})$ before and after irradiation. The film deposited on a single-crystalline substrate (C020306C) closely follows the theoretical curve (2.4) for a single domain subsequently penetrated by flux. After the irradiation m_{rem} is somewhat increased due to the enhanced critical current density, which results in a higher penetration field and a shift of the curve to higher magnetic fields.

The situation is quite different in the strongly granular sample (C22111). First, the penetration field is much lower, reflecting the small J_c^{GB} of about $2 \times 10^{10} \text{ Am}^{-2}$,

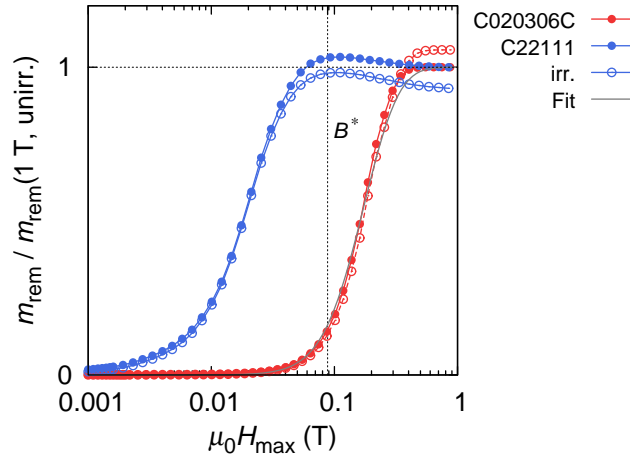


Figure 11.7. Remanent magnetisation in single- and poly-crystalline samples. While single-crystalline films closely follow the theoretical curve, m_{rem} decreases in poly-crystalline samples above fields comparable to B^* of the single-crystalline sample due to the field applied by the grains to the grain-boundaries.

and the sample already saturates at much lower fields. But at an applied field comparable to H^* of the single-crystalline sample the magnetic remanent moment starts to decrease for the reasons described above. This demonstrates that two different critical current densities flowing on two distinct length scales are present in this sample. After the irradiation the pattern is similar, but m_{rem} decreases to a lower value in agreement with the VSM hysteresis loops.

Hence, an alternative mechanism is suggested for the origin of the crossover in $J_c(B)$: due to the enhanced J_c^G after irradiation, a higher induction in the grains is effective at the grain-boundaries, which in turn decreases the field dependent J_c^{GB} and thus the magnetic moment of the sample. This mechanism is only based on the assumption of improved pinning in the grains, a result which is indirectly confirmed by measurements on single-crystalline samples, and does not rely on grain-boundary deterioration. The basic result, i.e., that the cross-over field indicates the transition from grain-boundary- to grain-controlled current transport remains unchanged.

Chapter 12.

Summary

The critical current density J_c in samples grown by pulsed laser deposition (PLD), hybrid liquid phase epitaxy (HLPE), and metal-organic deposition (MOD) has been investigated as a function of field and temperature. The latter two growth processes are of particular interest from a technological point of view, because HLPE is faster and MOD less expensive than conventional PLD and will thus appeal to industry—once growth of high-performing conductors on metallic substrates is successfully established.

Among the samples grown on single-crystalline substrates the highest critical current density J_c is achieved by PLD; the highest critical current per unit width, the most relevant factor for applications, is carried by HLPE samples, which can be grown to high thicknesses without deterioration of the superconductor. The field dependence of the critical current density $J_c(B)$ improves in HLPE samples containing BaZrO_3 , suggesting this secondary phase as a possible candidate to enhance J_c in high magnetic fields. However, neutron irradiation, which allows to modify the defect structure of the material in a controlled way, demonstrates that an even better performance is possible, if the defect state is optimised in HLPE or MOD films. The already high J_c and the weak field dependence in samples grown by PLD do not improve after irradiation, which indicates that these samples already contain a highly effective defect matrix.

On poly-crystalline substrates HLPE and MOD films carry a significantly lower J_c and further optimisation is required until the conductors are ready for applications. After irradiation J_c does not improve, which indicates that the low performance derives from granularity rather than from a lack of pinning centres. This view is also supported taking self-field effects in films with grain-boundaries into account. In granular samples a cross-over of $J_c(B)$ between the irradiated and the unirradiated state indicates a transition from grain-boundary to grain

controlled current transport and shows that pinning in the grains governs the current transport in the field range important for applications.

Scanning Hall probe measurements are of practical and fundamental interest. The magnetoscan allows a swift characterisation of long tapes and provides valuable information on the homogeneity of the supercurrent flow; the results agree with transport measurements of the critical current. The calculation of the local J_c from Hall scans of the self-field allows to quantify J_c as a function of the position in the film. It was found that J_c and B at a certain position are closely correlated in bulk superconductors as well as in thin films which is indicative of a field dependence $J_c(B)$ at fields below the self-field of a sample. This is a unique feature of this method, because numerical simulation of transport and magnetisation measurements show that this field domain is not accessible to measurements of the average J_c of a film. Simulations are further employed to confirm an analytical expression derived to quantify the effect of $J_c(B)$ on the thickness dependence of J_c .

Of pure theoretical interest is the mechanism responsible for the simultaneous occurrence of shoulders and a sharp a,b -peak in the J_c anisotropy curve close to $H \parallel ab$, which was discussed in terms of a transition between different pinning regimes. Supportive evidence comes from the dependence of the n -value on J_c : for samples without this peculiar feature, the n -value/ J_c relation behaves in the expected way and follows a smooth curve, while it changes abruptly at the a,b -peak position in samples with shoulders. Arguments have been provided, which are in favor of a transition into an intrinsic pinning regime, when the applied magnetic field is aligned close to the a,b -planes.

Bibliography

- [1] B. Dam, J. M. Huijbregtse, F. C. Klaassen, R. C. F. van der Geest, G. Doornbos, J. H. Rector, A. M. Testa, F. S., J. C. Martinez, B. Stäuble-Pümpin, and R. Griessen, “Origin of high critical currents in $\text{YBa}_2\text{Cu}_3\text{O}_{7-\delta}$ superconducting thin films,” vol. 399, pp. 439–442, 1999.
- [2] E. Zeldov, “Magnetization transport currents in thin superconducting films,” *Phys. Rev. B*, vol. 49, pp. 9802–9822, 1994.
- [3] R. Liang, P. Dosanjh, D. A. Bonn, and W. N. Hardy, “Lower critical fields in a ellipsoid-shaped $\text{YBa}_2\text{Cu}_3\text{O}_{6.95}$ single crystal,” *Phys. Rev. B*, vol. 50, pp. 4212–4216, 1994.
- [4] E. H. Brandt and M. Indenbom, “Type-II-superconductor strip with current in a perpendicular magnetic field,” *Phys. Rev. B*, vol. 48, pp. 12 893–12 906, 1993.
- [5] C. P. Poole, H. A. Farach, and R. J. Creswick, *Superconductivity*. Dan Diego, California: Academic Press, Inc., 1995, ch. Magnetic Properties, p. 326.
- [6] X. Obradors, T. Puig, A. Pomar, F. Sandiumenge, N. Mestres, M. Coll, A. Cavallaro, N. Romà, J. Gázquez, J. C. Gonzáles, O. Castaño, J. Gutierrez, A. Palau, K. Zalamova, S. Morlens, A. Hassini, M. Gilbert, S. Ricart, J. M. Moretó, S. Piñol, D. Isfort, and J. Bock, “Progress towards all-chemical superconducting $\text{YBa}_2\text{Cu}_3\text{O}_7$ -coated conductors,” *Supercond. Sci. Technol.*, vol. 19, pp. 13–26, 2006.
- [7] D. Dijkamp, T. Venkatesan, X. D. Wu, S. A. Shasheen, N. Jisrawi, Y. H. Min-Lee, W. L. McLean, and M. Croft, “Preparation of Y-Ba-Cu oxide superconductor thin films using pulsed laser evaporation from high T_c bulk material,” *Appl. Phys. Lett.*, vol. 51, pp. 619–621, 1987.
- [8] H. C. Freyhardt, R. Wördenweber, B. Utz, A. Usoskin, and Y. Yamada, “Physical vapour deposition techniques,” in *Handbook of Superconducting Materials*, D. A. Cardwell and D. S. Ginley, Eds. Institute of Physics Publishing, 2003, pp. 741–763.
- [9] J. Hänisch, C. Cai, R. Hühne, L. Schultz, and B. Holzapfel, “Formation of nanosized BaIrO_3 precipitates and their contribution to flux pinning in Ir-doped $\text{YBa}_2\text{Cu}_3\text{O}_{7-\delta}$ quasi-multilayers,” *Appl. Phys. Lett.*, vol. 86, p. 122508, 2005.

- [10] J. Hänisch, C. Cai, V. Stehr, R. Hühne, L. J., K. Nenkov, G. Fuchs, L. Schultz, and B. Holzapfel, “Formation and pinning properties of growth-controlled nanoscale precipitates in $\text{YBa}_2\text{Cu}_3\text{O}_{7-\delta}$ /transition metal quasi-multilayers,” *Supercond. Sci. Technol.*, vol. 19, pp. 534–540, 2006.
- [11] A. Kursumovic, Y. S. Cheng, B. A. Glowacki, J. Madsen, and J. E. Evetts, “Study of the rate-limiting process in liquid-phase epitaxy of thick YBaCuO films,” *J. Crystal Growth*, vol. 218, pp. 45–56, 2000.
- [12] A. Kursumovic, R. I. Tomov, R. Hühne, J. L. MacManus-Driscoll, B. A. Glowacki, and J. E. Evetts, “Hybrid liquid phase epitaxy processes for $\text{YBa}_2\text{Cu}_3\text{O}_7$ film growth,” *Supercond. Sci. Technol.*, vol. 17, pp. 1215–1223, 2004.
- [13] A. Kursumovic, J. Evetts, J. L. MacManus-Driscoll, B. Maiorov, L. Civale, H. Wang, Q. X. Jia, and S. R. Foltyn, “High critical current densities in $\text{YBa}_2\text{Cu}_3\text{O}_{7-x}$ films grown at high rates by hybrid liquid phase epitaxy,” *Appl. Phys. Lett.*, vol. 87, p. 252507, 2005.
- [14] A. Kursumovic, R. Tomov, R. Hühne, B. A. Glowacki, J. E. Evetts, A. Tuisi, E. Villa, and B. Holzapfel, “High temperature growth kinetics and texture of surface-oxidised nio for coated conductor application,” *Physica C*, vol. 385, pp. 337–345, 2003.
- [15] X. Obradors, T. Puig, A. Pomar, F. Sandiumenge, S. Pinñol, N. Mestres, O. Castaño, M. Coll, A. Cavallaro, A. Palau, J. Gázquez, J. C. Gonzáles, J. Gutiérrez, N. Romà, S. Ricasrt, J. M. Moretó, M. D. Rossell, and G. van Tendeloo, “Chemical solution deposition: a path towards low cost coated conductors,” *Supercond. Sci. Technol.*, vol. 17, pp. 1055–1064, 2004.
- [16] S. Foner, “Vibrating sample magnetometer,” *Rev. Sci. Instrum.*, vol. 27, p. 548, 1956.
- [17] —, “The vibrating sample magnetometer: Experiences of a volunteer,” *J. Appl. Phys.*, vol. 79, pp. 4740–4745, 1996.
- [18] —, “Versatile and sensitive vibrating-sample magnetometer,” *Rev. Sci. Instrum.*, vol. 30, pp. 548–557, 1959.
- [19] J. Mallison, “Magnetometer coils and reciprocity,” *J. Appl. Phys.*, vol. 37, pp. 2514–2515, 1966.
- [20] B. J. Roth, N. G. Sepulveda, and J. P. Wikswo, “Using a magnetometer to image a two-dimensional current distribution,” *J. Appl. Phys.*, vol. 65, pp. 361–372, 1998.
- [21] F. Hengstberger, “Entwicklung einer Magneto-Scan-Anlage,” Master’s thesis, TU Wien, 2005.

- [22] H. W. Weber, H. Böck, and E. Unfried, “Neutron dosimetry and damage calculations for the TRIGA MARK-II reactor in Vienna,” *J. Nucl. Mater.*, vol. 137, pp. 236–240, 1986.
- [23] M. C. Frischherz, M. A. Kirk, J. Farmer, L. R. Greenwood, and H. W. Weber, “Defect cascades produced by neutron irradiation in $\text{YBa}_2\text{Cu}_3\text{O}_{7-\delta}$,” *Physica C*, vol. 232, pp. 309–327, 1994.
- [24] C. P. Bean, “Magnetization of hard superconductors,” *Phys. Rev. Lett.*, vol. 66, pp. 250–253, 1962.
- [25] H. P. Wiesinger, F. M. Sauerzopf, and H. W. Weber, “On the calculation of J_c from magnetization measurements on superconductors,” *Physica C*, vol. 203, pp. 121–128, 1992.
- [26] M. Zehetmayer, “Anisotropic magnetic properties of superconducting MgB_2 and $\text{HgBa}_2\text{CuO}_{4+\delta}$ single crystals,” Ph.D. thesis, TU Wien, 2003.
- [27] H. Hilgenkamp and J. Mannhart, “Grain boundaries in high- T_c superconductors,” *Rev. Mod. Phys.*, vol. 74, pp. 485–549, 2002.
- [28] *Superconductivity - Part 1: Critical current measurements - DC critical current of Nb-Ti composite superconductors*, International Electrotechnical Commission (IEC), 2006.
- [29] *Scilab manual*, The Scilab consortium, 2009. [Online]. Available: <http://www.scilab.org/product/man/datafit.html>
- [30] R. Fuger, “Analysis of high temperature superconductors for applications in fusion magnets,” Ph.D. thesis, TU Wien, 2008.
- [31] M. Zehetmayer, M. Eisterer, and H. W. Weber, “Simulation of the current dynamics in a superconductor induced by a small permanent magnet: application to the magnetoscan technique,” *Supercond. Sci. Technol.*, vol. 19, pp. 429–437, 2006.
- [32] M. Zehetmayer, R. Fuger, M. Eisterer, F. Hengstberger, and H. W. Weber, “Assessment of the local supercurrent densities in long superconducting coated conductors,” *Appl. Phys. Lett.*, vol. 90, p. 032506, 2007.
- [33] F. Hengstberger, R. Fuger, M. Eisterer, H. W. Weber, and D. Isfort, “Homogeneity of supercurrent flow in coated conductors,” *Physica C*, vol. 460–462, pp. 1397–1398, 2007.
- [34] J. H. Claassen, M. E. Reeves, and R. J. Soulen, “A contactless method for measurement of the critical current density and critical temperature of superconducting films,” *Rev. Sci. Instrum.*, vol. 62, pp. 996–1004, 1991.

- [35] R. J. Wijngaarden, H. J. W. Spoelder, R. Surdeanu, and G. R., “Determination of two-dimensional current patterns in flat superconductors from magneto-optical measurements: An efficient inversion scheme,” *Phys. Rev. B*, vol. 54, pp. 6742–6746, 1996.
- [36] C. Jooss, R. Warthmann, A. Forkl, and H. Kronmüller, “High-resolution magneto-optical imaging of critical currents in $\text{YBa}_2\text{Cu}_3\text{O}_{7-\delta}$ thin films,” *Physica C*, vol. 299, pp. 215–230, 1998.
- [37] *NICONET manual*, Working Group of Software (WGS), 2009. [Online]. Available: <http://www.icm.tu-bs.de/NICONET>
- [38] V. Sima, private communication.
- [39] R. W. Hamming, *Digital Filters*, 3rd ed. Mineola, New York: Dover Publications, Inc., 1989, ch. Design of Nonrecursive Filters.
- [40] M. Eisterer, “The significance of solutions of the inverse biot-savart problem in thick superconductors,” *Supercond. Sci. Technol.*, vol. 18, pp. 5–62, 2005.
- [41] F. Hengstberger, M. Eisterer, M. Zehetmayer, and H. W. Weber, “Assessing the spatial and field dependence of the critical current density in ybco bulk superconductors by scanning hall probes,” *Supercond. Sci. Technol.*, vol. 22, p. 025011, 2009.
- [42] E. H. Brandt, “Square and rectangular thin superconductors in a transverse magnetic field,” *Phys. Rev. Lett.*, vol. 74, pp. 3025–3028, 1995.
- [43] M. Däumling and W. Goldacker, “Specimen geometry effects on the irreversible magnetization in the low field regime for specimens of bulk Nb_3Sn ,” *Z. Phys. B.*, vol. 102, pp. 331–336, 1997.
- [44] A. Sanchez and C. Navau, “Critical-current density from magnetization loops of finite high- T_c superconductors,” *Supercond. Sci. Technol.*, vol. 14, pp. 444–447, 2001.
- [45] A. Palau, T. Puig, X. Obradors, and C. Joos, “Simultaneous determination of grain and grain-boundary critical currents in $\text{YBa}_2\text{Cu}_3\text{O}_7$ -coated conductors by magnetic measurements,” *Phys. Rev. B*, vol. 75, p. 054517, 2007.
- [46] B. Zeimetz, R. P. Baranowski, and J. E. Evetts, “Finite element calculations of local current distribution in anisotropic superconductors in external and self magnetic field,” *IEEE Trans. Appl. Supercond.*, vol. 11, pp. 3354–3358, 2001.
- [47] F. Gömöry, J. Šouc, M. Vojenčiak, and B. Klinčok, “Phenomenological description of flux pinning in non-uniform high-temperature superconductors in fields lower than the self-field,” *Supercond. Sci. Technol.*, vol. 20, pp. 271–277, 2007.

- [48] L. Rostila, J. Lehtonen, and R. Mikkonen, “Self-field reduces critical current density in thick YBCO layers,” *Physica C*, vol. 451, pp. 66–70, 2007.
- [49] L. Rostila, J. Lehtonen, R. Mikkonen, J. Šouc, E. Seiler, T. Melíšek, and M. Vojenčiak, “How to determine critical current density in YBCO tapes from voltage-current measurements at low magnetic fields,” *Supercond. Sci. Technol.*, vol. 20, pp. 1097–1100, 2007.
- [50] Y. B. Kim, C. F. Hempstead, and A. R. Strnad, “Persistent currents in hard superconductors,” *Phys. Rev. Lett.*, vol. 9, pp. 306–309, 1962.
- [51] A. Kursumovic, B. Maiorov, J. H. Durrell, H. Wang, H. Zhou, L. Stan, S. Harrington, S. Wimbush, T. G. Holesinger, and J. L. MacManus-Driscoll, “High I_c , $\text{YBa}_2\text{Cu}_3\text{O}_{7-x}$ films grown at very high rates by liquid assisted growth incorporating lightly Au-doped SrTiO_3 buffers,” *Supercond. Sci. Technol.*, vol. 22, p. 015009, 2009.
- [52] J. Gutiérrez, A. Llordés, J. Gázquez, M. Gibert, N. Romà, S. Ricart, A. Pomar, F. Sandiumenge, N. Mestres, T. Puig, and X. Obradors, “Strong isotropic flux pinning in solution derived $\text{YBa}_2\text{Cu}_3\text{O}_{7-x}$ nanocomposite superconductor films,” *Nature Mater.*, vol. 6, pp. 367–373, 2007.
- [53] C. J. Beek, M. Konczykowski, A. Abal’oshev, I. Abal’osheva, P. Gierlowski, S. J. Lewandowski, M. V. Indenbom, and S. Barbanera, “Strong pinning in high-temperature superconducting films,” *Phys. Rev. B*, vol. 66, p. 024523, 2002.
- [54] J. L. MacManus-Driscoll, S. R. Foltyn, Q. X. Jia, H. Wang, A. Serquis, L. Civale, B. Maiorov, M. E. Hawley, M. P. Maley, and D. E. Peterson, “Strongly enhanced current densities in superconducting coated conductors of $\text{YBa}_2\text{Cu}_3\text{O}_{7-x}+\text{BaZrO}_3$,” *Nature Mater.*, vol. 3, pp. 439–443, 2004.
- [55] A. Kursumovic, private communication.
- [56] F. Hengstberger, M. Eisterer, H. W. Weber, A. Kursumovic, and J. L. MacManus-Driscoll, “Critical current anisotropy in nanostructured HLPE coated conductors,” *J. Phys: Conf. Ser.*, vol. 97, p. 012012, 2008.
- [57] K. Matsumoto, T. Horide, A. Ichinose, S. Horii, Y. Yoshida, and M. Mukaida, “Critical current control in $\text{YBa}_2\text{Cu}_3\text{O}_{7-\delta}$ films using artificial pinning centers,” *Jpn. J. Appl. Phys.*, vol. 44, pp. 246–248, 2005.
- [58] B. Maiorov, A. Kursumovic, L. Stan, H. Zhou, H. Wang, L. Civale, R. Feenstra, and J. L. MacManus-Driscoll, “Vortex pinning landscape in $\text{YBa}_2\text{Cu}_3\text{O}_7$ films grown by hybrid liquid phase epitaxy,” *Supercond. Sci. Technol.*, vol. 20, pp. 223–229, 2007.
- [59] L. Civale, B. Maiorov, J. L. MacManus-Driscoll, H. Wang, T. G. Holesinger, S. R. Foltyn, A. Serquis, and P. N. Arendt, “Identification of intrinsic

ab-plane pinning in $\text{YBa}_2\text{Cu}_3\text{O}_7$ thin films and coated conductors,”
IEEE Trans. Appl. Supercond., vol. 15, pp. 2808–2811, 2005.

- [60] Y. Yeshurun and A. P. Malozemoff, “Giant flux creep and irreversibility in an Y-Ba-Cu-O crystal: an alternative to the superconducting-glass model,”
Phys. Rev. Lett., vol. 60, pp. 2202–2205, 1988.
- [61] F. M. Sauerzopf, “Anisotropic flux pinning in $\text{YBa}_2\text{Cu}_3\text{O}_{7-\delta}$ single crystals: The influence of defect size and density as determined from neutron irradiation,” *Phys. Rev. B*, vol. 57, pp. 10 959–10 971, 1998.
- [62] H. W. Weber, “Irradiation,” in *Handbook of Superconducting Materials*, D. A. Cardwell and D. S. Ginley, Eds. Institute of Physics Publishing, 2003, pp. 407–418.
- [63] S. Tönies, A. Vostner, and H. W. Weber, “Determination of inter- and intragranular currents in high temperature superconducting tapes and coated conductors,” *J. Appl. Phys.*, vol. 92, pp. 2628–2633, 2002.
- [64] F. Hengstberger, M. Eisterer, H. W. Weber, A. Kursumovic, and J. L. MacManus-Driscoll, “Irreversible magnetic properties of neutron irradiated HLPE coated conductors,” *Physica C*, vol. 17, pp. 3549–3552, 2007.
- [65] K. H. Müller, C. Andrikidis, H. K. Liu, and D. S. X., “Intergranular and intragranular critical currents in silver-sheated Pb-Bi-Sr-Ca-Cu-O tapes,”
Phys. Rev. B, vol. 50, pp. 10 218–10 224, 1994.

List of Figures

1.1. Thermal activation of a vortex and resistive transition of a superconductor	4
2.1. Application of the Bean model to thin films—current distribution and self-field	8
3.1. Optical micrograph of a bridged HLPE sample	13
3.2. Pattern used in transport measurements on HLPE samples	15
4.1. Coil configuration of a SQUID	18
4.2. Coil configuration of the VSM	19
4.3. Sensitivity of the VSM in the x,y -plane	21
4.4. Definition of the angles in the 6 T-system	24
4.5. Magnetic field in z -direction of a current	26
4.6. Čerenkov radiation in the pool of the TRIGA MARK-II research reactor	28
4.7. SEM images of HLPE samples made in a FIB system	29
5.1. Bean model for an infinitely long bar	32
5.2. Evaluation of magnetisation loops taking the self-field into account	33
5.3. Role of voltage criterion in defining I_c	36
5.4. Identification of the n -value	37
5.5. Determination of the irreversibility line	39
5.6. Comparison of different evaluation methods for T_c and ΔT_c . . .	40
6.1. Simulation of the current distribution induced by the magnetoscan	44
6.2. Field profile of a coated conductor carrying an odd current distribution	45
6.3. Comparison between magnetoscan and transport measurements .	47
6.4. Comparison between magnetoscan and cryoscan	48
7.1. Coordinate system inversion and symmetry of the matrix	51
7.2. Illustration of the inversion procedure	54
7.3. Condition number and illustration of the condition problem . . .	56
7.4. Flux profile and current density of a bulk heated in the centre . .	59
7.5. Correlation between J_c and B in bulk superconductors	60
7.6. Comparison to magnetometry	61
7.7. Detection of defects and $J_c(B)$ correlation in thin films	63
7.8. Correlation between J_c and B in thin films	64
7.9. Coil used for magnetising thin films and partial reversal of flux in a sample	65

7.10. Comparison of the magnetic moment assessed by SQUID and scan measurements	66
8.1. Low field plateau and power-law field dependence of $J_c(H)$	69
8.2. Flow chart sketching the iterative procedure employed to calculate the current distribution for an arbitrary material law $J_c(\vec{B})$	70
8.3. Magnetic field distribution in a thin disk at low applied fields . . .	72
8.4. Simulated $J_c(H)$ using a power-law $J_c(B)$ and role of the sheet current K_c in a thin disk	73
8.5. Magnetic field distribution in a thin conductor at low applied fields	75
8.6. Simulations at low applied fields	76
8.7. Fitting the material law to the measurement data	77
8.8. Approximations used to derive $J_c(c)$ from $J_c(B)$	78
8.9. Confirmation of the derived equation by simulations	80
9.1. Field dependence of the critical current density	84
9.2. Hall scan of HLPE coated conductors	85
9.3. Temperature dependence of the α -value	87
9.4. Critical current density in doped conductors	88
9.5. X-ray diffraction on HLPE films	89
10.1. Anisotropy of J_c in doped HLPE films	92
10.2. Field dependence of J_c in HLPE films	93
10.3. Correlation between the n -value and J_c in FH752	95
10.4. Correlation between the n -value and J_c at maximum Lorentz force	96
10.5. Correlation between the n -value and J_c at variable Lorentz force .	96
10.6. Irreversibility line in HLPE films and coated conductors	98
10.7. Irreversibility line in PLD films and best power-law fits	99
11.1. Irradiation of HLPE films.	103
11.2. Irradiation of MOD films	104
11.3. Irradiation of PLD multilayers	105
11.4. Irreversibility line of PLD multilayers before and after neutron irradiation	106
11.5. Relative enhancement in J_c after neutron irradiation	107
11.6. Cross-over in poly-crystalline samples	109
11.7. Remanent magnetisation in single- and poly-crystalline samples .	110

List of Tables

9.1. Key data of the samples used for magnetisation measurements . .	90
10.1. Key data of the samples used for transport measurements	100

Curriculum vitae

Name Florian Anton Hengstberger

Address Wachaustraße 41
3121 Karlstetten

Place of Birth Krems an der Donau

Date of Birth April 7, 1981

Education

2009 PhD thesis

2005–2009 PhD research at the
Vienna University of Technology,
Project Assistant

2005 Diploma thesis on
“Development of a magnetoscan device”

2000–2005 Studies of physics at the
Vienna University of Technology,
Tutorial Assistant

1995–1999 Secondary academic school (natural science class)

Publications

F. Hengstberger, M. Eisterer, M. Zehetmayer, and H. W. Weber,
“Assessing the spatial and field dependence of the critical current density in
YBCO bulk superconductors by scanning Hall probes,”
Supercond. Sci. Technol., vol. 22, p. 025011, 2009.

R. Fuger, M. Eisterer, F. Hengstberger, and H. W. Weber,
“Influence of neutron irradiation on high temperature superconducting
coated conductors,”
Physica C, vol. 468, pp. 1647–1651, 2008.

- F. Hengstberger, M. Eisterer, H. W. Weber, A. Kursumovic, and J. L. MacManus-Driscoll,
 “Critical current anisotropy in nanostructured HLPE coated conductors,”
J. Phys: Conf. Ser., vol. 97, p. 012012, 2008.
- F. Hengstberger, R. Fuger, M. Eisterer, H. W. Weber, and D. Isfort,
 “Homogeneity of supercurrent flow in coated conductors,”
Physica C, vol. 460–462, pp. 1397–1398, 2007.
- M. Zehetmayer, R. Fuger, F. Hengstberger, M. Kitzmantel, M. Eisterer, and H. W. Weber,
 “Modified magnetoscan technique for assessing inhomogeneities in the current flow of coated conductors - Theory and experiment,”
Physica C, vol. 460–462, pp. 158–161, 2007.
- F. Hengstberger, M. Eisterer, H. W. Weber, A. Kursumovic, and J. L. MacManus-Driscoll,
 “Irreversible magnetic properties of neutron irradiated HLPE coated conductors,”
IEEE Trans. Appl. Supercond., vol. 17, pp. 3549–3552, 2007.
- R. Fuger, F. Hengstberger, M. Eisterer, and H. W. Weber,
 “Scan techniques for coated conductors,”
IEEE Trans. Appl. Supercond., vol. 17, pp. 3753–3756, 2007.
- M. Zehetmayer, R. Fuger, M. Eisterer, F. Hengstberger, and H. W. Weber,
 “Assessment of the local supercurrent densities in long superconducting coated conductors,”
Appl. Phys. Lett., vol. 90, p. 032506, 2007.
- T. D. Withnell, N. H. Babu, K. Iida, Y. Shi, D. A. Cardwell, S. Haindl, F. Hengstberger, and H. W. Weber,
 “The effect of seed orientation and separation on the field trapping propoerties of multi-seeded, melt processed Y-Ba-Cu-O,”
Physica C, vol. 445–448, pp. 382–386, 2006.
- F. Hengstberger, S. Haindl, H. W. Weber, and X. Chaud,
 “Investigation of artificially patterned YBCO single domain bulks,”
J. Phys: Conf. Ser., vol. 43, pp. 513–517, 2006.
- S. Haindl, F. Hengstberger, H. W. Weber, S. Meslin, J. Noudem, and X. Chaud,
 ”Hall probe mapping of melt processed superconductors with artifical holes”,
Supercond. Sci. Technol., vol. 19, pp. 108–115, 2006.